Measurement of Forces in a Low Consistency Refiner

by

Brett Cameron Prairie
B.Sc. Queen's University, 2003

A Thesis Submitted in Partial Fulfillment of the
Requirements for the Degree of

MASTER OF APPLIED SCIENCE

in the Department of Mechanical Engineering

Supervisor: Dr. Peter M. Wild

ABSTRACT

A piezo-ceramic sensor was developed to measure normal and tangential shear forces applied to a bar at one location in the refining zone of a Sunds Defibrator Conflo® JC-00 refiner. Testing was completed at the Pulp and Paper Research Institute of Canada in Vancouver, BC using CTMP pulp with a stock consistency of 3.15%. Distributions have been determined for peak normal and shear forces, peak coefficient of friction, shear work, and shear lead. These distributions were analysed to assess possible correlations with specific edge load. Force magnitudes were found to increase with an increase in specific edge load. The peak coefficient of friction was calculated that ranged from 0.13 to 0.16. Both the normal and shear force magnitudes varied by as much as a factor of 3, due to rotor out-of-tram of only 0.06 mm. These distributions could provide greater insight to the mechanisms responsible for fibre development in papermaking and thus "In Process" control of various refiner conditions.

ACKNOWLEDGEMENTS

Thank you to Peter Wild for you for your patience. I cannot stress this enough. Ever since I arrived at the university you have been quite accommodating. It has been a pleasure working on this project with a supervisor that has such a breadth of knowledge in all things mechanical.

I would also like to thank Peter Byrnes for providing countless hours explaining to me just about everything about this project. What I find amazing is that for every question I have, you seem to have the answer. Just being in your company has helped me greatly improve as a researcher. I would also like to emphasize that it's been Trulli great to have someone else to talk to about Formula 1.

Dustin. From the trail tips on the coast to helping me develop my flick to countless days on the road, it's been a lot of fun and I'm always learning from you. Thank you for being a great friend during and after work. The only thing that seems odd about this friendship is the amount of pulp and paper, and force sensor talk that goes on between you and me in public.

I would also like to thank the Pulp and Paper Research Institute of Canada for their financial support to the project. Daniel Ouellet, Norm Roberts and Bill Francis, thank you immensely for guiding me through my experiments. Thank you to NSERC and Andritz Ltd. for their financial contributions to this research.

To my friends in Victoria, whether it is hiking, camping, skiing, or any other adventure that could have you stuck up island without a set of tent poles, it has always been fun.

To my family, you have been so supportive of me since forever. This degree is so much sweeter knowing that you've been there every step of the way. I love you very much.

TABLE OF CONTENTS

ABSTRACT ..... **II**

ACKNOWLEDGEMENTS ..... **III**

LIST OF FIGURES ..... **VIII**

LIST OF TABLES ..... **XIII**

LIST OF NOMENCLATURE ..... **XIV**

1 INTRODUCTION **1**

1.1 MECHANICAL PULP REFINING 1

1.1.1 Mechanical Refiners 1

1.2 PULP CONSISTENCY 3

1.3 LOW-CONSISTENCY MECHANICAL REFINING 4

1.4 FORCES MEASURED IN LC MECHANICAL REFINING 4

1.5 REFINER TRAM 8

1.6 REFINER FORCE SENSOR DEVELOPMENT 9

1.7 OBJECTIVE 11

1.8 METHODOLOGY AND THESIS OUTLINE 11

2 MODIFICATION/PREPARATION OF RFS4 FOR LC REFINING **13**

2.1 INTRODUCTION 13

2.2 PROBE GEOMETRY 13

2.3 FREQUENCY RESPONSE 15

2.4 REFINING ENVIRONMENT 17

2.5 CALIBRATION 18

2.6 SUMMARY 22

3 EXPERIMENTAL SETUP **23**

3.1 INTRODUCTION 23

3.2 SENSOR INSTALLATION INTO THE CONFLO® JC-00 STATOR 23

3.2.1 Sensor Sleeve 24

3.2.2 Machining of the Stator 25

3.3 DATA ACQUISITION 28
3.3.1 Charge Amp 30
3.3.2 High/Low-Speed DAQ Boards 31
3.3.3 Terminal Blocks 31
3.3.4 Sensor Wiring 32
3.3.5 Thermocouple 32
3.3.6 Virtual Instrument for Data Acquisition 32
3.4 SUMMARY 33

4 EXPERIMENTAL PROCEDURE 34

4.1 INTRODUCTION 34
4.2 PULP FURNISH 34
4.3 TARGET REFINING CONDITIONS 35
4.4 ACTUAL REFINING CONDITIONS 38
4.5 SUMMARY 41

5 DATA PROCESSING 42

5.1 INTRODUCTION 42
5.2 A BAR-PASSING EVENT 42
5.3 EVENT CLASSIFICATION 44
5.3.1 Primary Event Classification Criteria 45
5.3.2 Secondary Event Classification Criteria 47
5.3.3 Event Parameters 48
5.3.3.1 Normal and Shear Forces 48
5.3.3.2 Shear Work 49
5.3.3.3 Peak Coefficient of Friction 49
5.3.3.4 Shear Lead 49
5.4 SIGNAL CONDITIONING AND SELECTION OF EVENT CRITERIA 50
5.4.1 Upper and Lower Search Limits 50
5.4.2 Filtering 50
5.4.3 Proximity Limit and Event Length Ratio 55
5.4.4 Peak Fraction 57
5.5 ROTOR BAR IDENTIFICATION 60
5.6 RAW DATA EXTRACTION 61

5.7 MANUAL VERIFICATION 62
5.8 SUMMARY 63

6 RESULTS AND DISCUSSION I – FORCE PROFILES AND EVENT PARAMETER DISTRIBUTIONS 64

6.1 INTRODUCTION 64
6.2 FORCE PROFILES 64
6.3 PLATE SEGMENT IDENTIFICATION 68
6.4 OCCURRENCE RATIO 70
6.5 EVENT PARAMETER DISTRIBUTIONS 70
6.6 THE WEIBULL DISTRIBUTION 74
6.6.1 Effect of Varying the Weibull Parameters 75
6.7 SUMMARY 77

7 RESULTS AND DISCUSSION II – COMPARISONS BETWEEN EVENT PARAMETERS AND SPECIFIC EDGE LOAD 78

7.1 INTRODUCTION 78
7.2 VARIATIONS IN EVENT PARAMETERS AT THE REFINER LEVEL 78
7.3 COMPARING SENSOR MEASUREMENTS WITH THEORETICAL FORCE VALUES 82
7.4 SUMMARY 86

8 RESULTS AND DISCUSSION III – SEGMENT AND BAR VARIATIONS BETWEEN EVENT PARAMETERS AND SPECIFIC EDGE LOAD 87

8.1 INTRODUCTION 87
8.2 VARIATIONS IN EVENT PARAMETERS AT THE SEGMENT LEVEL 87
8.3 VARIATIONS IN EVENT PARAMETERS AT THE BAR LEVEL 91
8.4 THE EFFECT OF ROTOR TRAM ON FORCE LEVELS 94
8.4.1 Force Profiles 94
8.4.2 Rotor Alignment 96
8.4.3 Force Magnitudes 96
8.5 SUMMARY 98

9 CONCLUSIONS 99

10 RECOMMENDATIONS 101

REFERENCES **102**

APPENDIX A – REFINING CONDITIONS **104**

A.1. EXPERIMENT S9 104

A.2. EXPERIMENT S9B1 107

A.3. EXPERIMENT S9B2 110

A.4. EXPERIMENT S12 113

APPENDIX B – EVENT CLASSIFICATION AND BAR IDENTIFICATION LOGIC FLOW CHARTS **116**

B.1. EVENT CLASSIFICATION LOGIC 116

B.2. BAR IDENTIFICATION LOGIC 118

B.2.1. Bar Identification Main Routine 118

B.2.2. "Forward Pass" Subroutine 120

B.2.3. "Fill Bars Forward" Subroutine 121

B.2.4. "Fill Bars Reverse" Subroutine 122

B.2.5. "Delete Resonance" Subroutine 123

B.2.6. "Delete Duplicates" Subroutine 124

B.2.7. Count Segments 125

B.2.8. Count Revolutions 126

APPENDIX C –WEIBULL FORCE DISTRIBUTIONS AND MEDIAN VALUES **127**

C.1. REFINER LEVEL 127

C.2. SEGMENT LEVEL 128

C.2.1. Experiment S9 128

C.2.2. Experiment S9B1 130

C.2.3. Experiment S9B2 132

C.2.4. Experiment S12 134

C.3. BAR LEVEL 136

C.3.1. Bar #4 136

C.3.2. Bar #8 137

C.3.3. Bar #12 138

LIST OF FIGURES

Figure 1-1, Types of mechanical pulp refiners [1] 2
Figure 1-2, Conflo stator and rotor [4] 2
Figure 1-3, A conical refiner (Sunds Defibrator Conflo® refiner) [4] 3
Figure 1-4 - L-Shaped Beam Force Sensor Design. Normal Force "R", Shear Force "T" [5] 5
Figure 1-5, 2-Component Sensor. Normal Force "R", Shear Force "T" [5] 6
Figure 1-6, Measurements made by 2-Component Sensor. Horizontal axis represents overlap between refiner bars; vertical axis represents pressure measured by the sensor. [6] 6
Figure 1-7, Normal and shear forces measured in a single bar refiner [10] 7
Figure 1-8, RFS1 9
Figure 1-9, RFS2 10
Figure 1-10, RFS3 10
Figure 1-11, Front view of RFS4 installed in a plate segment (back view inset) 11
Figure 2-1, Sensor Location in the Conflo® JC-00 Stator 13
Figure 2-2, Conflo® JC-00 refiner bar geometry (dimensions in mm) 14
Figure 2-3, Conflo® JC-00 Stator refiner bars 14
Figure 2-4, Rotor bar orientation 15
Figure 2-5, Calibration of RFS4-LC (Normal and Shear Impacts respectively) 16
Figure 2-6, Frequency spectrum of RFS4-LC impulse response while retained in a testing plate. Piezo A is the piezoelectric element on the side of the leading edge of the sensor. 17
Figure 2-7, RFS4-LC Positive Directions of Impact 18
Figure 2-8, Time domain plots of force hammer response (left) and piezo voltage response (right) for RFS4-LC 19
Figure 2-9, RFS4-LC Normal Impact Calibration 20
Figure 2-10, RFS4-LC Leading Edge Shear Impact Calibration 20
Figure 3-1, RFS4-LC installed in the Conflo® JC-00 Stator (inside view) 23
Figure 3-2, Exploded view of RFS4-LC assembled in the sensor sleeve 24
Figure 3-3, RFS4-LC installed in the Conflo® JC-00 Stator (outside view) 24
Figure 3-4, Alignment fixture for locating the bars on the Conflo® JC-00 stator 25

Figure 3-5, Alignment fixture in place on the Conflo® JC-00 stator (alignment plate aligned with a stator bar) 26
Figure 3-6, Aligning the boring tool to the alignment plate 27
Figure 3-7, Machining of pocket into the Conflo® JC-00 stator 27
Figure 3-8, Workstation (showing data acquisition hardware) during refining trials (Pulp and Paper Research Institute of Canada – Vancouver, BC) 28
Figure 3-9, Instrumented Conflo® JC-00 refiner 29
Figure 3-10, Data acquisition schematic 29
Figure 3-11, Plot of the charge amplifier's transfer function 30
Figure 3-12, Data acquisition software front panel display 33
Figure 4-1, Schematic of the refiner showing the direction of pulp flow [20] 35
Figure 4-2, Target refining conditions for comparison with sensor data. Experiments at 900 rpm conducted at SELs of 0.33 J/m and 0.5 J/m, 1200 rpm conducted at an SEL of only 0.33 J/m. 37
Figure 4-3, Feed Rate during experiment S9 (applying a forward moving average filter of 100 points and a reverse moving average filter of 100 points) 38
Figure 4-4, Motor Load during experiment S9 (applying a forward moving average filter of 100 points and a reverse moving average filter of 100 points) 39
Figure 4-5, Specific edge load. Samples were extracted for analysis from grey regions. (Experiment S9) 40
Figure 4-6, Actual refining conditions for comparison with sensor data (Error bars indicate the range in refining conditions for each sample) 41
Figure 5-1, A bar-passing event [17] 42
Figure 5-2, Typical sensor data with bar-passing events indicated by dots (Experiment S9B1-5. Time: 9:23:20.000 - 9:23:20.010. [SEL=0.32 J/m]) 43
Figure 5-3, Sensor data (Experiment S9B1-5. Time: 9:23:20.0025 - 9:23:20.0035. [SEL=0.32 J/m]) 44
Figure 5-4, A potential bar-passing event 46
Figure 5-5, An example of Event Proximity 48
Figure 5-6, Effect of applying a notch filter to the data – unfiltered data shown above, filtered data below. (Experiment S9-8. Time: 9:08:13.010 - 9:08:13.017. [SEL=0.32 J/m]) 51

Figure 5-7, The distribution of event lengths on unfiltered data (Experiment S9-8. Time: 9:08:12 - 9:08:17. [SEL=0.32 J/m]) 52
Figure 5-8, The distribution of event lengths on unfiltered data – cropped (Experiment S9-8. Time: 9:08:12 - 9:08:17. [SEL=0.32 J/m]) 53
Figure 5-9, The distribution of event lengths on filtered data (Experiment S9-8. Time: 9:08:12 - 9:08:17. [SEL=0.32 J/m]) 54
Figure 5-10, Proximity of Events on filtered data (two situations where events can have a proximity below the bar-passing period) 55
Figure 5-11, Distribution of Event Proximity Using an ELR lower limit of 0.19 (Experiment S9-8. Time: 9:08:12 - 9:08:17. [SEL=0.32 J/m]) 56
Figure 5-12, Effect of Proximity Limit on Event Length Ratios (Experiment S9-8. Time: 9:08:12 - 9:08:17. [SEL=0.32 J/m]) 57
Figure 5-13, path of the sensor along a moving plate segment 59
Figure 5-14, Profile of a typical event on the first bar of a plate segment on the rotor (2nd order Butterworth notch filter) 59
Figure 5-15, Bar Labelling Procedure 61
Figure 6-1, Unfiltered Normal and Shear Forces measured in the Conflo® JC-00 refiner. Normal forces are grey, shear forces are black. (90 ms of data shown from experiment S9B1-5. Time: 9:23:21.000- 9:23:21.090. [SEL=0.47 J/m]) 65
Figure 6-2, Power spectrum of data recorded at a refiner speed of 900 rpm (Experiment S9B1-5. Time: 9:23:20 - 9:23:21 [SEL=0.47 J/m]) 66
Figure 6-3, Typical Unfiltered Normal Force Profiles (Experiment S9B1-1. Time: 9:22:52.015 - 9:22:52.017. [SEL=0.47 J/m]) 67
Figure 6-4, Typical Unfiltered Shear Force Profiles (Experiment S9B1-1. Time: 9:22:52.015 - 9:22:52.017. [SEL=0.47 J/m]) 67
Figure 6-5, Typical bar counts at each plate segment on the rotor. The horizontal axis identifies the rotor bar number (Experiment S9-1. Time: 9:06:00-9:06:05. [SEL=0.38 J/m]) 69
Figure 6-6, Normalized distribution of Normal Force Peaks [N] (Experiment S9B2-6. Time: 11:18:07-11:18:16. [SEL=0.47 J/m]) 71
Figure 6-7, Normalized distribution of Shear Force Peaks [N] (Experiment S9B2-6. Time: 11:18:07-11:18:16. [SEL=0.47 J/m]) 71

Figure 6-8, Normalized distribution of Coefficients of Friction (Experiment S9B2-6. Time: 11:18:07-11:18:16. [SEL=0.47 J/m]) 72
Figure 6-9, Normalized distribution of Shear Work [mJ] (Experiment S9B2-6. Time: 11:18:07-11:18:16. [SEL=0.47 J/m]) 73
Figure 6-10, Normalized distribution of Shear Lead [ms] (Experiment S9B2-6. Time: 11:18:07-11:18:16. [SEL=0.47 J/m]) 73
Figure 6-11, The effect of varying β in a Weibull Distribution 75
Figure 6-12, The effect of varying η in a Weibull Distribution 75
Figure 6-13, The effect of varying γ in a Weibull Distribution 76
Figure 7-1, Comparison of Median Normal Forces at Various SEL 78
Figure 7-2, Comparison of Median Shear Forces at Various SEL 79
Figure 7-3, Comparison of Median Shear Work at Various SEL 79
Figure 7-4, Comparison of the Median Coefficient of Friction at Various SEL 80
Figure 7-5, Comparison of the Median Shear Lead at Various SEL 81
Figure 7-6, Comparison of the Normal Force Distribution Shape, β at Various SEL 82
Figure 7-7, Comparison between Work measured by the sensor and Work calculated from SEL 85
Figure 8-1, Comparison of Normalized Normal Force Distributions for Each Segment (Experiment S9-1. Time: 9:06:00-9:06:05. [SEL=0.38 J/m]) 88
Figure 8-2, Comparison of Median Normal Forces for Each Plate Segment at Various SEL. 89
Figure 8-3, Comparison of Median Shear Forces for Each Plate Segment at Various SEL 90
Figure 8-4, Comparison of Median Shear Work for Each Plate Segment at Various SEL 91
Figure 8-5, Comparison of Median Normal Forces for Bar #4 on Segment #4 at Various SEL. 92
Figure 8-6, Comparison of Median Normal Forces for Bar #8 on Segment #4 at Various SEL. 93
Figure 8-7, Comparison of Median Normal Forces for Bar #12 on Segment #4 at Various SEL. 93
Figure 8-8, Normal Force Data showing the Effect of Out-of-Tram (Experiment S9B1-1. Time: 9:22:50.000-9:22:50.333. [SEL=0.47 J/m]) 95

Figure 8-9, Shear Force Data showing the Effect of Out-of-Tram (Experiment S9B1-1. Time: 9:22:50.000-9:22:50.333. [SEL=0.47 J/m]) 95
Figure 8-10, Median Normal Forces recorded at each Plate Segment (Experiment S12) 97
Figure 8-11, Median Normal Forces recorded at each Plate Segment (Experiment S9) 97
Figure 8-12, Median Normal Forces recorded at each Plate Segment (Experiment S9B1) ... 97
Figure 8-13, Median Normal Forces recorded at each Plate Segment (Experiment S9B2) ... 98
Figure A-1, Feed Rate (Experiment S9) 104
Figure A-2, Motor Load (Experiment S9) 104
Figure A-3, Specific energy (Experiment S9) 106
Figure A-4, Specific edge load (Experiment S9) 106
Figure A-5, Feed Rate (Experiment S9B1) 107
Figure A-6, Motor Load (Experiment S9B1) 107
Figure A-7, Specific energy (Experiment S9B1) 109
Figure A-8, Specific edge load (Experiment S9B1) 109
Figure A-9, Feed Rate (Experiment S9B1) 110
Figure A-10, Motor Load (Experiment S9B1) 110
Figure A-11, Specific energy (Experiment S9B2) 112
Figure A-12, Specific edge load (Experiment S9B2) 112
Figure A-13, Feed Rate (Experiment S9B2) 113
Figure A-14, Motor Load (Experiment S9B2) 113
Figure A-15, Specific energy (Experiment S12) 115
Figure A-16, Specific edge load (Experiment S12) 115
Figure B-1, Event Classifier Logic Flow Chart 117
Figure B-2, Bar Identification Main Procedure Logic Flow Chart 118
Figure B-3, "Forward Pass" Subroutine Logic Flow Chart 120
Figure B-4, "Fill Bars Forward" Subroutine Logic Flow Chart 121
Figure B-5, "Fill Bars Reverse" Subroutine Logic Flow Chart 122
Figure B-6, "Delete Resonance" Subroutine Logic Flow Chart 123
Figure B-7, "Delete Duplicates" Subroutine Logic Flow Chart 124
Figure B-8, "Count Segments" Subroutine Logic Flow Chart 125
Figure B-9, "Count Revolutions" Subroutine Logic Flow Chart 126

LIST OF TABLES

Table 3-1, Conversion factors for measuring feed rate and motor load 31
Table 4-1, General Operating Conditions 36
Table 4-2, Refining Conditions for Experiment S9 36
Table 4-3, Refining Conditions for Experiment S9B 36
Table 4-4, Refining Conditions for Experiment S12 37
Table 5-1, Event Count using Multiple Peak Fraction Values (Experiment S9-8. Time: 9:08:12 - 9:08:17. [SEL=0.32 J/m]. Bar #1 Events Removed) 58
Table 5-2, Manual Verification of Event Classification 62
Table 6-1, Occurrence Ratio of Events during Refining 70
Table 8-1, Median Forces at each plate segment (Experiment S9-1. Time: 9:06:00-9:06:05. [SEL=0.38 J/m]) 88
Table 8-2, Linear regression values for all plate segments (Normal Forces) 89
Table 8-3, regression values for all plate segments (Shear Forces) 90
Table 8-4, Linear regression values for all plate segments (Shear Work) 91
Table 8-5, Occurrence Ratio of Events for Bar #4 on Segment #4 94
Table 8-6, Occurrence Ratio of Events for Bar #8 on Segment #4 94
Table 8-7, Occurrence Ratio of Events for Bar #12 on Segment #4 94
Table 8-8, Estimated plate gap for each segment on the rotor 96
Table A-1, Calculated Sample Conditions (Experiment S9) 105
Table A-2, Calculated Sample Conditions (Experiment S9B1) 108
Table A-3, Calculated Sample Conditions (Experiment S9B2) 111
Table A-4, Calculated Sample Conditions (Experiment S12) 114
Table B-1, Bar-Labelling Tolerances for Bar-Passing and Segment-Passing periods 119
Table C-1, Normal and Shear Force Weibull Parameters (Refiner Level) 127
Table C-2, Normal and Shear Force Weibull Parameters (Experiment S9, Segments) 128
Table C-3, Normal and Shear Force Weibull Parameters (Exper. S9B1, Segments) 130
Table C-4, Normal and Shear Force Weibull Parameters (Exper. S9B2, Segments) 132
Table C-5, Normal and Shear Force Weibull Parameters (Experiment S12, Segments) 134
Table C-6, Normal and Shear Force Weibull Parameters (Bar #4) 136
Table C-7, Normal and Shear Force Weibull Parameters (Bar #8) 137
Table C-8, Normal and Shear Force Weibull Parameters (Bar #12) 138

LIST OF NOMENCLATURE

ϕ	bar angle
l	bar length
b	bar spacing
f_{bp}	bar-passing period
Δt_{BAR}	bar-passing period
k_i	calibration constant
μ	dynamic viscosity of pulp
Δt_{EVENT}	event length
ELR	Event Length Ratio
HC	high consistency pulp
LC	low consistency pulp
M_P	mass of dry wood
M_W	mass of water
F_N	normal force
$PROX$	Proximity Limit
C_m	pulp consistency
Q	refiner rotating frequency
ω	rotor angular velocity
r_i	rotor bar radius at tip of bar
D	rotor diameter at the bar tip
Δts	sampling period
F_S	shear force
W_S	shear work done over a bar-passing event
$\hat{W}$	shear work done per unit bar length
w_S	shear work done per unit bar width
s	sliding distance (event length)
SEL	specific edge load
r_o	stator bar radius at tip of bar
v	tangential velocity of the rotor at the sensor
t_{Pi}	time recorded for an event peak
τ_S	viscous shear stress
v_a	voltage from piezo A
v_b	voltage from piezo b
γ	Weibull location parameter
η	Weibull scale parameter
β	Weibull shape parameter

1 INTRODUCTION

1.1 Mechanical Pulp Refining

There are two main approaches to separating wood fibres: chemical refining and mechanical refining. To understand the difference between these two types of refining one must first understand lignin. Lignin is an amorphous phenolic polymer responsible for holding wood fibres together. Lignin is dissolved during chemical refining. A drawback to chemical refining is that the chemicals that dissolve lignin also dissolve the fibrous material. The overall yield of chemical pulp is in the range of 40-45%. Mechanical refining involves mechanically breaking the wood fibres apart from one another. In mechanical refining, therefore, the lignin remains. As a result, mechanical pulps have a considerably higher yield of 90-98% [1, 2].

Cyclical compression and shearing of the fibres are the main mechanisms of mechanical refining [1, 3]. This cycling causes the fibres to separate from one another. In addition, internal and external fibrillation[1] increases the contact surface area of the fibres for bonding and gives them greater flexibility, which makes them suitable for papermaking [1].

1.1.1 Mechanical Refiners

Mechanical refiners came into commercial production in the 1960's. Today, there are several types of mechanical refiners including single disc, double disc, twin, and conical refiners. Single disc and conical refiners have both *stator* (stationary) and *rotor* (rotating) plates. A double disc refiner operates with two rotor plates, while a twin refiner has two rotor plates, rotating around two stator plates mounted back-to-back. Schematics of these types of refiners are shown in Figure 1-1.

[1] Fibrillation refers to the brushing effect that appears on fibres with the breaking of "fibrils".

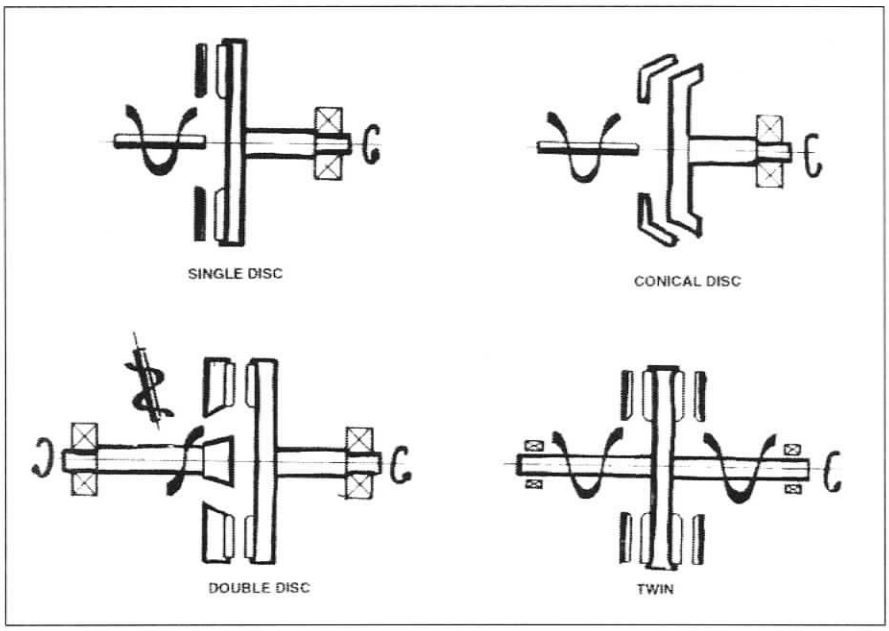

Figure 1-1, Types of mechanical pulp refiners [1]

Conical refiners have a *female* stator plate and *male* rotor plate as seen in Figure 1-2, which gives them a longer refining zone for the same given outer diameter (when compared with disc refiners). Another advantage of conical refiners is that the pressure exerted on the pulp mat is balanced in the radial direction, lowering the axial force on the rotor shaft, relative to a disc refiner.

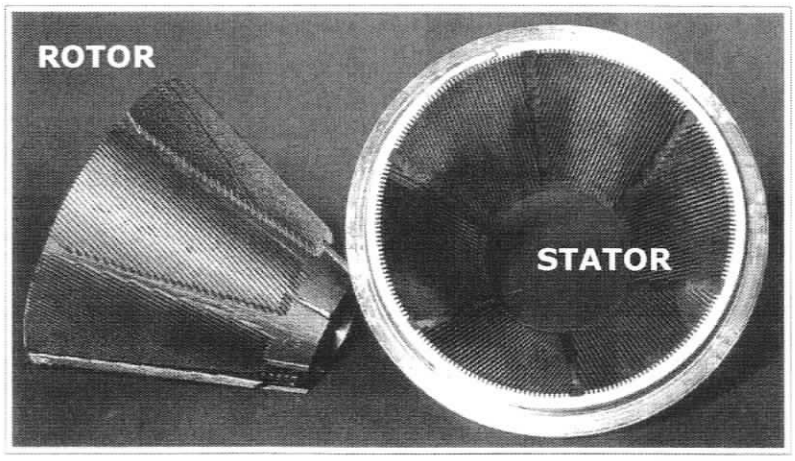

Figure 1-2, Conflo stator and rotor [4]

The mechanical refiner used during this research is a conical refiner, similar to the one shown in Figure 1-3.

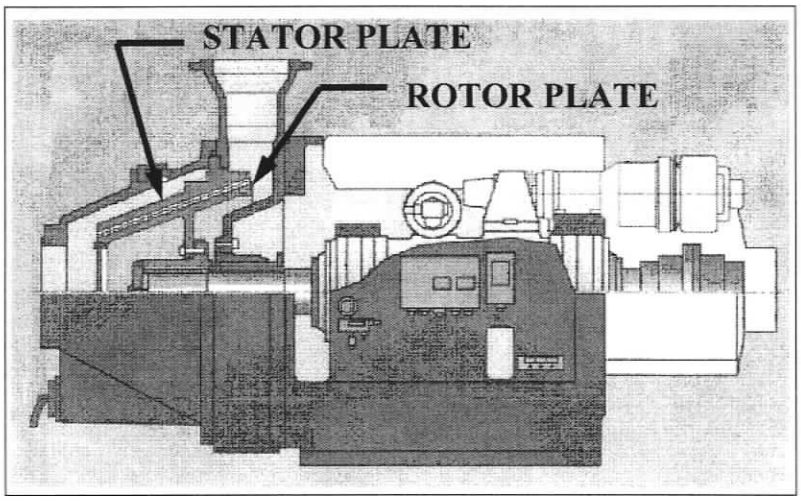

Figure 1-3, A conical refiner (Sunds Defibrator Conflo® refiner) [4]

1.2 Pulp Consistency

Wood pulp is comprised of a suspension of separated wood fibres in water. The consistency of pulp refers to the mass content of fibre present in the pulp.

The formula for the consistency of pulp is as follows:

$$C_m = \frac{M_P}{M_W + M_P} \cdot 100\% \qquad (1\text{-}1)$$

Where M_P is the mass of the dry wood fibres and M_W is the mass of the water.

Typically, pulp with a fibre content of 5% or less is considered a *low-consistency* pulp, while *high-consistency* pulps have a fibre content of 20% or greater and medium-*consistency* pulps are referred to pulp with a fibre content of 6-15% [1].

1.3 Low-Consistency Mechanical Refining

Low-consistency or LC refining is used in tertiary stage mechanical pulp refining, in addition to in stock preparation and reject refining (refining shives[2] or fibres that are too large to be accepted at the paper machine). Because LC refining operates under lower specific energies[3] than HC (High Consistency) refining, it also has lower energy costs associated with it. LC refining is excellent at removing shives, externally fibrillating the fibres, removing latency in the fibre (fibre curl), and improving fibre networking and bonding capabilities [1, 2].

1.4 Forces Measured in LC Mechanical Refining

A Number of researchers have studied forces on the bars in LC refining. Some of these studies have been experimental and some have been theoretical.

Goncharov et al. [5] developed two force sensors for measuring the conditions in an LC refiner. The first sensor was based on an L-shaped beam, the top of which protruded into the refining zone as a segment of a refining bar, as seen in Figure 1-4. Beam loading was measured with strain gauges mounted to the base of the beam. The sensor had difficulties measuring normal forces and measuring any forces under small plate gaps (the range tested was 0.01 – 0.3 mm). The accuracy of the sensor was also limited to ±2 N, and measurements could only be made at bar-passing frequencies less than 2 – 2.5 kHz. Another sensor was built by Goncharov that was capable of measuring normal and shear forces in a refiner. The second sensor had twice the accuracy of the first (±1 N) but could only measure bar-passing frequencies up to 1.3 kHz.

---

[2] Shives refer to groups of fibres that have not been broken apart into individual fibres

[3] Specific energy is the amount of energy expended per unit mass of pulp (dry mass). Specific energy is commonly expressed in kWh/t.

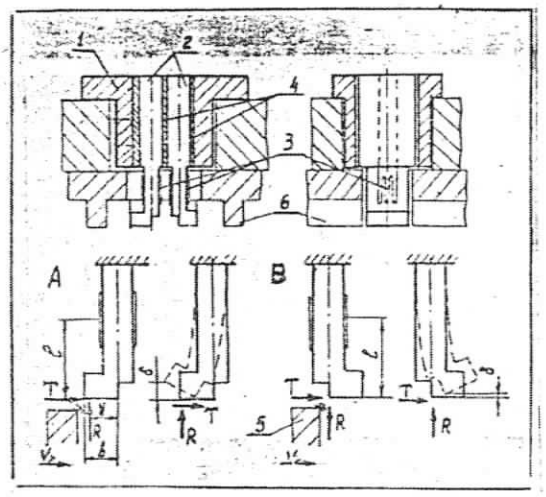

Fig. i - Sensor with L-shaped beams. 1 - body; 2 - L-shaped beams; 3 - tensiometric elements; 4 - washers; 5 - rotor blade; 6 - stator blade; A and B - diagrams for the load and deformation of the beams.

Figure 1-4 - L-Shaped Beam Force Sensor Design. Normal Force "R", Shear Force "T" [5]

Following this work, Goncharov [6] performed experiments in a disc refiner using three 2-component sensors, located along a radius of the disc (see Figure 1-5). The consistency of the stock was 2.5 – 3% and was fed through the refiner at a range of plate gaps (0.15 – 0.3 mm). Measurements of axial thrust, torque and the distribution of hydraulic pressure in the refiner were also gathered. A large pressure spike was observed at the initial stage of the bar crossing followed by a "pulling apart" stage near the end of the crossing, which can be seen in Figure 1-6. The bar widths were varied between 2 and 10 mm during the series of experiments. Goncharov concludes that most of the refining work is due to this early large spike, and further, that increasing the number of bars in the plate pattern will fibrillate the fibres more efficiently. A coefficient of friction of the fibres of 0.11 +/- 0.02 (at 720 rpm) was calculated.

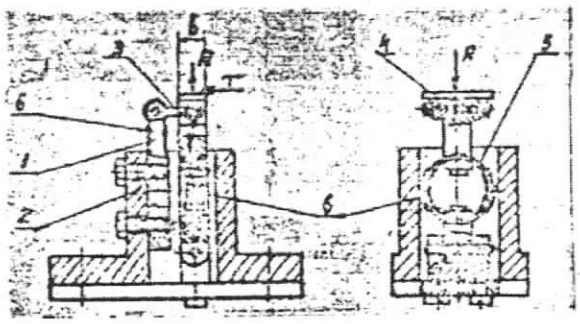

Figure 2 - Two-component sensor.

1 - flat beam; 2 - body of sensor; 3 - rod; 4 - sensor element; 5 - ring; 6 - tensiometers.

Figure 1-5, 2-Component Sensor. Normal Force "R", Shear Force "T" [5]

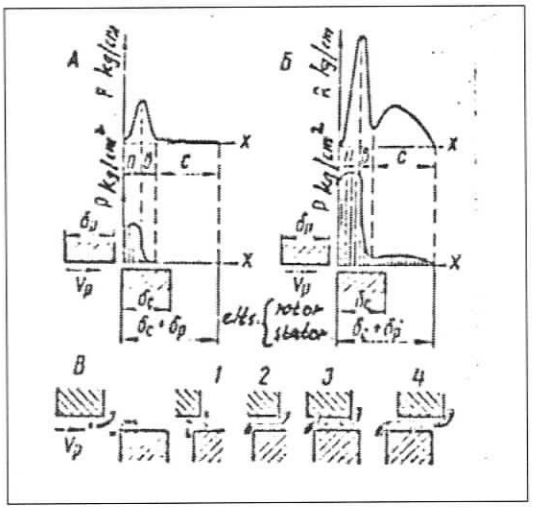

Figure 1-6, Measurements made by 2-Component Sensor. Horizontal axis represents overlap between refiner bars; vertical axis represents pressure measured by the sensor. [6]

Nordman et al. [3] equipped a small Jylhä disc refiner with transducers for the following measurements: bar clearance, inlet and outlet pressure, pressure in the grooves between the refiner bars and on the top surface of the bar, and temperature. The authors conclude that the most critical mechanisms in refining are the friction generated during fibre-fibre and fibre-bar contact, as well as transverse compression of fibre bundles.

In the laboratory, Senger and Ouelett [7, 8] used a single-bar refiner[4] to estimate the normal and shear forces on individual flocs (bundles of individual fibres) at both low and high consistencies. Studies of the forces on fibres in low consistency refining were carried out by Martinez et al. [9] and Batchelor et al. [10] using flocs of nylon fibres at a consistency of 2.5 – 3%. Normal and shear force profiles were measured using a single bar refiner at various bar gaps ranging from 0.7 – 1.3 mm. Normal forces rose to a plateau over the bar-crossing, whereas the shear force profile contained a definite peak at the onset of the impact, and can be seen in Figure 1-7. This peak was associated with a ploughing force, sometimes called a *cornering force*, as the fibre bundle is initially caught between the bars. Although the study was limited due to the polymer furnish, the theoretical model was in close agreement with the experiments and provided a useful insight into the phenomena occurring during a bar-passing event.

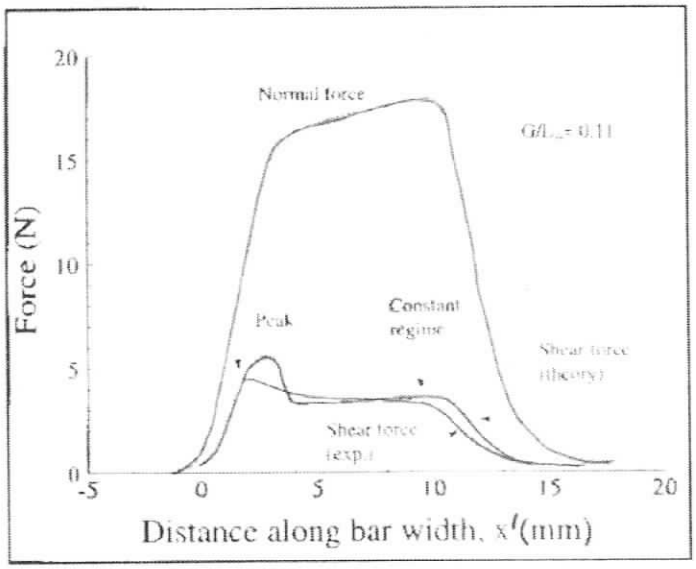

Figure 1-7, Normal and shear forces measured in a single bar refiner [10]

[4] Two horizontally mounted discs with one bar protruding from each disc. The bottom disc is stationary, while the top disc rotates. Pulp is placed on the stator bar and the forces on the floc are measured as the rotor bar passes over the stator.

Kerekes et al. [11] conducted a theoretical study of normal and shear forces and their relation to specific edge load[5]. Calculations of the forces on the individual fibres were included in the study to relate the strains on the fibres with the loading imparted from the refiner. It was concluded that the shear force on the fibres is equal to the specific edge load divided by the sliding distance of bar movement over which the force is exerted. The force exerted on the fibres depends on the amount and distribution of fibres in the gap. Kerekes et al. state that from the point of view of the refiner, torque on the motor is transmitted through the bars on the refiner. These forces are then transmitted to the individual fibres within a fibre network (i.e. a pulp floc). They conclude that friction of fibres over fibres caused by shear forces likely accounts for external fibrillation of the fibres whereas internal strain in the fibres accounts for internal fibrillation.

1.5 Refiner Tram

Studies have been conducted on the importance of disc parallelism, more commonly referred to as refiner *tram*. Mihelich et al. [12] looked at static out-of-tram in a single disc refiner and found that moderate out-of-tram (of 0.25 mm) can be tolerated but extreme tram (1.02 mm) will reduce the pulp quality considerably. In this study, no mention was made of the plate gap. However, a 1500 hp (1100 kW) 42" diameter Sprout Waldron single disc refiner was used to refine wood chips, which is quite larger than the Conflo refiner used in these trials.

Ohls and Syrjänen [13] investigated the causes of disc out-of-tram and its effects on pulp quality, concluding that tram can be minimized and thereby reducing motor load fluctuations and substantially improving average pulp properties.

Frazier [14] investigated the effects of refiner tram using hydrodynamic lubrication theory and concluded that an optimal tram angle could be found which preserves fibre length but does not increase the shive level.

---

[5] Specific edge load (SEL) is an intensity measure equal to the energy expended per unit refiner bar length over one bar-crossing, expressed in J/m.

1.6 Refiner Force Sensor Development

The development of a piezoelectric force sensor for LC refining undertaken in this work follows previous sensor developments for HC refining [15-19]. These previous sensors were designed to measure forces in disc refiners, operating with primary and secondary stage refined pulp.

The first prototype refiner force sensor, RFS1, was developed [15-17] to measure forces in a 300 mm outside diameter lab-scale refiner. The purpose of this research was to demonstrate feasibility and to investigate forces in HC refining at the bar level. RFS1 is shown in Figure 1-8.

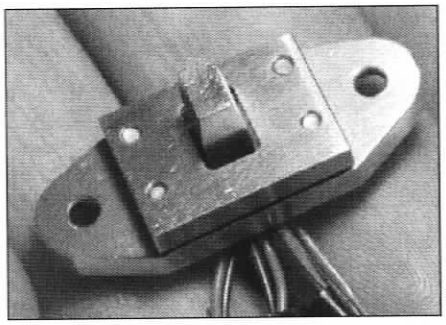

Figure 1-8, RFS1

A second prototype, RFS2 (shown in Figure 1-9) was developed for use in both Lab and Pilot scale refiners [18]. This design proved to be more robust than the previous designs and formed the basis for the third generation sensor. These sensors were used in successful trials in a 33 inch diameter pilot-scale HC refiner. The drawbacks to the design were: resonance related to high bar-passing frequencies, and susceptibility to high operating temperatures and humidity.

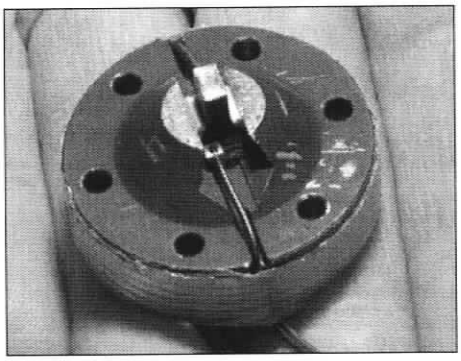

Figure 1-9, RFS2

RFS3 was developed [19] to have a higher first natural frequency than previous designs and to withstand high temperatures and humidity. Unfortunately, these sensors failed while undergoing tests in a pressurized pilot scale refiner. The sensors failed due to moisture absorption into the piezoelectric elements under high pressure, saturated steam. The high bar-passing frequencies in the Pilot scale refiner were also a concern as the lowest natural frequency of the sensor was excited. RFS3 is shown in Figure 1-10.

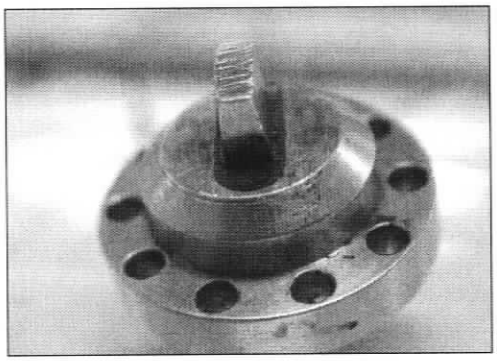

Figure 1-10, RFS3

Improving the sealing and assembly were objectives for the development of RFS4. RFS4 used o-rings for positive sealing on both the probe tip and sensor housing. Silicone was employed for sealing the sensor wires, eliminating the need for epoxy, present on previous designs. Teflon coated wires were used to withstand the harsh environment so as not to permit steam from entering the sensor between the wire and sleeve. This sensor

completed successful trials in an industrial sized refiner and thus became the basis for the sensor used in this study. Figure 1-11 shows RFS4 installed in a stator plate in an Andritz disc refiner.

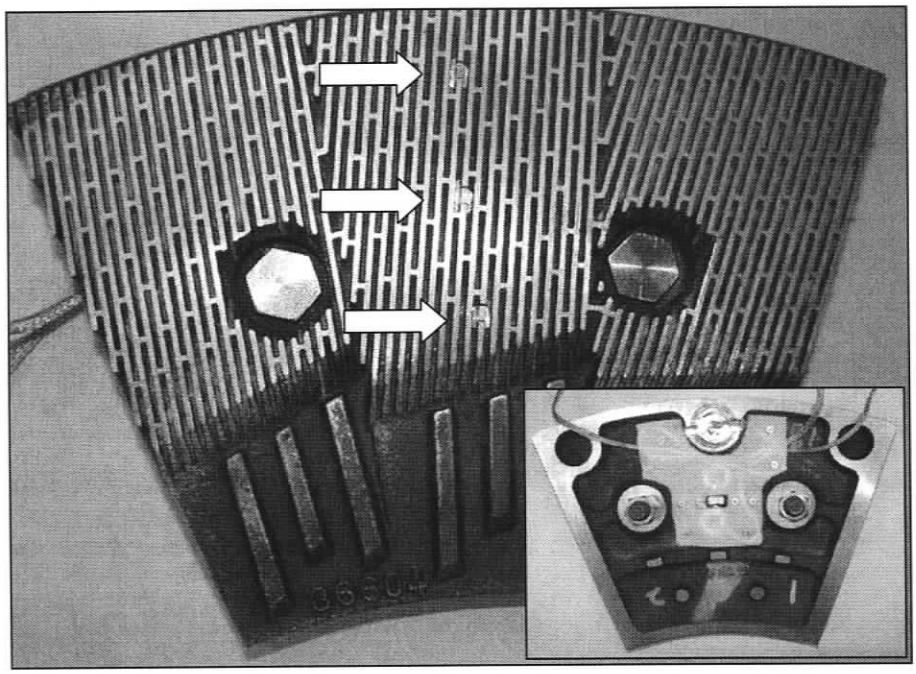

Figure 1-11, Front view of RFS4 installed in a plate segment (back view inset)

1.7 Objective

The goal of this work is to develop a sensor for LC refining by modifying RFS4 to suit the Conflo refiner geometry, to measure local normal and shear forces on the refiner bars. Distributions of these forces will be measured and related to changes in refining conditions.

1.8 Methodology and Thesis Outline

The Conflo refiner bar profile is longer than the bar profile from the Andritz refiner, used with RFS4, and a longer probe will lower the first natural frequency of the sensor.

Although the bar-crossing frequency of the Conflo is lower by comparison to the Andritz refiner, analysis of the sensor frequency response will be conducted. The details of designing a modified probe to match the profile of a bar on the stator of the refiner are discussed in Chapter 2.

The Conflo stator will need to be modified to accept the sensor while providing a method of securing and sealing the sensor once it is aligned with a stator bar. The conical shape and hardness of the stator creates difficulties with machining, therefore an intermediate assembly will be designed to seal and secure the sensor to minimize the machining on the Conflo. This experimental setup is covered in Chapter 3

In Chapter 4, the refining conditions in which the sensor probe will measure forces are described.

Due to the large amount of data that will be acquired, automated classification of the data will be used to extract forces from unwanted portions of signals recorded by the sensor. The algorithms developed for identifying bar-passing events are explained in Chapter 5.

Finally, once useful force data has been successfully identified comparisons between the force magnitudes and profiles can be made with respect to changes in refining conditions. These results and discussion are organized based on the level of analysis completed. Chapter 6 covers discussion on bar-passing event profiles measured and the corresponding event parameter distributions throughout the trials. Chapter 7 contains discussion on changes in the force magnitudes and other bar-passing event parameters with changes to specific edge load. In Chapter 8, the same analysis used in Chapter 7 is extended to the plate segment and individual bar level.

2 MODIFICATION/PREPARATION OF RFS4 FOR LC REFINING

2.1 Introduction

To instrument the Conflo® JC-00 refiner with an RFS4 sensor, modifications to the existing probe geometry were made. These modifications are described along with calibration and the experimental frequency response analysis conducted to assess the performance of the sensor.

2.2 Probe Geometry

Integration of RFS4 into the Conflo® required changing the probe tip length and width to match the Conflo® JC-00 bar geometry. The grooves on the Conflo® JC-00 are much deeper than the grooves of the plates for which RFS4 was originally designed. Figure 2-1, Figure 2-2, and Figure 2-3 show the inside of the stator where the sensor was mounted and the dimensions of the refiner bars, respectively.

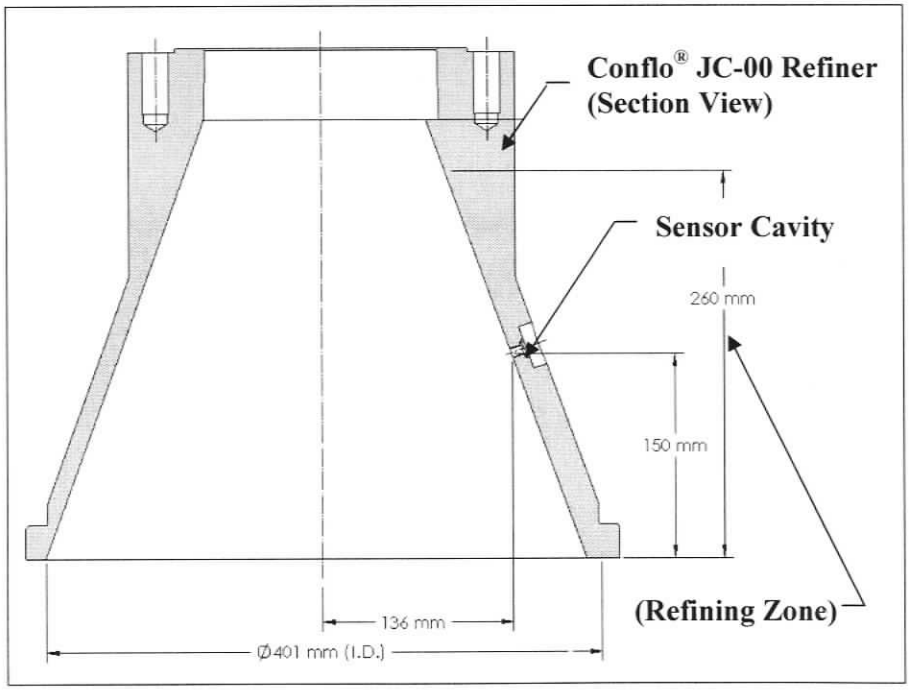

Figure 2-1, Sensor Location in the Conflo® JC-00 Stator

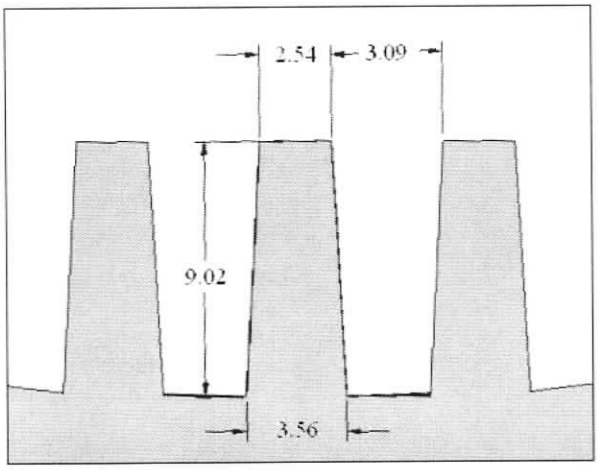

Figure 2-2, Conflo® JC-00 refiner bar geometry (dimensions in mm)

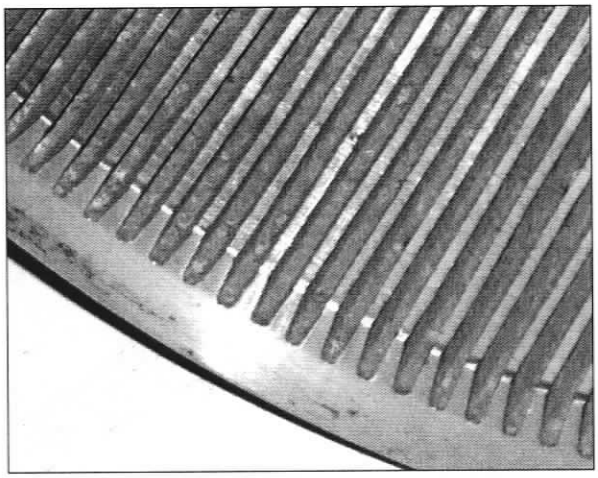

Figure 2-3, Conflo® JC-00 Stator refiner bars

To match these taller bars, the sensor probe must be longer resulting in a longer cantilevered mass and, therefore, a lower first natural frequency.

The highest bar-passing frequency, f_{BP} attainable by the Conflo® JC-00 refiner can be calculated by

$$f_{BP} = \frac{\pi DQ}{b} \qquad (2\text{-}1)$$

Where D is the rotor diameter in millimetres – where the bar-passing event occurs, Q is the refiner rotating frequency in revolutions per second and b is the bar spacing (bar width plus groove width) in millimetres.

The Conflo® JC-00 rotor has an effective bar spacing of 6.4 mm (5.63 mm bar spacing at an average bar angle of 29°), as can be seen in Figure 2-4. Its highest operating speed for trials is 1200 rpm (20 rps). The rotor diameter at the sensor location is 272 mm. This translates to a highest achievable bar-passing frequency of 2.6 kHz.

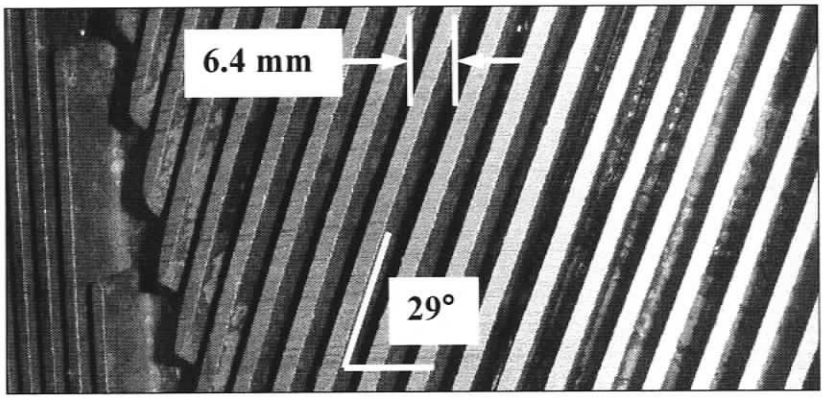

Figure 2-4, Rotor bar orientation

2.3 Frequency Response

A spare RFS4 sensor was disassembled and fitted with a modified probe tip. Frequency analysis of RFS4-LC was conducted experimentally. RFS4-LC was excited by a modal hammer while secured in a test plate that was manufactured for mounting the sensor, as shown in Figure 2-5. The two orientations in which the probe was struck were also used for calibration of the sensor.

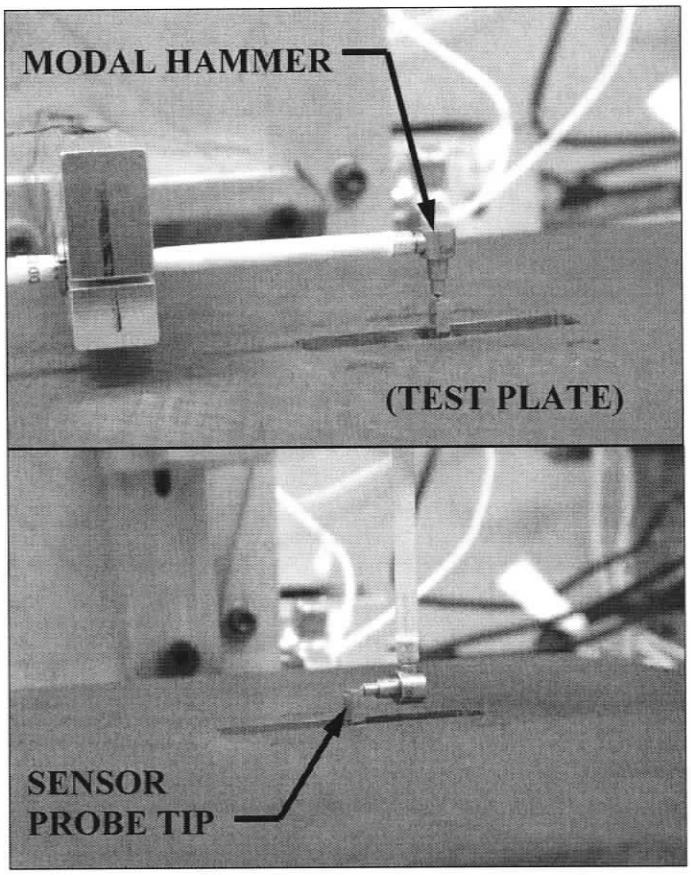

Figure 2-5, Calibration of RFS4-LC (Normal and Shear Impacts respectively)

The test plate incorporated the same mounting configuration that would occur in the stator (castellated spacer with retaining screw). Figure 2-6 shows the frequency response of RFS4-LC (twenty impacts were averaged). The lowest natural frequency of the sensor is roughly 5.6 times higher than the highest bar-passing frequency.

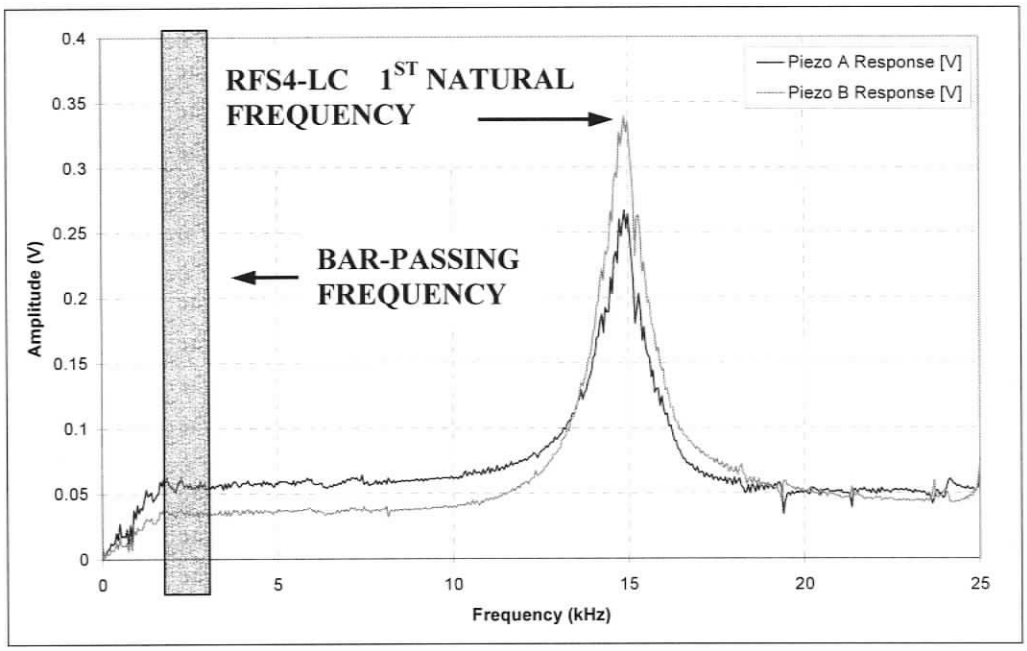

Figure 2-6, Frequency spectrum of RFS4-LC impulse response while retained in a testing plate. Piezo A is the piezoelectric element on the side of the leading edge of the sensor.

2.4 Refining Environment

During the testing at the Pulp and Paper Research Institute of Canada in Vancouver, BC; the Conflo JC-00 refiner will have an operating temperature of 60°C refining at atmospheric pressure. The sensor must be able to survive these conditions without allowing moisture to enter the sensor housing. Moisture on the piezoelectric elements will lower their dielectric strength and will affect the calibration of the piezos, making them much less sensitive and will eventually lead to sensor failure.

RFS4 was designed to withstand the harsh environment inside an Andritz 36-1CP refiner (operating temperatures of 180°C, saturated steam at 9.9 atm). The environment inside the Conflo JC-00 refiner consists of water and pulp at elevated temperatures (60°C, atmospheric). Even with a much less demanding environment for the RFS4-LC, an environmental test was completed with the sensor surviving a one hour soak in 80°C water.

2.5 Calibration

As stated earlier, the refiner force sensor was calibrated at 60°C by successive impacts with a modal force hammer on the probe tip in the normal and shear directions, giving the sensor its reference force. This is shown in Figure 2-7. A *normal* impact is applied normal to the top surface of the sensor probe. A *shear* impact is applied at 90 degrees to the normal direction along the leading edge of the probe. The leading edge refers to the edge of the probe tip that first receives an impact with a bar on the rotor during refining. The force hammer used for calibration was PCB Piezotronics #086D80/12911 with a flexible handle and no added tip or extender.

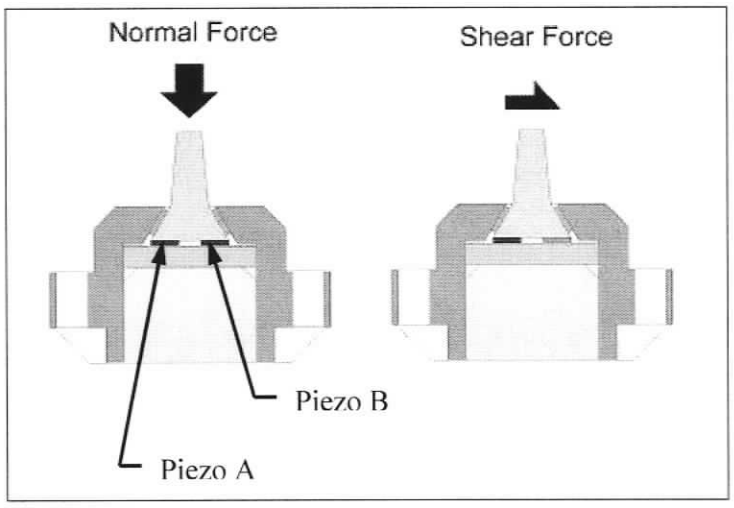

Figure 2-7, RFS4-LC Positive Directions of Impact

A custom LabVIEW program, created by Mr. Peter Byrnes, captures both the force hammer voltage response and the voltage response of the piezo elements in the sensor. Typical responses are shown in Figure 2-8.

The temperature for which each impact occurred is also recorded. The sensor is equipped with a thermocouple wire which is located in the sensor housing. The thermocouple is fed out of the sensor via one of the piezo wire ports.

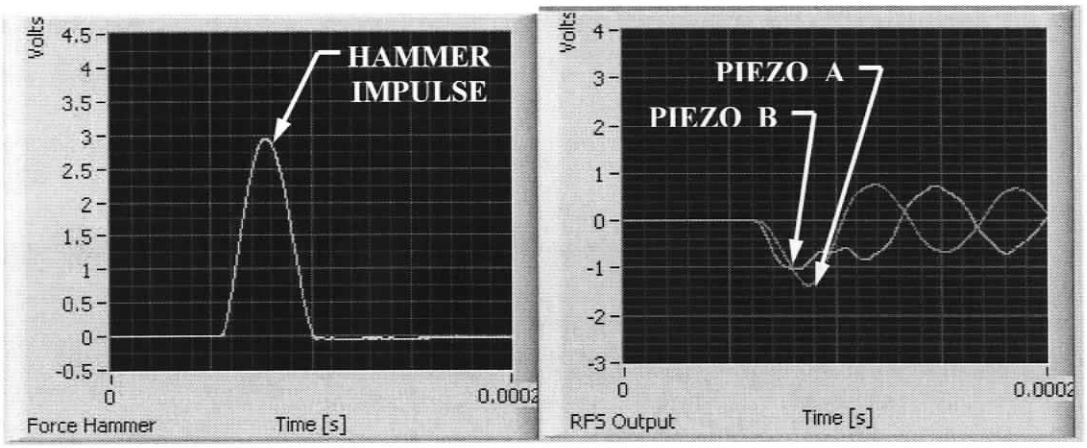

Figure 2-8, Time domain plots of force hammer response (left) and piezo voltage response (right) for RFS4-LC

The peak voltages recorded from the piezos versus the peak force applied to the probe tip are plotted and a linear regression is performed with the y-intercept of the regression line fixed to the origin, as shown in Figure 2-9 and Figure 2-10. The regression line is fixed to the origin because the piezoelectric elements will have no charge under zero strain (or during a static state since the elements are preloaded).

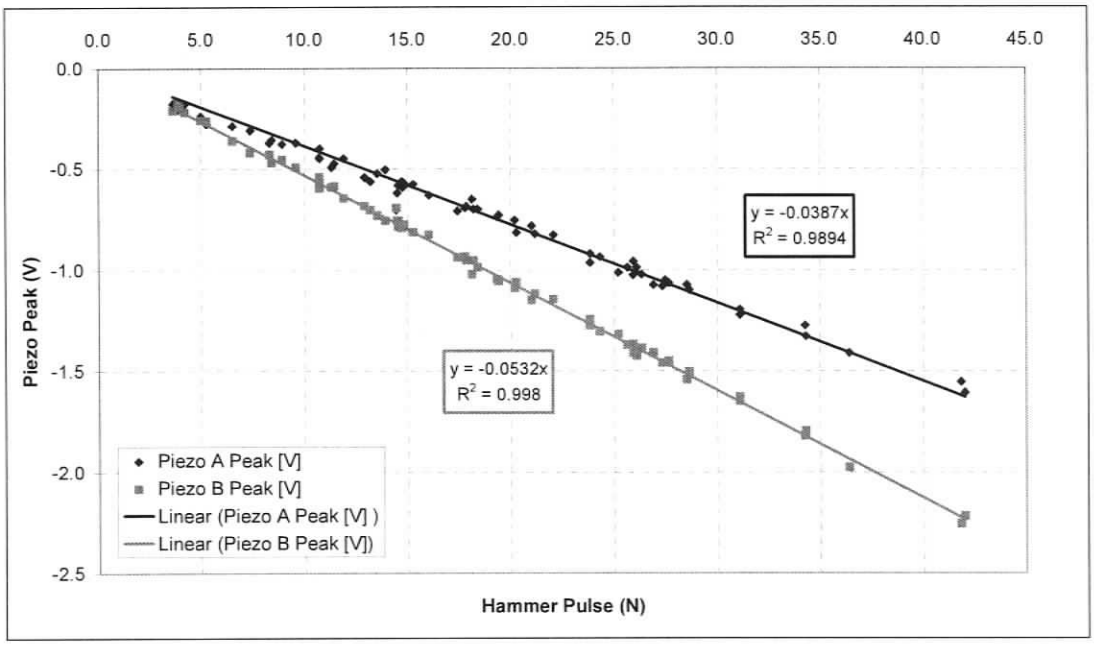

Figure 2-9, RFS4-LC Normal Impact Calibration

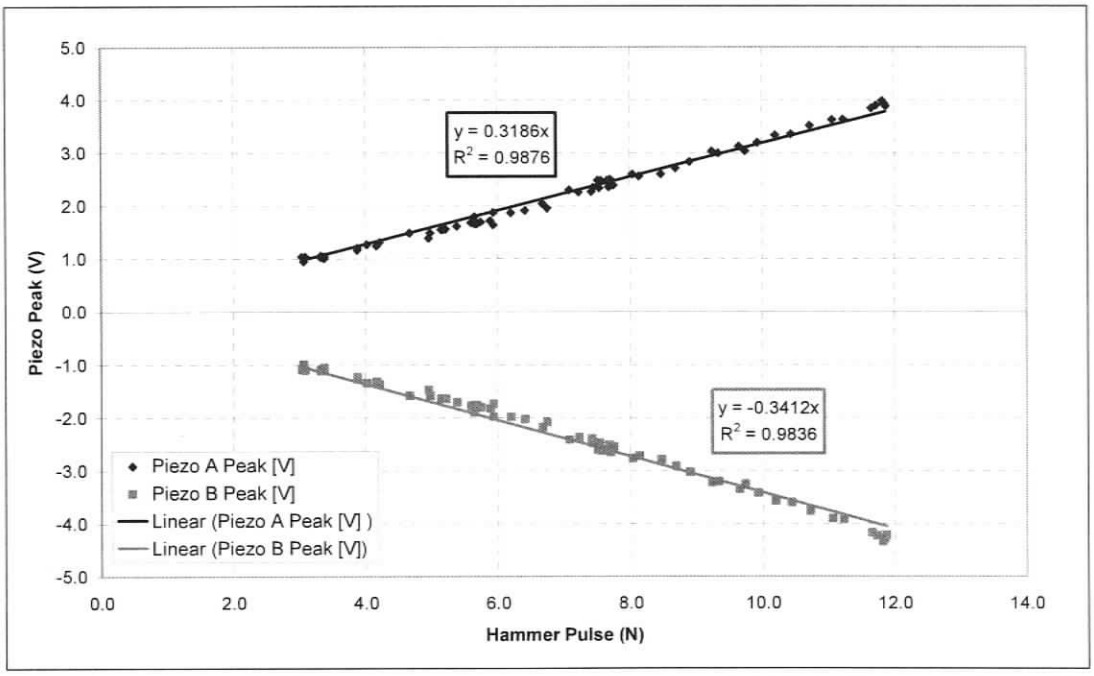

Figure 2-10, RFS4-LC Leading Edge Shear Impact Calibration

The slopes of the lines are recorded as the calibration constants: k_1, k_2, k_3, k_4. These values are given in the units [V/N]. The first two constants correspond to normal impacts and the remaining two correspond to shear impacts.

Assuming superposition, the voltages measured will be,

$$\begin{aligned} v_A &= k_1 \cdot F_N + k_3 \cdot F_S \\ v_B &= k_2 \cdot F_N + k_4 \cdot F_S \end{aligned} \qquad (2\text{-}2)$$

Where v_A is the voltage measured from Piezo A and v_B is the voltage measured from Piezo B.

In matrix format, the previous equation appears as such:

$$\begin{bmatrix} v_1 \\ v_2 \end{bmatrix} = \begin{bmatrix} k_1 & k_3 \\ k_2 & k_4 \end{bmatrix} \begin{bmatrix} F_N \\ F_S \end{bmatrix} \qquad (2\text{-}3)$$

The calibration formulas are then inverted to obtain both the normal and shear forces from the peak voltages of each piezoelectric element. These formulas will be referred to as the normal and shear *sensitivity equations*.

$$\begin{bmatrix} F_N \\ F_S \end{bmatrix} = \frac{1}{\det[k]} \begin{bmatrix} k_4 & -k_3 \\ -k_2 & k_1 \end{bmatrix} \begin{bmatrix} v_1 \\ v_2 \end{bmatrix}$$

$$F_N = \frac{1}{k_1 k_4 - k_3 k_2} \left(k_4 v_1 - k_3 v_2 \right) \qquad (2\text{-}4)$$

$$F_S = \frac{1}{k_1 k_4 - k_3 k_2} \left(-k_2 v_1 + k_1 v_2 \right) \qquad (2\text{-}5)$$

For example, with the calibration constants:

$$\left.\begin{aligned} k_1 &= 0.1977 \\ k_2 &= 0.1977 \\ k_3 &= -0.7265 \\ k_4 &= 0.7286 \end{aligned}\right\} \text{[V/N]}$$

The Normal and Shear force sensitivity equations are calculated respectively:

$$\left.\begin{aligned} F_N &= 2.5327 \cdot v_A + 2.5254 \cdot v_B \\ F_S &= -0.6872 \cdot v_A + 0.6872 \cdot v_B \end{aligned}\right\} \text{[N/V]}$$

This method of calibration was developed for RFS1 [15], has been validated [16] and has been used on sensors RFS1 – RFS4.

2.6 Summary

RFS4 was altered to have a longer probe for measurements in a Conflo® JC-00 refiner. The sensor was calibrated in both the normal and shear direction using a modal hammer. Experimental analysis was conducted to characterize the sensor behaviour at various frequencies to determine whether the lowest natural frequency of the sensor would be excited in the refiner. It was found that the lowest natural frequency of the sensor in a mounted configuration is 15kHz. This is approximately 5.6 times greater than the highest bar-passing frequency of the refiner.

3 EXPERIMENTAL SETUP

3.1 Introduction

Experiments aimed at measuring refining forces in a low-consistency refiner were conducted at the Pulp and Paper Research Institute of Canada in Vancouver, BC. The refiner used for these experiments was a Sunds Defibrator Conflo® JC-00 conical refiner. In this chapter, hardware and software preparations that were made for the trials are discussed.

3.2 Sensor Installation into the Conflo® JC-00 Stator

To install the sensor into the Conflo® JC-00 stator, a pocket was bored into the stator, centred on a refiner bar. A sleeve was then machined to press into this pocket. The sleeve allowed the sensor to be sealed in place using an o-ring so water and pulp could not escape around the sensor; while allowing the sensor to be aligned and oriented with a rotor bar accurately and secured firmly in place. Figure 3-1 and Figure 3-3 show the sensor installed in the Conflo refiner from the inside and outside, respectively. Figure 3-2 shows an exploded view of the sensor assembly.

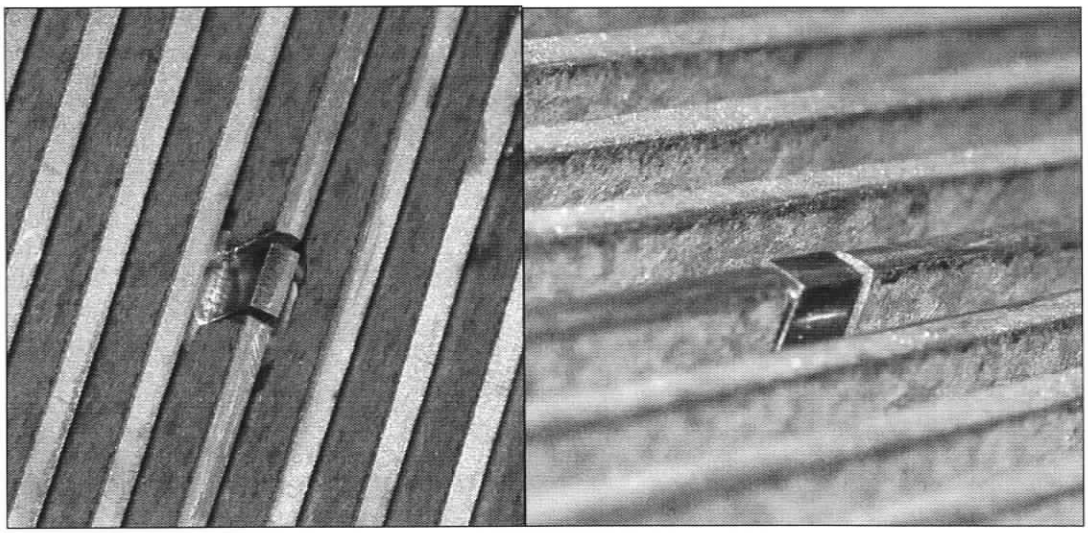

Figure 3-1, RFS4-LC installed in the Conflo® JC-00 Stator (inside view)

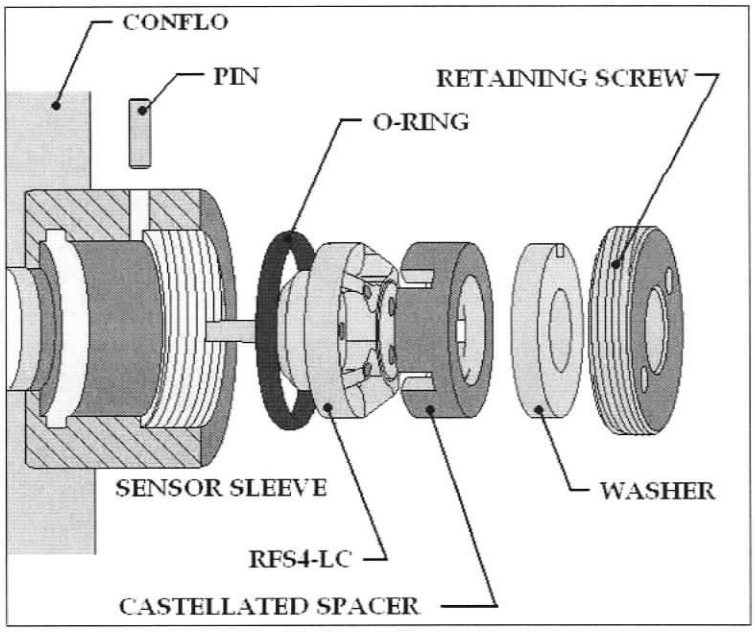

Figure 3-2, Exploded view of RFS4-LC assembled in the sensor sleeve

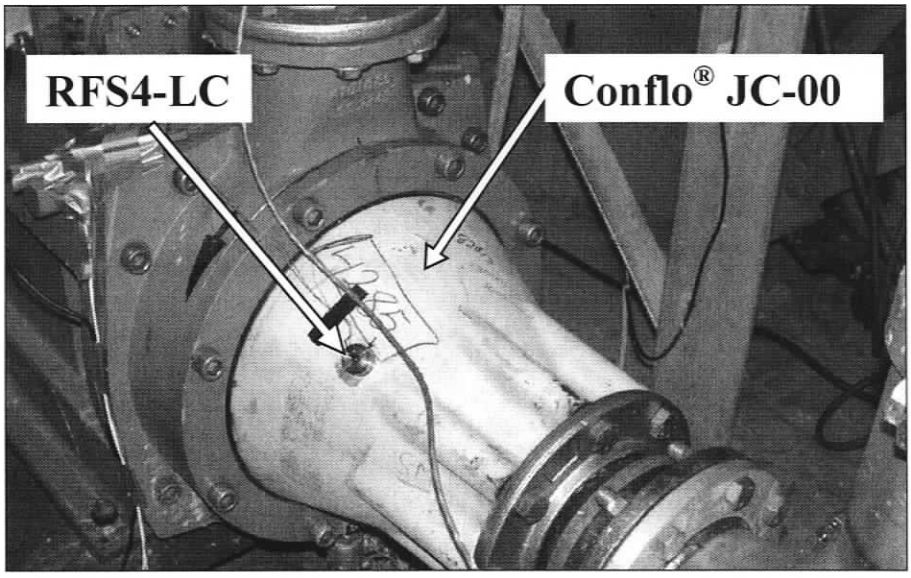

Figure 3-3, RFS4-LC installed in the Conflo® JC-00 Stator (outside view)

3.2.1 Sensor Sleeve

At the bottom of the sleeve, the sensor is located axially and is able to be sealed using an o-ring groove, as shown in Figure 3-2. The castellated spacer locates on the back of the sensor

housing. The washer located between the castellated spacer and the retaining screw inhibits the transmission of torque to the sensor when tightening the retaining screw. If torque was allowed to be transmitted to the sensor, the sensor would rotate in the stator and would misalign with the refiner bars. A hole in the side of the sleeve allows a pin to be inserted to locate with the slot on the washer. Once the retaining screw is tightened and the sensor is located and fastened, the pin is removed.

3.2.2 Machining of the Stator

A custom alignment fixture was designed to centre the sensor pocket on a refiner bar. This fixture consisted of a locating base plate for the stator with a removable angled alignment plate, as seen in Figure 3-4. Pins located in the plate centred the stator on the fixture. The Conflo stator was placed on the plate and rotated until a refiner bar aligned with the angled alignment plate. Since the stator bars are parallel to one another on a conical surface, the bar angle[6] is different for each bar. A bar on the stator with zero bar angle was chosen for the sensor location since it was parallel with the alignment plate. Figure 3-5 shows the angled alignment plate aligned with a stator bar with zero bar angle. Once aligned, the outside of the stator was marked around its base so that when removed, the stator could be returned to its original location.

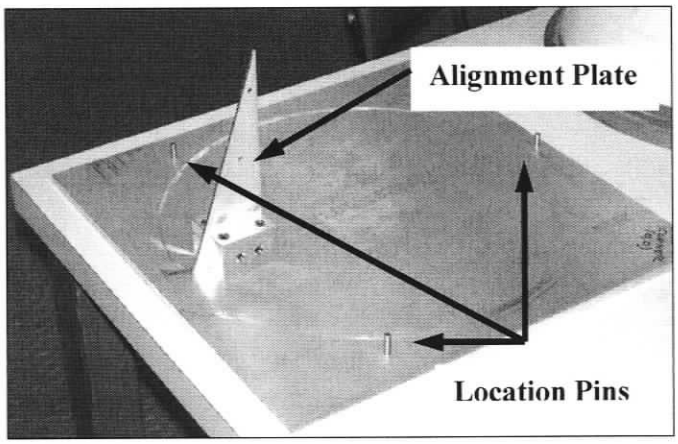

Figure 3-4, Alignment fixture for locating the bars on the Conflo® JC-00 stator

[6] The *bar angle* is the angle in the tangent plane (tangent to the cone) between the bar and a line that intersects the cone axis.

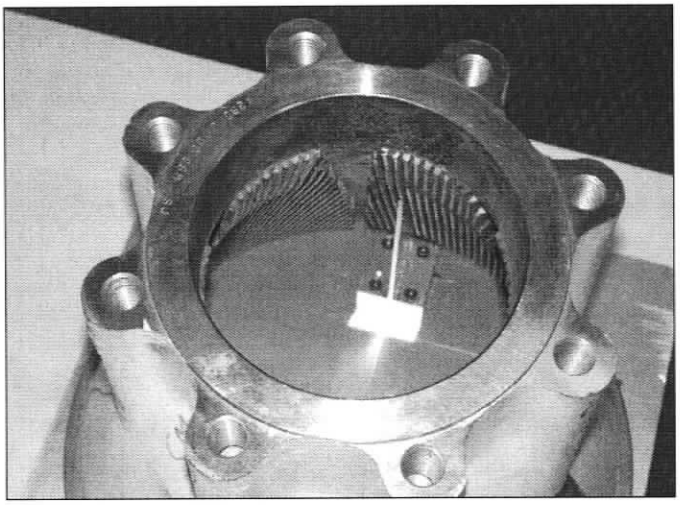

Figure 3-5, Alignment fixture in place on the Conflo® JC-00 stator (alignment plate aligned with a stator bar)

With the stator removed, the boring tool was located to the centre of the alignment plate. The stator was then returned to its previous location so the pocket could be bored accurately into the casting material. Figure 3-6 and Figure 3-7 show the alignment of the boring tool and machining of the stator plate, respectively. With the pocket machined in the stator, the sleeve was pressed into position.

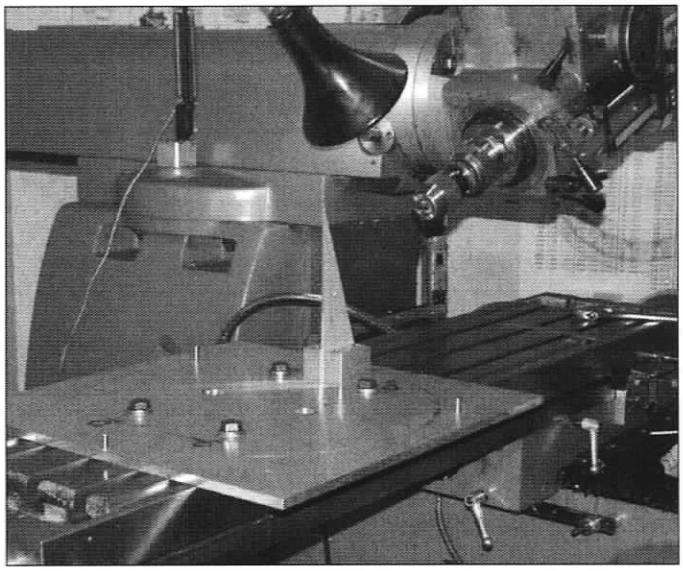

Figure 3-6, Aligning the boring tool to the alignment plate

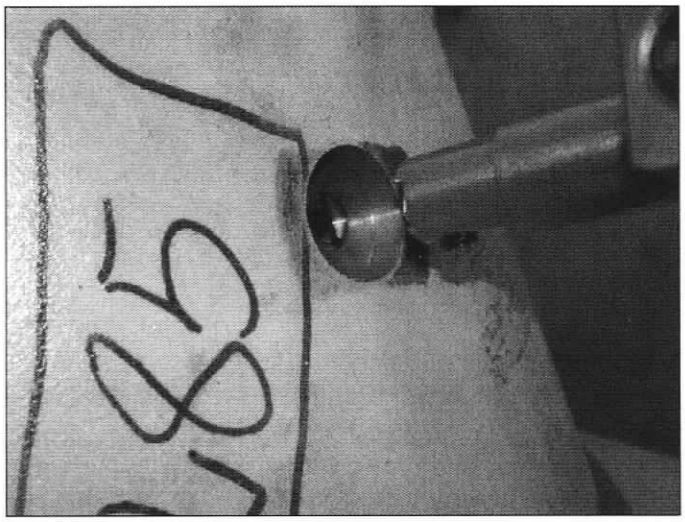

Figure 3-7, Machining of pocket into the Conflo® JC-00 stator

3.3 Data Acquisition

In this section, the equipment used for the acquisition of data during the refining trials at the Pulp and Paper Research Institute of Canada Vancouver laboratory is discussed. Figure 3-8 shows the setup of the data acquisition equipment and Figure 3-9 shows the instrumented refiner. Figure 3-10 shows a schematic of the equipment setup.

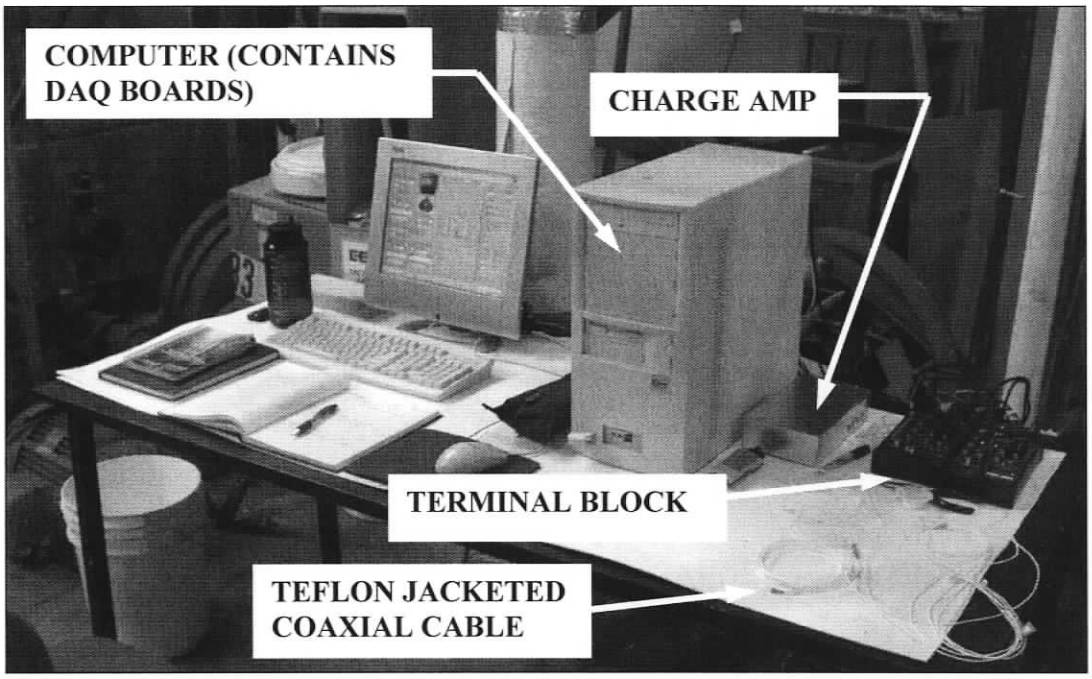

Figure 3-8, Workstation (showing data acquisition hardware) during refining trials (Pulp and Paper Research Institute of Canada – Vancouver, BC)

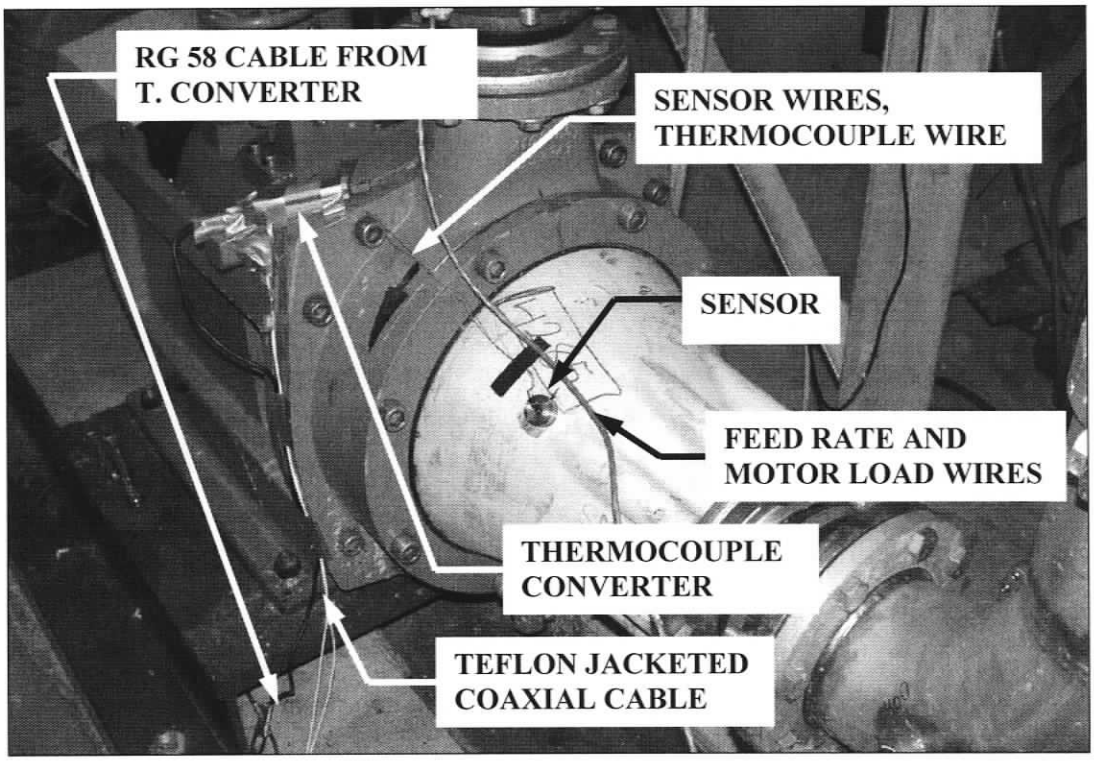

Figure 3-9, Instrumented Conflo® JC-00 refiner

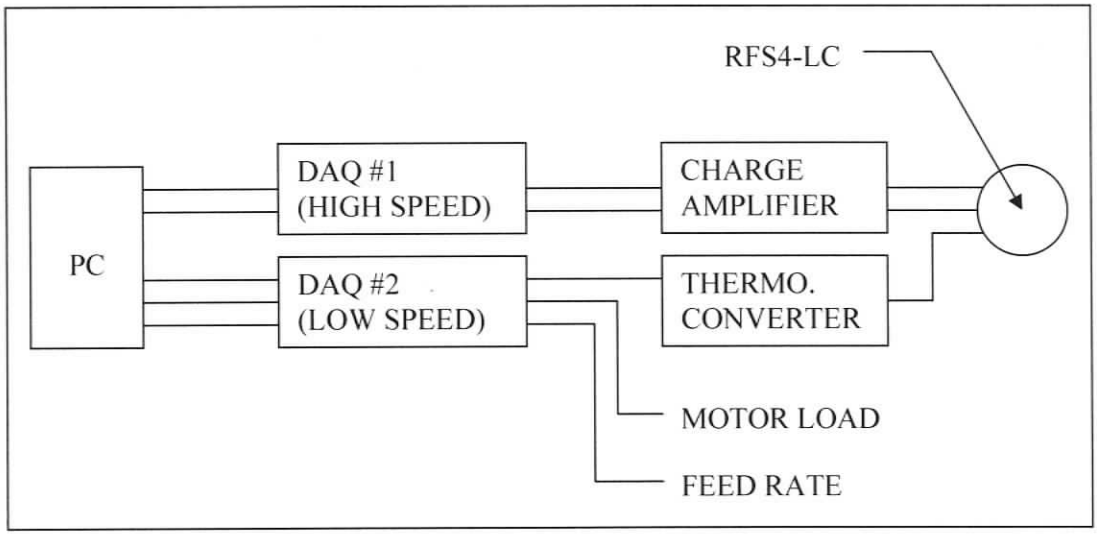

Figure 3-10, Data acquisition schematic

3.3.1 Charge Amp

A custom charge amplifier was designed Dr. Rolf Lueck and built by Mr. Kevin Jones, to suit measurements from the LC sensor in the Conflo under the given operating conditions. The charge amplifier converts the charge signals produced by the sensor to a voltage signal required by the data acquisition boards. The cut-off frequency of the charge amplifier was designed to be over 100 times lower than the lowest bar-passing frequency of 2.0 kHz to minimize measurement error due to signal decay. With a cut-off frequency of 100 Hz, the time constant of the amplifier (time for the signal to decay to 37% of its original value) is 1.6 ms. The bar-passing periods at 900 rpm and 1200 rpm are 0.50 ms 0.38 ms, respectively. To reduce the potential for electromagnetic noise arising from the laboratory, the amplifier is powered by two 9V DC batteries.

One drawback to the sensor and charge amp is that low frequency signals are not detected. When looking at the amplifier's transfer function in Figure 3-11, it is apparent that any signal with a frequency below 100 Hz is reduced drastically. This means that if constant (or DC) force signals exist; they will not be detected by the sensor.

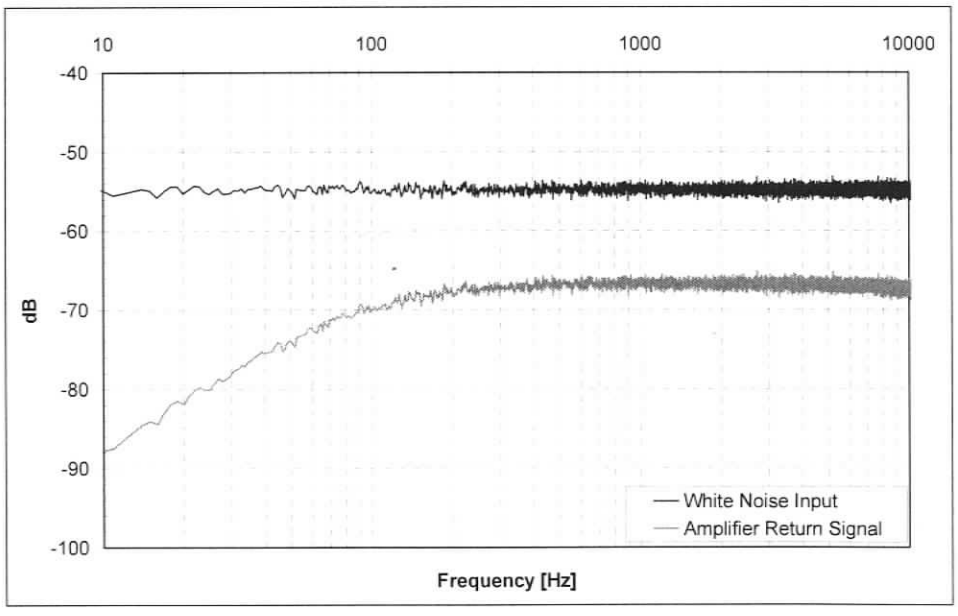

Figure 3-11, Plot of the charge amplifier's transfer function

3.3.2 High/Low-Speed DAQ Boards

Two data acquisition boards were used to obtain data during these trials. The DAQ boards convert the amplified analog signals from the piezos to a digital signal. Both boards have 12 bit resolution meaning that with an amplifier range of +/- 10 V, the resolution of the data acquired is +/- 2.5 mV across this range. A National Instruments NI PCI-6110, 5 MS/s, 12-Bit, 4 Analog Input Simultaneous-Sampling Multifunction DAQ was used to obtain the higher speed signal, required for sensor measurement. There were two signals acquired from the sensor (one for each piezo) at a sampling frequency of 100 kS/s. The sampling rate of 100 kS/s was chosen based on the maximum bar-passing frequency of the trials (at 1200 rpm) of 2.67 kHz. 100 kS/s amounts to 37 sample points per bar-passing event.

Data from the thermocouple, the motor load, and the feed rate were acquired using a National Instruments NI PCI-6023E, 200 kS/s, 12-Bit, 16 Analog Input Multifunction DAQ. The low speed board acquires data at a sampling rate of 100 S/s, much lower than the board's sampling capability.

Both the feed rate and the motor load were received as 4-20 mA signals. The feed rate signals were converted to voltages, over a range of 1-5 V using a 249 ohm resistor and the motor load voltage range was 0.4-2 V using a 100 ohm resistor. Table 3-1 shows the conversion factors for feed rate and motor load. The relationship between both the feed rate and motor load and the voltages acquired is linear.

Table 3-1, Conversion factors for measuring feed rate and motor load

Current [mA]	Voltage [V]	Feed Rate [l/min]	Current [mA]	Voltage [V]	Motor Load [kW]
4	1	0	4	0.4	0
20	5	2617	20	2	100

3.3.3 Terminal Blocks

Two National Instruments NI BNC-2110, Shielded Connector Blocks were used for connecting the high-speed DAQ board with the charge amplifier, and low-speed DAQ board to the incoming feed rate, motor load and thermocouple wires.

3.3.4 Sensor Wiring

Feeding out of the sensor housing are four-32 AWG stranded Teflon coated wires (two per piezoelectric element) and one thermocouple wire (discussed later). The four piezo wires connect to Dytran 6010A, Teflon jacketed coaxial cables (10' length) via #10-32 connectors and attach to the charge amp on the other end also via #10-32 connectors. The Teflon coating on the cables and wires ensure that moisture from around the refiner does not permeate into the wires, while the #10-32 connectors are equipped with o-rings for positive sealing at the ends. The Dytran cables are attached as close to the senor as practically possible to reduce electromagnetic noise from the laboratory environment. The 32 AWG stranded Teflon coated wires from the sensor are twisted in pairs to reduce the effects of electromagnetic noise.

The cables leading out the charge amp are standard RG 58 coaxial cable with BNC connectors, which feed into the terminal blocks.

3.3.5 Thermocouple

The thermocouple used during the trials is an Omega 5TC-TT-T-36-144 copper-constantan, (36 gauge PFA Teflon coated wires, 144" length). This thermocouple wire is T-type calibrated, making it suitable for operation at a temperature range of -200°C-350°C in an environment with moisture present. The temperature is measured at an accuracy of +/- 1.1°C (at 25°C). A change of 1 mV of signal corresponds to a temperature change of 1°C. The thermocouple wires connect to an Omega SMCJ-T analog-to-digital converter which connects to the terminal block through RG 58 coaxial cable via BNC connectors.

3.3.6 Virtual Instrument for Data Acquisition

The data is acquired using a custom-built program designed by Mr. Peter Byrnes. The front panel of the program is shown in Figure 3-12.

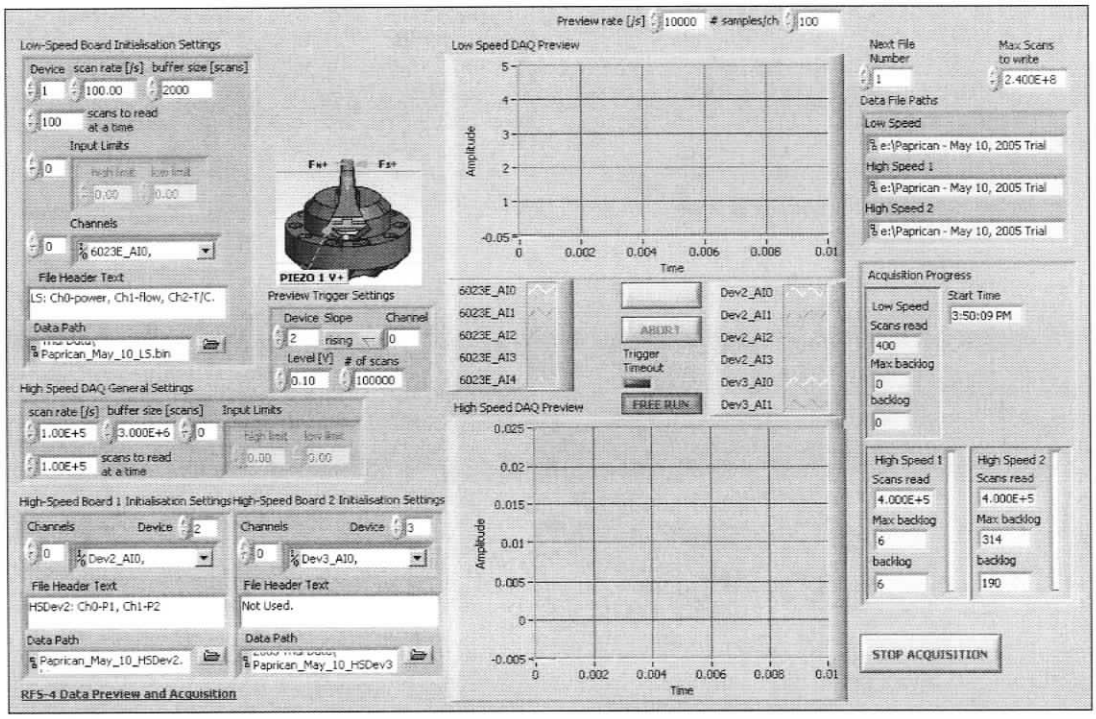

Figure 3-12, Data acquisition software front panel display

3.4 Summary

The stator on the Conflo® JC-00 refiner was machined to allow for RFS4-LC to be accurately aligned with a refiner bar for measuring forces occurring inside the refiner during operation. A sleeve was machined to press into the hole bored in the Conflo to secure and provide sealing to RFS4-LC. The sleeve accommodates design changes to the sensor without having to alter the stator.

A custom charge amplifier was designed for the type of sensor and the refining environment. To minimize electromagnetic noise from the laboratory environment, the amplifier was isolated from any power sources by using batteries. Protection from moisture was a key concern with the wiring and components located around the refiner; connections with o-rings and Teflon coated wires were used. Refiner data including forces, temperature, motor load and feed rate are able to be obtained using a custom Virtual Instrument for data acquisition.

4 EXPERIMENTAL PROCEDURE

4.1 Introduction

The operating conditions of the trials performed will be discussed in this chapter, along with the pulp used. An explanation of how the operating conditions were adjusted and the implications of these adjustments are examined.

4.2 Pulp Furnish

Three trials were performed on the Conflo® JC-00 refiner at the Pulp and Paper Research Institute of Canada's Vancouver Laboratory. All experiments followed similar procedures, all using CTMP (Chemi-Thermo Mechanical Pulp) preheated to 60°C, fed through the refiner at atmospheric pressure. The pulp was disintegrated, and then added to the *Stock* chest where it was diluted to a consistency of 3.15%. The pulp then travelled through the refiner where it was then deposited into the *Accept* chest, as shown in Figure 4-1. The *Reject* chest contains pulp from previous refining stages that still requires further refining and was not used during these experiments.

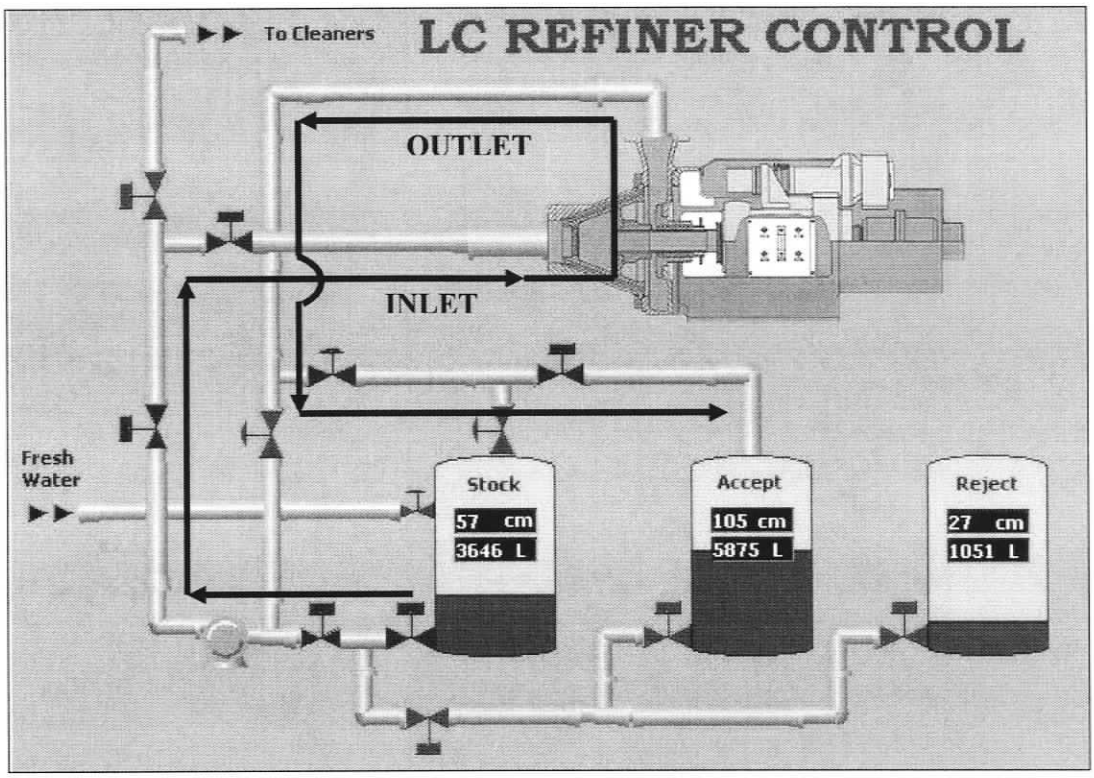

Figure 4-1, Schematic of the refiner showing the direction of pulp flow [20]

4.3 Target Refining Conditions

The objective of the experiments was to refine the pulp over a range of specific energies (0, 40, 60, 80, 100 kWh/t), at two different speeds (900, 1200 rpm) and two different specific edge loads (0.33, 0.50 J/m). A summary of the experiments is shown in Table 4-1 to Table 4-5. To achieve the desired specific energy the flow rate was adjusted while maintaining a constant motor load. Figure 4-2 shows the target refining conditions graphically.

Table 4-1, General Operating Conditions

Furnish:	CTMP (Chemi-Thermo Mechanical Pulp)
Stock Consistency:	3.15%
Operating Temperature:	60°C
Operating Pressure:	Atmospheric
Plate Factor[7]:	5.2 [km/rev]

Table 4-2, Refining Conditions for Experiment S9

Experiment	S9				
Refiner Speed	900	[rpm]	Target SEL[8]	0.33	[J/m]
Gross Power	43.9	[kW]	CEL[9]	78	[km/sec]
No Load Power	18.2	[kW]			

Sample Code	Feed Rate [L/min]	Energy Level [kWh/t]
S9-0	--	0
S9-40	340	40
S9-60	227	60
S9-80	170	80
S9-100	136	100

Table 4-3, Refining Conditions for Experiment S9B

Experiment	S9B				
Refiner Speed	900	[rpm]	Target SEL	0.50	[J/m]
Gross Power	57.2	[kW]	CEL	78	[km/sec]
No Load Power	18.2	[kW]			

Sample Code	Feed Rate [L/min]	Energy Level [kWh/t]
S9B-0	--	0
S9B-40	516	40
S9B-60	344	60
S9B-80	258	80
S9B-100	206	100

[7] The *plate factor* is a length of all the rotor-stator bar-crossings over one revolution of the rotor.
[8] *SEL* (Specific edge load) is calculated by dividing the motor power by the Cutting Edge Length.
[9] *CEL* (Cutting Edge Length) is equal to the *plate factor* multiplied by the rotor frequency (in rev/s).

Table 4-4, Refining Conditions for Experiment S12

Experiment	S12				
Refiner Speed	1200	[rpm]	Target SEL	0.33	[J/m]
Gross Power	69.8	[kW]	CEL	104	[km/sec]
No Load Power	35.5	[kW]			

Sample Code	Feed Rate [L/min]	Energy Level [kWh/t]
S12-0	--	0
S12-40	454	40
S12-60	303	60
S12-80	227	80
S12-100	182	100

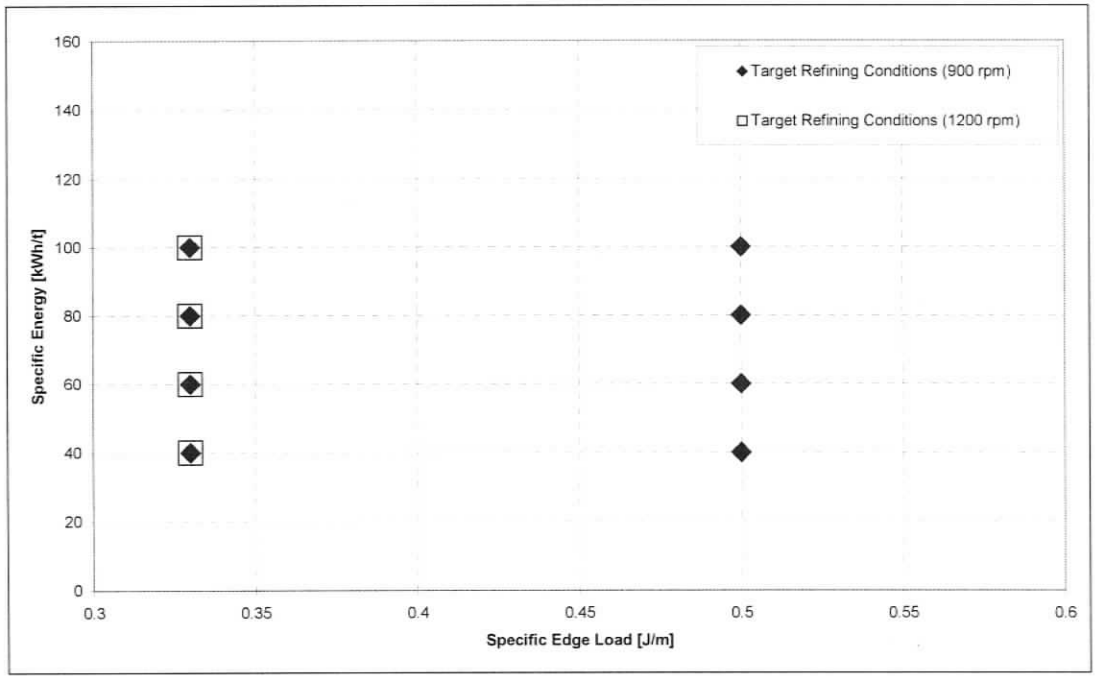

Figure 4-2, Target refining conditions for comparison with sensor data. Experiments at 900 rpm conducted at SELs of 0.33 J/m and 0.5 J/m, 1200 rpm conducted at an SEL of only 0.33 J/m.

4.4 Actual Refining Conditions

Stable operating conditions were not achieved at each of the prescribed operating conditions. Data obtained from the trials showed that there were large fluctuations in the motor load and the feed rate throughout the experiment. The feed rate and motor load for the first experiment (S9) are shown in Figure 4-3 and Figure 4-4, with the remaining refining conditions included in Appendix A.

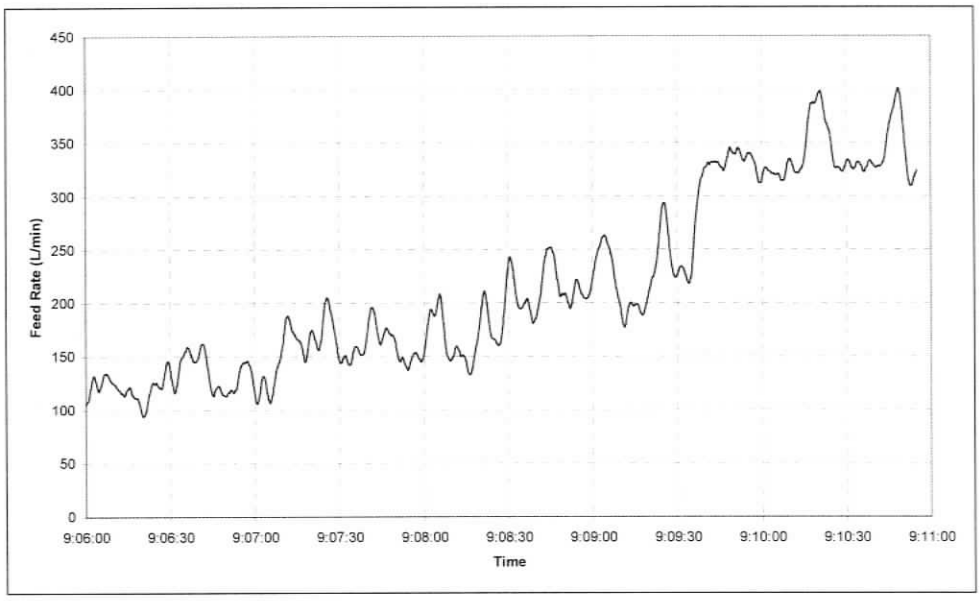

Figure 4-3, Feed Rate during experiment S9 (applying a forward moving average filter of 100 points and a reverse moving average filter of 100 points)

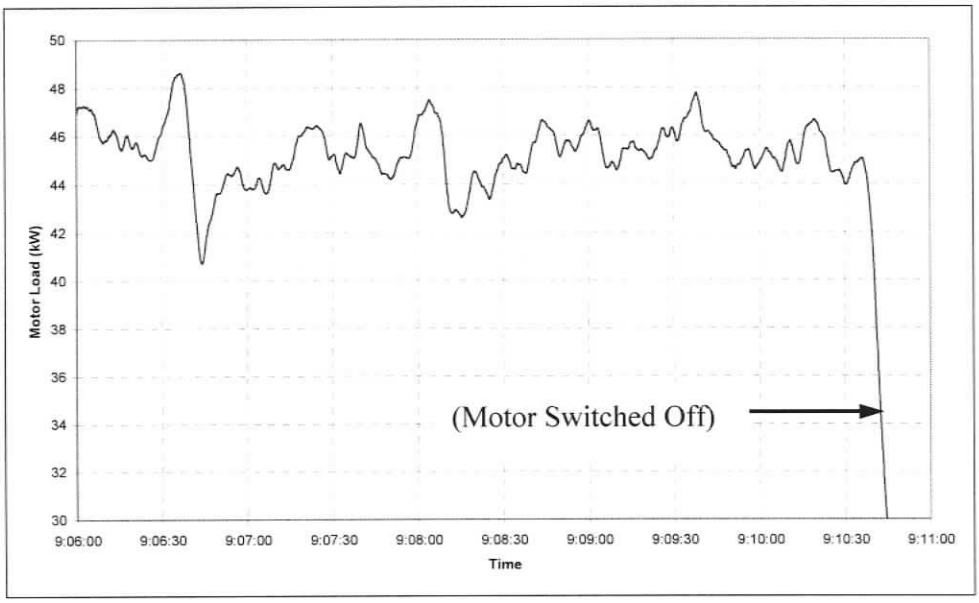

Figure 4-4, Motor Load during experiment S9 (applying a forward moving average filter of 100 points and a reverse moving average filter of 100 points)

To compare forces measured by the sensor on the basis of operating conditions, only time periods that had a relatively constant specific edge load were analysed. These time periods are shown visibly in Figure 4-5. All of the recorded sample times are summarized in Tables A-1 through A-4 of Appendix A. There are nine data samples taken for each experiment. The first set of experiments operating at 900 rpm with a specific edge load of 0.5 J/m, originally labelled as S9B – now designated S9B1, were repeated. The repeat run was designated S9B2.

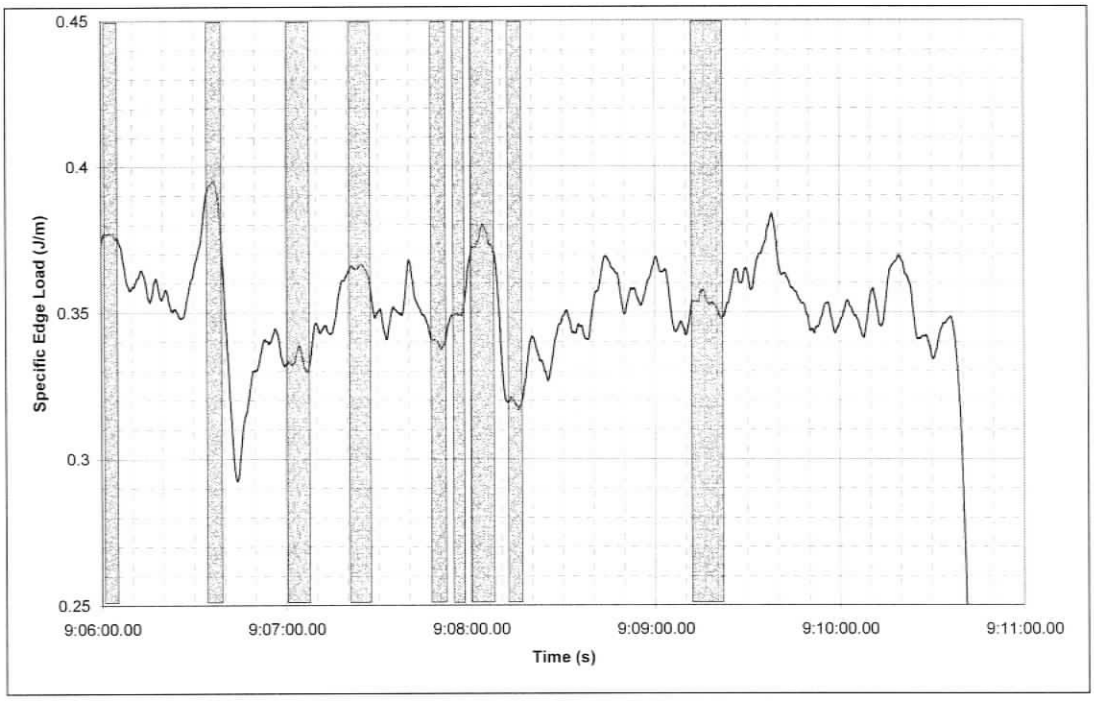

Figure 4-5, Specific edge load. Samples were extracted for analysis from grey regions. (Experiment S9)

Figure 4-6 summarizes both the specific edge loads and specific energies for all the samples taken.

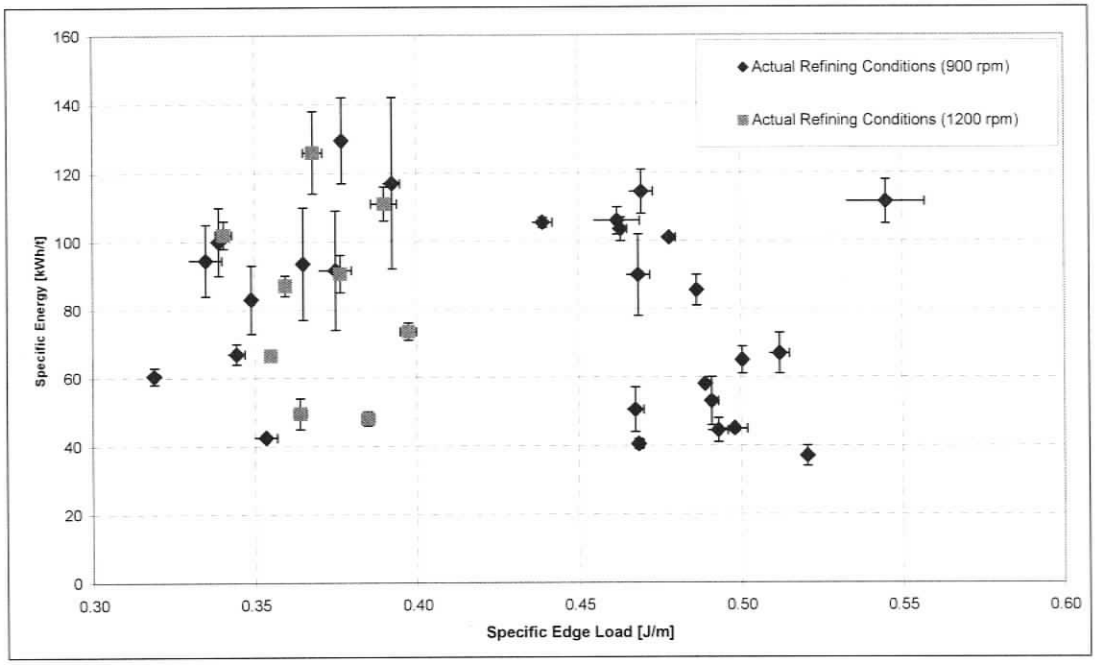

Figure 4-6, Actual refining conditions for comparison with sensor data (Error bars indicate the range in refining conditions for each sample)

4.5 Summary

Fluctuations in the motor load and feed rate caused the actual refining conditions to differ significantly from target levels. Data samples were taken from periods of the experiments with relatively stable specific edge loads. Nine data samples were taken from each experiment. Experiment S9B1 was repeated; the repeated experiment was designated S9B2. 36 data samples were taken in total.

5 DATA PROCESSING

5.1 Introduction

In total, 30 min 25 sec of data was recorded, amounting to 3.65×10^8 data points for both piezoelectric elements. Extracting the bar-passing events from this amount of data requires automated analysis. The methods used for this analysis are described in this chapter.

5.2 A Bar-Passing Event

In Chapter 1, it is explained that the cyclic compression and shearing of fibres makes them flexible and fibrillated for papermaking. This compression is applied to the pulp as it is trapped between the rotor and stator bars crossing over one another. Each of these bar-crossings is referred to as a *bar-passing event*. This is illustrated below in Figure 5-1.

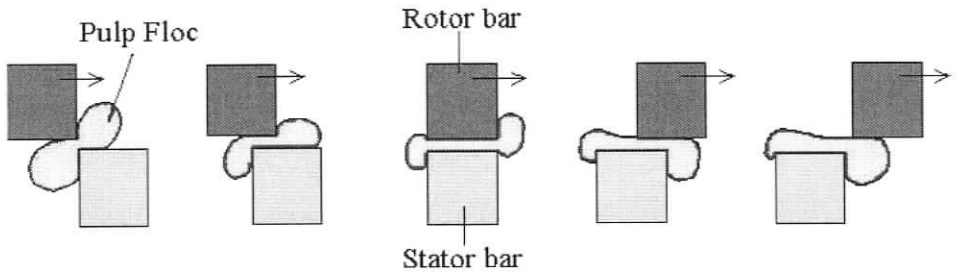

Figure 5-1, A bar-passing event [17]

An example of data recorded by the sensor is shown in Figure 5-2:

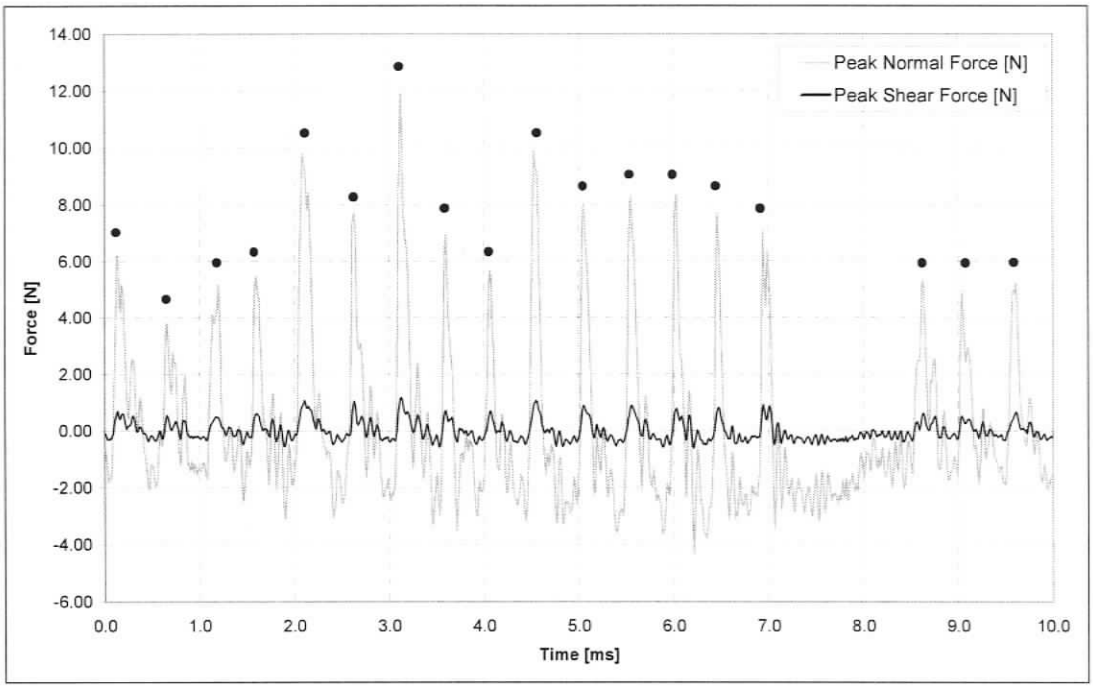

Figure 5-2, Typical sensor data with bar-passing events indicated by dots (Experiment S9B1-5. Time: 9:23:20.000 - 9:23:20.010. [SEL=0.32 J/m])

Each large "spike" in the data (indicated by a dot) represents the forces measured during a bar-passing event. The shape of the event can change depending on a variety of factors including the amount of pulp present during the bar-crossing, the shape of the bar and the loading on the refiner. The smaller oscillations are *resonance* of the sensor occurring after an impact and are indicated in Figure 5-3, which shows a segment of data taken from Figure 5-2. After the 15th bar-passing event in Figure 5-2, seven of these oscillations take place over approximately 0.5 ms, corresponding to a frequency of 14 kHz. This frequency is close to the sensor's lowest natural frequency of 15 kHz.

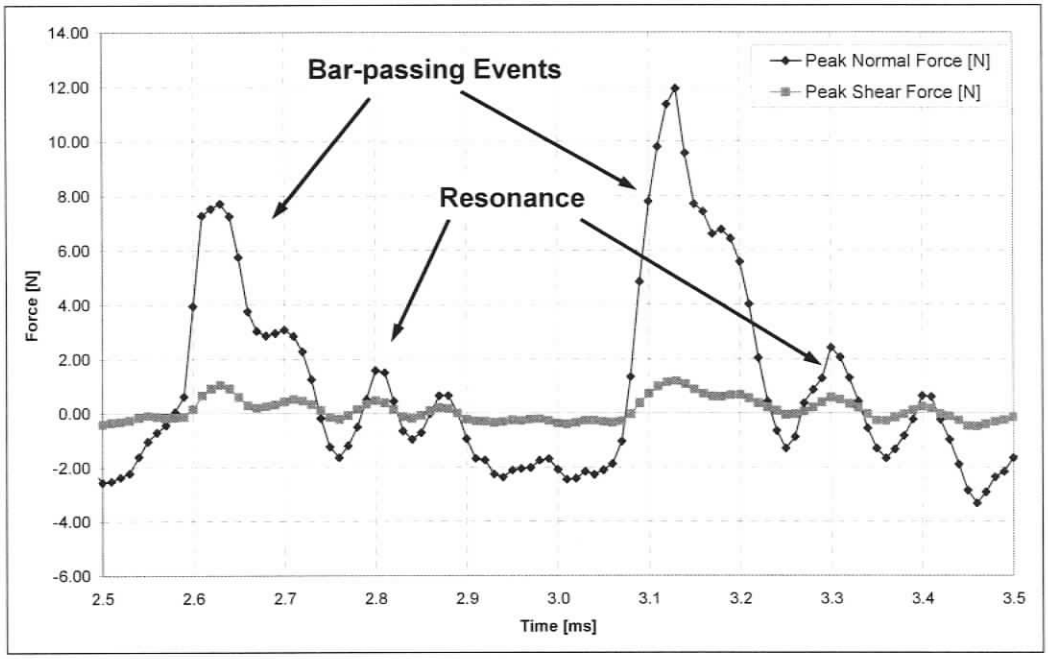

Figure 5-3, Sensor data (Experiment S9B1-5. Time: 9:23:20.0025 - 9:23:20.0035. [SEL=0.32 J/m])

5.3 Event Classification

A primitive way of classifying a typical bar-passing event is *a single peak bound by two valleys*; representing the trapping of a single floc of pulp over one bar-passing. Due to the heterogeneity in feed and load, it is not uncommon for a bar-passing event to take on many different shapes. To identify bar-passing events, an algorithm was created using LabVIEW by Mr. Dustin Olender, with the assistance of the author. This algorithm not only identifies events, but also classifies them based on various criteria. For data to be identified as a bar-passing event, it must pass a series of criteria. For simplicity, these steps have been categorized into *Primary Event Classification Criteria* and *Secondary Event Classification Criteria.* Primary Event Classification involves identification of all potential events. Secondary Event Classification Criteria assesses the attributes of the potential event to either accept or discard it.

5.3.1 Primary Event Classification Criteria

All data acquired is subjected to LabVIEW's built-in peak detection function which scans for local maxima in the normal force data (using a 3-point quadratic interpolation). The classifier then creates an array containing the location or *index* of that peak. This array will be referred to as the *Peak Index* array. In Figure 5-4, peaks would be detected at indices 8, 11 and 14. Peaks that are found outside a set of upper and lower limits – *Upper/Lower Search Limits* in Figure 5-4 are discarded from the Peak Index. The reason a peak might need to be discarded from the peak index is to analyse only forces that are between certain thresholds.

Each peak detected by the algorithm is considered a potential event. The next step is to find the beginning and ending of each potential event. The two criteria for finding these *boundaries* are that they must occur at a minima and must also be below a certain percentage of the peak value, which will be called the *Peak Fraction* (shown in Figure 5-4). Since the three peaks initially detected all have different magnitudes, they also all have different peak fractions.

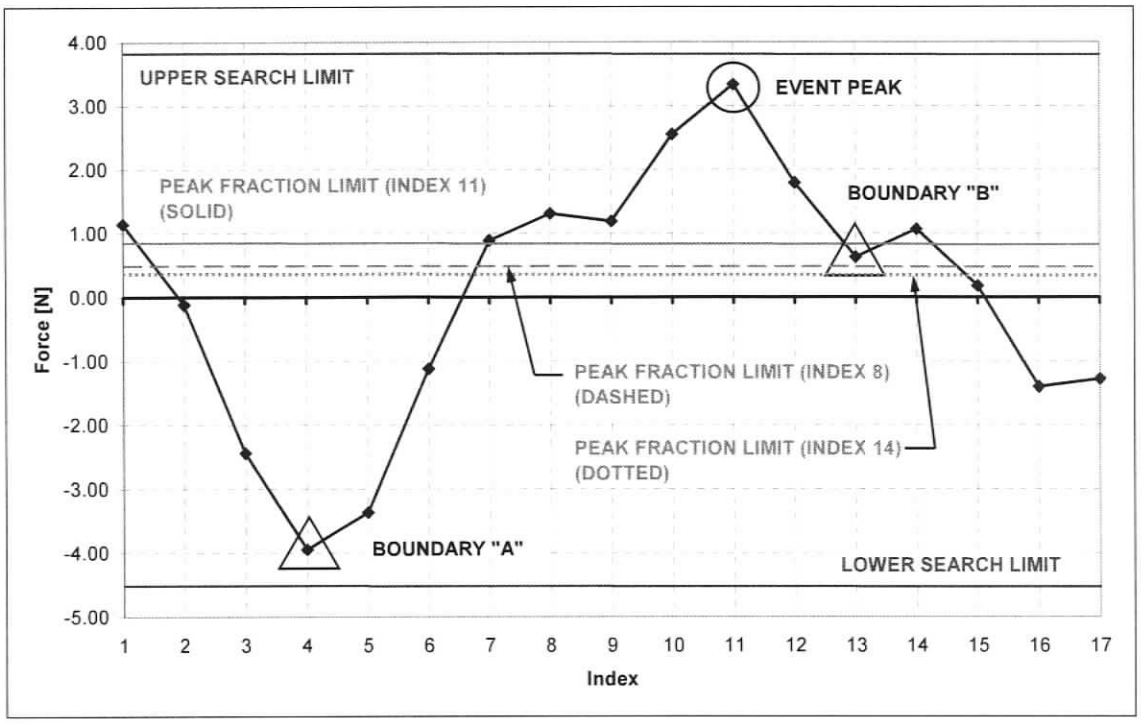

Figure 5-4, A potential bar-passing event

The event classifier first scans the data starting at index 8. The classifier then compares the magnitude of the peak at index 8 to the magnitudes of data points both sides of it, continuing outwards until a suitable boundary is found. If any data point has a higher magnitude than the current peak, the current peak is discarded from the Peak Index. For example, once the data point at index 10 is compared with the peak at index 8, the peak at index 8 is discarded from the Peak Index. The algorithm then moves to the next peak, at index 11, and repeats this procedure (searching for suitable boundaries). Although the data point at index 9 is a local minimum, since this value is above the peak fraction, the program continues searching for a boundary. Finally a boundary is found at index 4. Another boundary is also found at index 13.

The event classifier algorithm proceeds to the next peak in the Peak Index, until all peaks have been analysed. The peak at index 14 would not be considered an event since the local minimum at index 13 would be above a new peak fraction value for the peak at index 14.

5.3.2 Secondary Event Classification Criteria

Once a potential event has been identified, it is tested against two criteria. These two criteria are called the *Event Length Ratio* (ELR) and *Proximity Limit*.

The ELR is calculated as follows:

$$ELR = \frac{\Delta t_{EVENT}}{\Delta t_{BAR}} \qquad (5\text{-}1)$$

Where Δt_{EVENT} is the event period (or "length") in seconds and Δt_{BAR} is the bar-passing period in seconds. If an event is below a prescribed ELR lower limit, it is considered resonance and is removed by discarding the record of its peak value from the Peak Index array.

The Proximity Limit is calculated as follows:

$$PROX = t_{Pi+1} - t_{Pi} \qquad (5\text{-}2)$$

Where t_{Pi} is the occurring time of the i^{th} potential event peak.

If two events are within a prescribed proximity and the second event is smaller in magnitude, the second event is considered resonance following a bar-passing event and is discarded. Figure 5-5 illustrates Event Proximity.

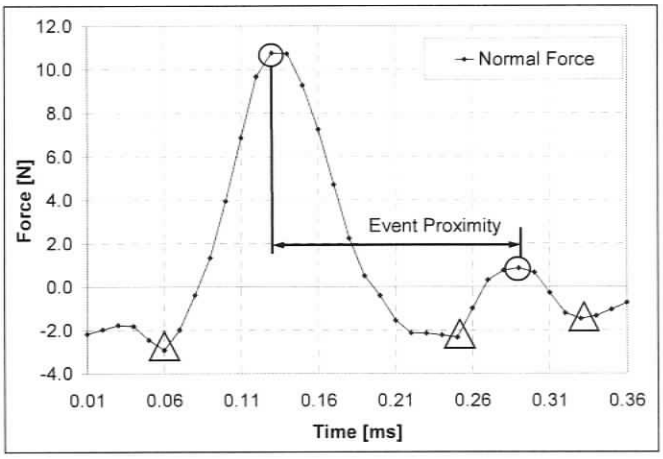

Figure 5-5, An example of Event Proximity

The logic for the event classifier algorithm is detailed in Appendix B. If a set of data passes these two Secondary Classification Criteria then it is considered a bar-passing event and various event *parameters* can be extracted.

5.3.3 Event Parameters

An event parameter is information about the event that quantitatively describes its shape and size, allowing comparisons to be made between bar-passing events at various refining conditions and between changes in pulp properties. The parameters calculated are: *Event Length Ratio*, *Normal and Shear Forces*, *Shear Work*, *Peak Coefficient of Friction* and *Shear Lead*.

5.3.3.1 Normal and Shear Forces

Some events have negative force values over the duration of the event. The piezoelectric elements in the sensor are able to measure impacts on the probe, regardless of their state of charge. Therefore, if an event's initial boundary has a negative force value, then the magnitude of the event is measured from the leading boundary.

5.3.3.2 Shear Work

Shear work is the total work done over the length of the sensor during one bar-passing event. Shear work is calculated by integrating the shear force over the event length. Integration is carried out using the trapezoidal rule. Since the sensor is capable of measuring time and not distance, the distance is calculated by multiplying the velocity of the bars with time. Velocity is calculated by dividing the effective bar spacing (see Figure 2-4) by the bar-passing period and time is calculated as the reciprocal of the sampling rate.

$$w_S = F \cdot dx$$
$$W_S = \int F \cdot dx$$
$$W_S = \int F \cdot v \cdot dt$$
$$W_S = \sum_i F_i \cdot v \cdot \Delta ts \qquad (5\text{-}3)$$

Where:

w_S is the work done per unit length and W_S is the work done over a bar-passing event.
v is the tangential velocity of the rotor at the sensor (= effective bar spacing/bar-passing period)
Δts is the sampling period (=1/sampling rate)

5.3.3.3 Peak Coefficient of Friction

The Peak Coefficient of Friction is calculated by dividing the Peak Shear Force by the Peak Normal Force within an event.

5.3.3.4 Shear Lead

Shear Lead is the time in milliseconds in which the Peak Shear Force leads the Peak Normal Force. Negative numbers indicate the Peak Normal Force is leading the Peak Shear Force.

5.4 Signal Conditioning and Selection of Event Criteria

Sensitivity studies have been carried out to determine the ideal values for Primary and Secondary Event Criteria along with filtering that has been applied to the data to allow for clearer event identification and are discussed in this section.

5.4.1 Upper and Lower Search Limits

As stated earlier, search limits allow for analysis of forces within certain magnitudes. For the purpose of the LC analysis, these limits were set outside of the data to analyse all of the forces present.

5.4.2 Filtering

When left unfiltered, the lower magnitude bar-passing events are sometimes difficult to distinguish from resonance, as shown in Figure 5-6 (a). Applying a filter to the data allows for clearer identification of bar-passing events. A 2^{nd} order Butterworth notch filter was used with corner frequencies of 6 kHz and 20 kHz respectively. The thresholds encompass RFS4-LC's lowest natural frequency of 15 kHz. Various bandwidths around the sensor's natural frequency were investigated. However, the chosen thresholds were the most successful at separating bar-passing events from resonance. Figure 5-6 (b) shows the effect of applying a notch filter to the same segment of data. Filtering the data eliminates most of the resonance.

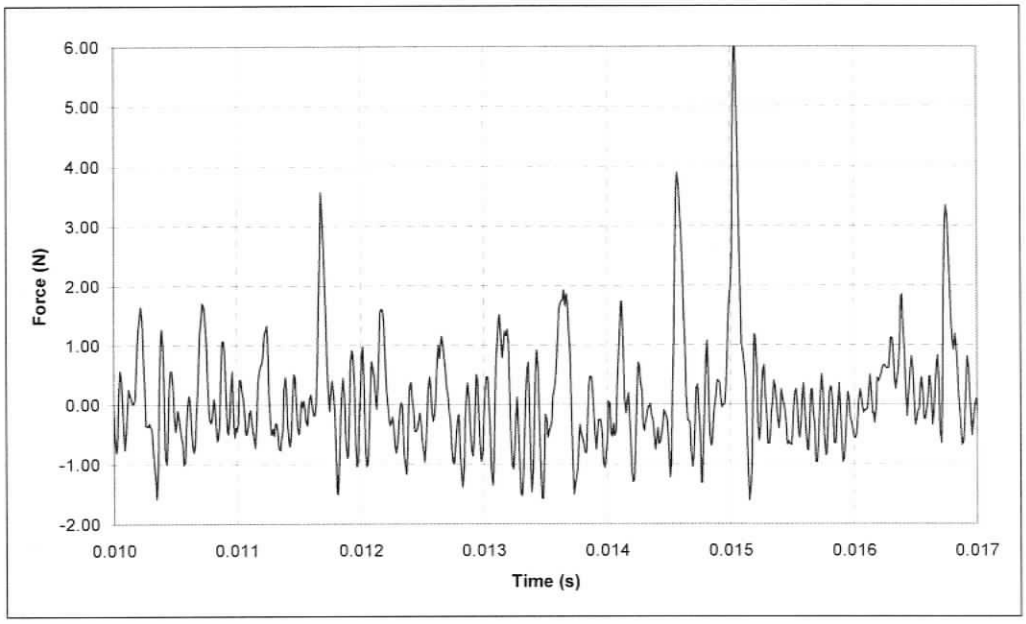

(a)

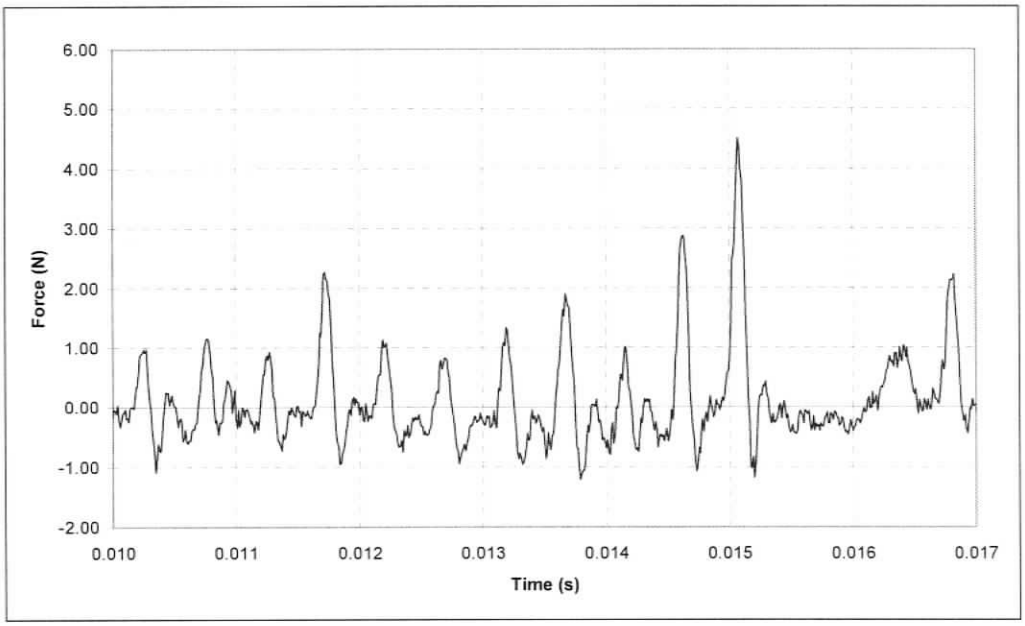

(b)

Figure 5-6, Effect of applying a notch filter to the data – unfiltered data shown above, filtered data below. (Experiment S9-8. Time: 9:08:13.010 - 9:08:13.017. [SEL=0.32 J/m])

Figure 5-7 shows the number of events recorded sorted according to their Event Length Ratio. The distribution is bimodal. The left mode is due principally to resonance. The lowest natural frequency of the sensor is 15 kHz, which has a period of 0.067 ms. The distribution in Figure 5-7 was taken from Experiment S9, where the bar-passing period is 0.5 ms. Therefore, oscillations which have a period of 0.067 ms, have an ELR of 0.13.

Based on inspection of the time domain data, most bar-passing events have an ELR of $0.25 < ELR < 0.50$. Therefore, the right hand mode is due to bar-passing events. This suggests that there may be a minimum ELR below which events are not bar-passing events and can be discarded.

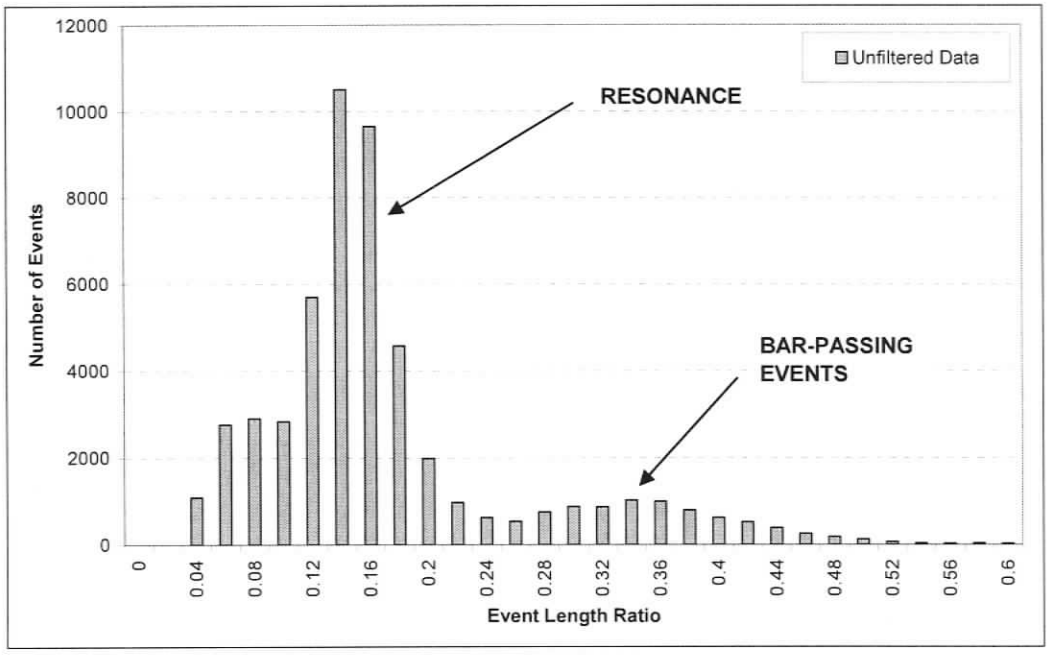

Figure 5-7, The distribution of event lengths on unfiltered data (Experiment S9-8. Time: 9:08:12 - 9:08:17. [SEL=0.32 J/m])

The distribution in Figure 5-7 is also shown in Figure 5-8, but at a different vertical scale to give a better view of the distribution of bar-passing events.

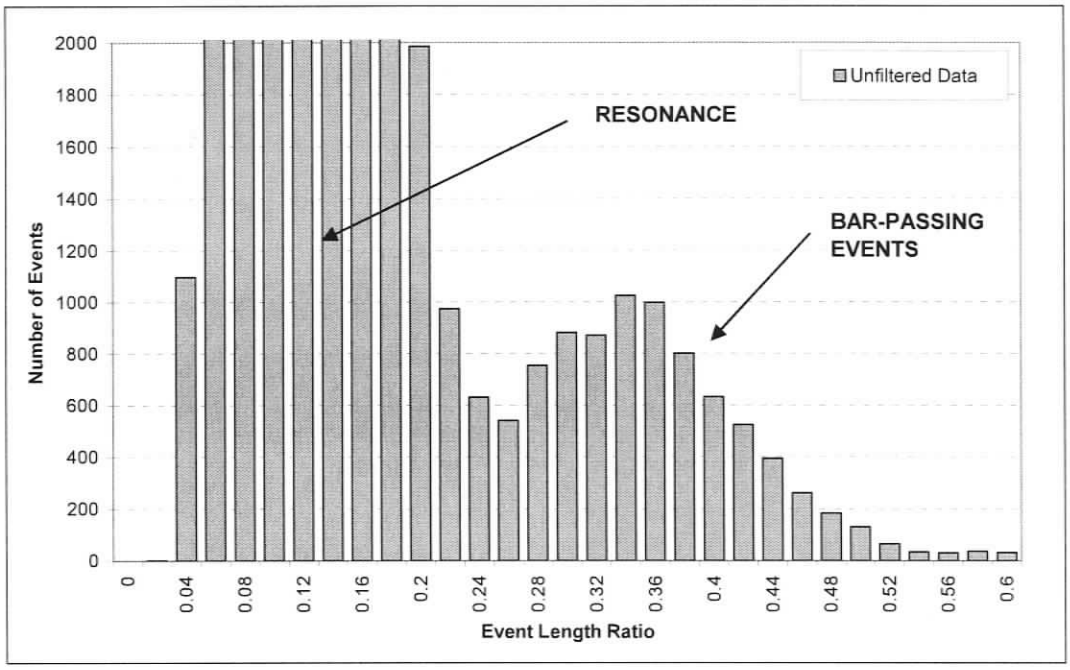

Figure 5-8, The distribution of event lengths on unfiltered data – cropped (Experiment S9-8. Time: 9:08:12 - 9:08:17. [SEL=0.32 J/m])

If the ELR is to be used to distinguish resonant events from bar-passing event, it is not clear where to set the ELR lower limit (see Figure 5-8). If the ELR lower limit is set high, more resonance will be removed but at the cost of losing bar-passing events with smaller magnitudes. By setting the ELR lower limit low, resonant events may be counted as bar-passing events.

Figure 5-9 shows the distribution of event lengths after notch filtering. Filtering removes many events with an ELR between 0.16 and 0.30. However, in this region it is still unclear whether events are bar-passing events or not. Therefore another method of discrimination is needed.

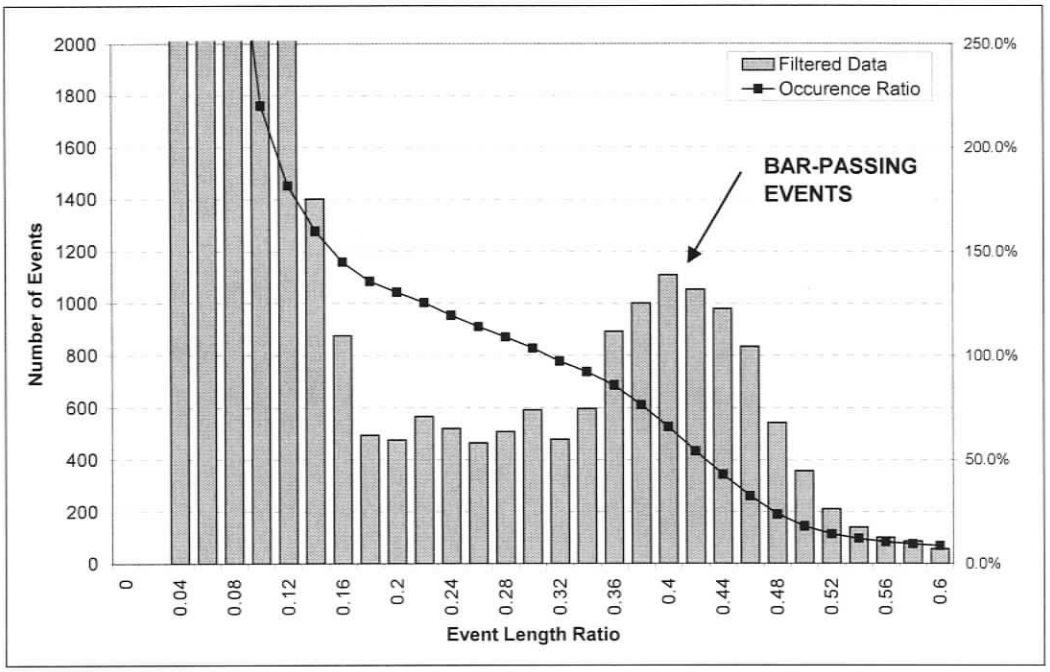

Figure 5-9, The distribution of event lengths on filtered data (Experiment S9-8. Time: 9:08:12 - 9:08:17. [SEL=0.32 J/m])

5.4.3 Proximity Limit and Event Length Ratio

Fundamentally, bar-passing events must occur within a certain temporal proximity of each other (i.e. the bar-passing period). For two events to have a temporal proximity below the bar-passing period, one event must be due to something other than a bar-passing event. Proximities below the bar-passing period can occur in two ways – from resonance following a bar-passing event, or from a bar-passing event following a resonant peak from the *previous* bar-passing event. Figure 5-10 illustrates these two situations.

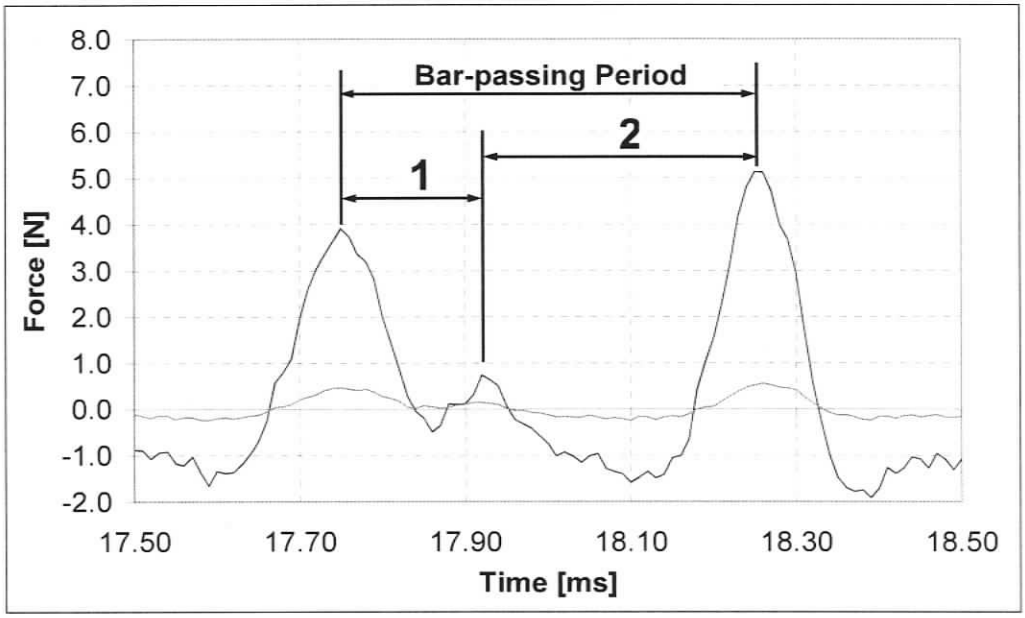

Figure 5-10, Proximity of Events on filtered data (two situations where events can have a proximity below the bar-passing period)

Figure 5-11 shows a normalized distribution of detected events by their temporal proximity to each other. The bar-passing period for this sample of data is 0.5 ms; and an approximately normal distribution around this value is clearly visible. Proximities below 0.4 show two modes: one centred on 0.2 ms and the other on 0.3 ms. These two distributions are comprised of the proximities of resonance preceding and following bar-passing events (shown in Figure 5-10).

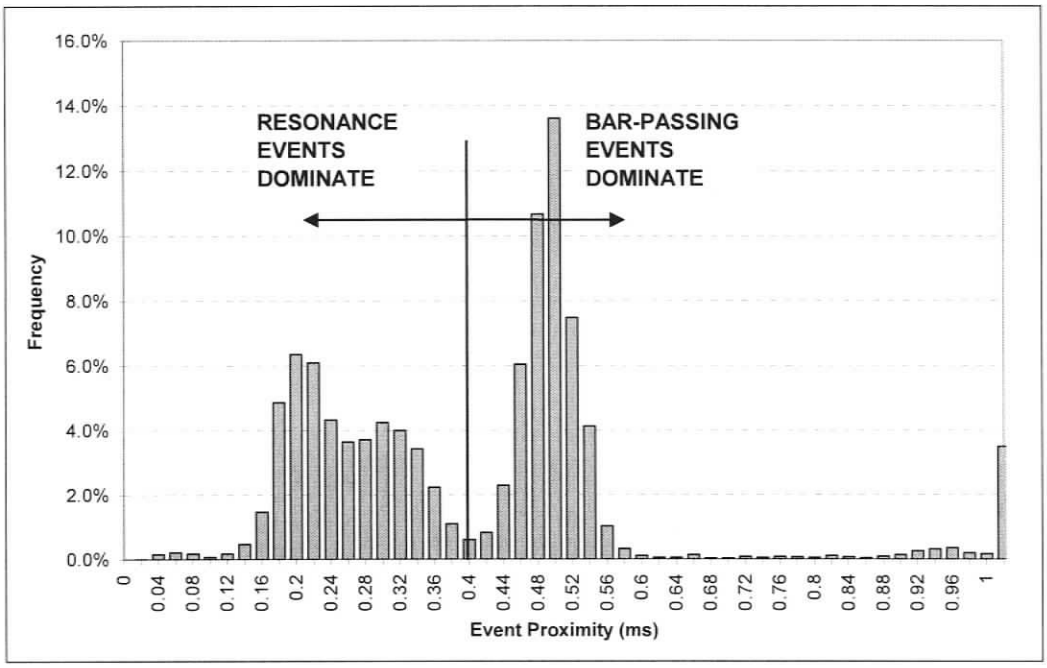

Figure 5-11, Distribution of Event Proximity Using an ELR lower limit of 0.19 (Experiment S9-8. Time: 9:08:12 - 9:08:17. [SEL=0.32 J/m])

Typically, resonance following a bar-passing event is smaller in magnitude than the event itself. Therefore, if two events have a temporal proximity within 0.4 ms and the second event is smaller in magnitude than the first, the second is deleted.

Figure 5-12 shows the ELR distribution of events both with a proximity limit of 0.4 ms applied, and without. A parameter called the *occurrence ratio*[10] is used as a method of determining a suitable ELR. The secondary vertical axis in Figure 5-12 shows a cumulative occurrence ratio. The number of events detected by the Classifier is counted starting from the largest events and ending at the smallest events. One can see in Figure 5-12 that with the proximity limit applied to the data that the cumulative occurrence ratio equals one at events that have an ELR between $0.16 < ELR < 0.18$. The cumulative occurrence ratio flattens over the region between resonant events dominate and bar-passing events dominate. Therefore, the margin of error in selecting a suitable ELR is minimal.

[10] The *occurrence ratio* is the number of events detected compared to the total bar-crossings. An occurrence ratio of one would mean that for every bar-crossing, the event classifier would detect a bar-passing event.

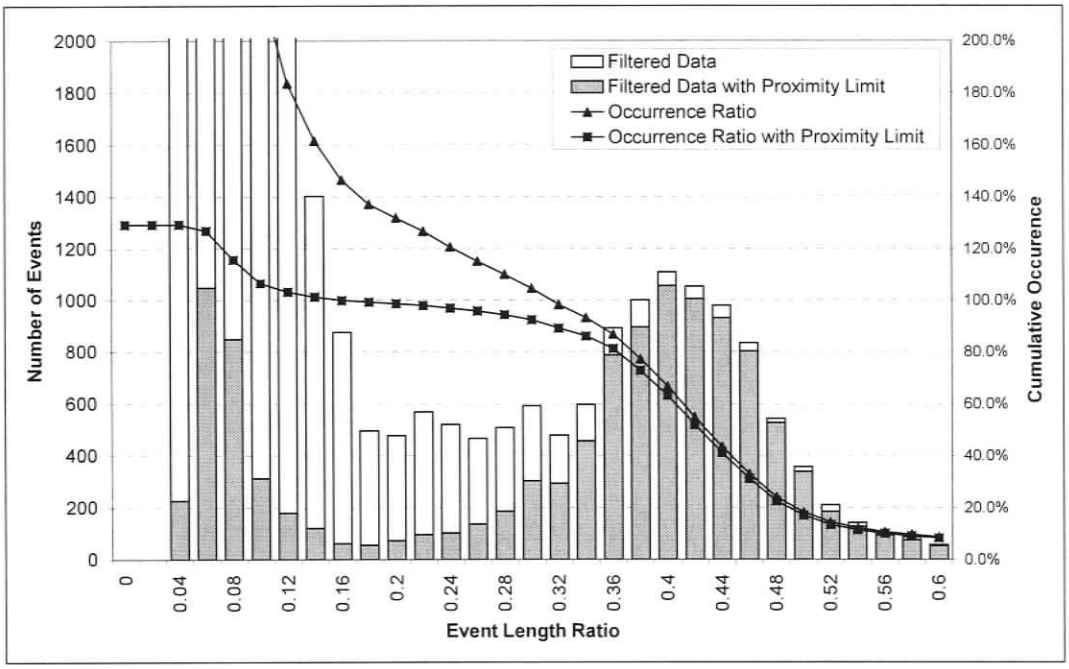

Figure 5-12, Effect of Proximity Limit on Event Length Ratios (Experiment S9-8. Time: 9:08:12 - 9:08:17. [SEL=0.32 J/m])

It is noted that the proximity limit is not very effective when used alone or without filtered data. This is because there are *many* resonance peaks present in the unfiltered data, specifically, many large resonance peaks following smaller resonance peaks. Combining both the proximity limit and the ELR lower limit to filtered data is effective for event classification and a smaller ELR value of 0.17 is used.

5.4.4 Peak Fraction

As stated earlier in Section 5.3.1, the Peak Fraction is a lower force limit, which is used to determine where to bound a force event. Indirectly, the "height" of this parameter controls the length of an event. If the Peak Fraction is set too high, much of the event will not be included, affecting the Shear Work that is calculated. If the Peak Fraction is set too low, multiple events can be improperly perceived as one event. Figure 5-4 illustrates the problem of setting the Peak Fraction too high, with the latter part of that event not being included.

Ideally, the Peak Fraction should be set as low as possible without concatenating multiple events. A sensitivity study was completed on the LC data to observe the effect of changing the Peak Fraction. Four Peak Fraction values were compared – 30%, 10%, 5% and 1%.

When counting the number of events detected by the Event Classifier, as the Peak Fraction is increased, the number of events detected decreases but so does the number of events with an ELR greater than one. Since the consistency of the pulp furnish during these trials is low (3.15%), events do not span more than one bar-crossing. Table 5-1 compares the event count with varying Peak Fraction. Based on this study, a Peak Fraction of 5% was used, since it reduces the number of events with an ELR greater than one, while still detecting many events.

Table 5-1, Event Count using Multiple Peak Fraction Values (Experiment S9-8. Time: 9:08:12 - 9:08:17. [SEL=0.32 J/m]. Bar #1 Events Removed)

Peak Fraction	*Event Count*	*ELR >1*	*Occurrence Ratio*
1%	8600	59	96.3%
5%	8598	21	96.3%
10%	8583	4	96.2%
30%	8466	0	94.9%

Events at Bar #1 have been removed from the data because the sensor crosses at the end of this rotor bar instead of crossing mid-span. It is suspected that only part of the sensor tip passes over this bar. See Figure 5-13 for an illustration of the sensor's path along a rotor segment. An example of a typical event at bar #1 on each segment is shown in Figure 5-14.

Figure 5-13, path of the sensor along a moving plate segment

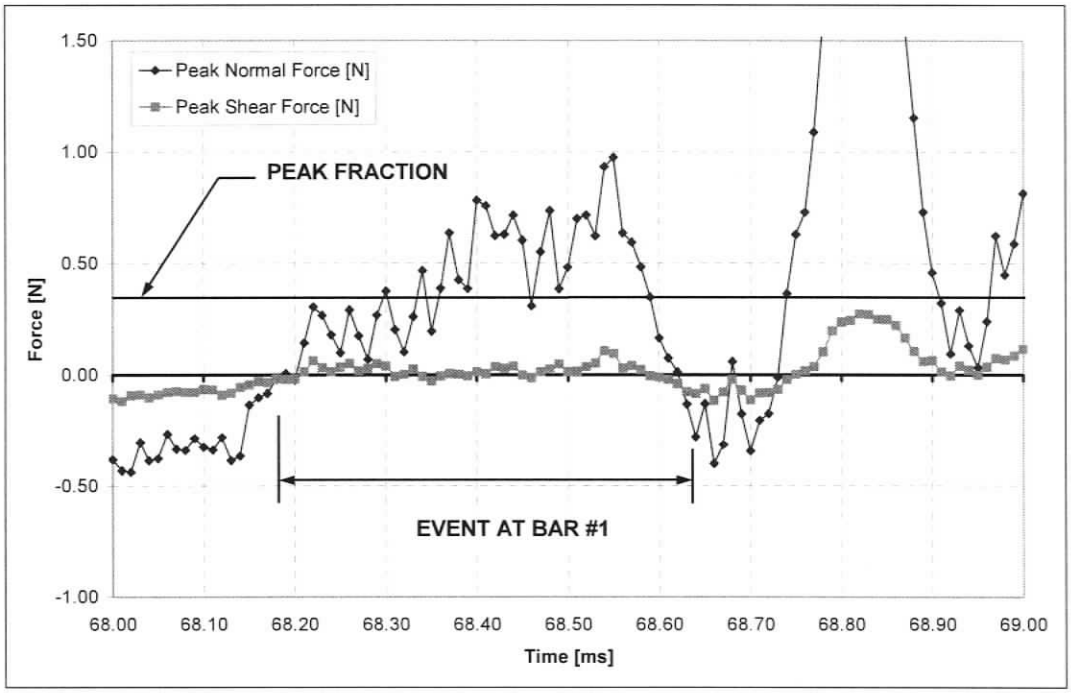

Figure 5-14, Profile of a typical event on the first bar of a plate segment on the rotor (2nd order Butterworth notch filter)

Slight changes in the Peak Fraction will greatly affect the number of events detected at Bar #1. Therefore, data for this bar is removed from this sensitivity study. Irregularities in the events from this bar are quite prevalent and events at Bar #1 are not representative of an impact along the mid-span of a bar. Data for this bar is, therefore removed from the data during data processing, after bar identification.

5.5 Rotor Bar Identification

The rotor is comprised of seven segments, each containing multiple bars. At the sensor's location, 18 bars per segment pass over the stator, is shown in Figure 5-13. Once bar-passing events have been successfully identified, an algorithm developed by the author labels each bar according to its position on the rotor. Since the refiner speed and bar spacing remained constant throughout the trials, the bar-passing period also remained constant, making it possible to predict when, within certain bounds, the next bar-passing event would occur.

The initial step of the *Bar Labelling* algorithm is to identify the bars manually for one plate segment appearing in the data. Once this is done the bar labelling program searches for the same bar on the next segment (shown in Figure 5-15 as Step "1"). The spacing between bars with the same number, on adjacent segments, is within a certain temporal proximity, which will be referred to as the *segment-passing period.* At 900 rpm, this period is 9.57 ms. The program labels bars separated by the segment-passing period as it scans through the data in a forward pass.

Once one forward pass is completed, any bars that have not yet been labelled using their segment-passing period are then identified based on their bar-passing period. Steps "2" and "3" in Figure 5-15 involve searching for bar-passing events that have a temporal proximity equal to the bar-passing period. Step "2" scans forward through the data searching for events with a temporal proximity of a bar-passing period, while Step "3" repeats this process in the reverse direction. Flow charts illustrating this algorithm are included in Appendix B.

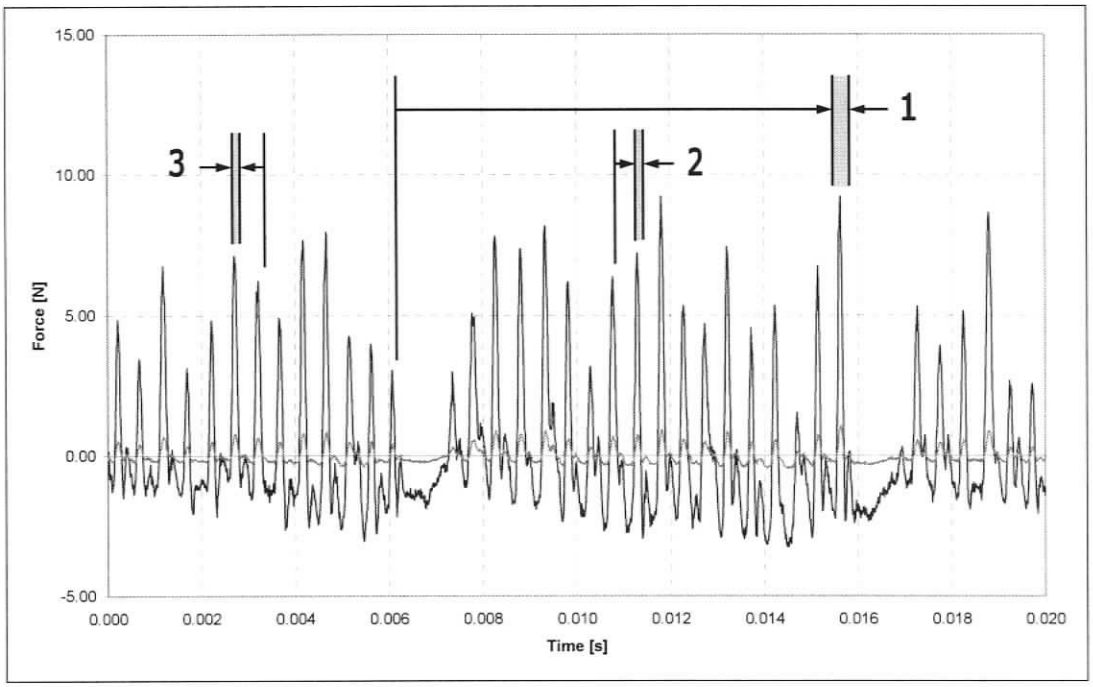

Figure 5-15, Bar Labelling Procedure

Once the bars have been successfully identified according to their position on the rotor, the segments and revolutions in which the events have occurred are added, making it possible to sort the data based on segment and individual bars. This is advantageous for exploring trends at these levels from misalignment in the rotor (*Out of Tram*) to differences in the individual bars (bars worn at different rates). The logic for these sub-routines is also shown in Appendix B.

5.6 Raw Data Extraction

Although applying a notch filter to the data is necessary for event detection and bar labelling, the filter removes certain frequency components from the event, which affects its shape. Filtering causes the magnitudes of the force peaks to be smaller than the unfiltered magnitudes. Unfiltered data is preferred for extracting the event parameters (such as shear work, shear lead and coefficient of friction). A method of extracting the same bar-passing events (that have been identified and labelled) in the filtered data from the unfiltered data is needed. To extract bar-passing events from unfiltered data, the Event Classifier is used to

detect all events in the unfiltered data without applying either an ELR lower limit or a Proximity Limit. This ensures that all bar-passing events are identified in the unfiltered data. It also means that all non bar-passing events are also included. Events from the unfiltered data set are then compared to events from the filtered data set, which have been labelled and identified. Any event from the unfiltered data set that does not have a peak occurring within 0.1 ms from the peak of an identified, labelled event is deleted. A tolerance of 0.1 ms between the peaks in the filtered and unfiltered events is needed because filtering introduces a phase lag in the data. This lag is consistently equal to 0.04 ± 0.01 ms.

5.7 Manual Verification

To ensure that both the Event Classification and Bar Identification algorithms successfully identify only bar-passing events along with the correct rotor bar, the samples from each experiment with the lowest occurrence ratios were manually verified. Samples with the lowest occurrence ratio from each experiment were selected for manual verification because they present the worst case scenarios for event detection. For example, if a sample has an occurrence ratio of 0.88 then 12% of the total bar-crossings were either without events or the events were not detected by the algorithms used.

A 0.1 s segment of data within each sample was analysed. The results are summarized in Table 5-2. The number of bar-passing events in the fourth column of Table 5-2 represent the number of events detected when manually scanning through the data. The number of events detected represent the number of events detected using the Event Classification and Bar Identification algorithms. A resonant event is counted if it is detected in place of a bar-passing event.

Table 5-2, Manual Verification of Event Classification

Sample	Analysis Start Time	Analysis Finish Time	No. of Bar-passing Events	No. of Events Detected	Resonance Detected	Accuracy
S9-3	9:07:03.000	9:07:03.100	177	170	2	95%
S9B1-1	9:22:53.000	9:22:53.100	177	176	1	99%
S9B2-3	11:17:24.500	11:17:24.600	173	170	0	98%
S12-4	11:02:38.000	11:02:38.100	204	191	0	94%

5.8 Summary

A method of identifying bar-passing events from the sensor data, extracting various event parameters, and identifying the bar on the rotor in which each event occurred was successful. Manual verification of the Event Classification and Rotor Bar Identification algorithms was carried out. Both algorithms are successful at identifying events and bar locations.

6 Results and Discussion I – Force Profiles and Event Parameter Distributions

6.1 Introduction

In this chapter, data recorded during the refiner trials at the Pulp and Paper Research Institute of Canada in Vancouver, BC. is presented. Force profiles are examined along with the distributions of the event parameters.

6.2 Force Profiles

Before exploring trends in the forces observed under the various refining conditions, there is a need for some familiarity with the bar-passing events. The Figure 6-1 shows 90 ms of force data recorded in the refiner. One revolution of the rotor at a speed of 900 rpm is completed in 67 ms. The first noticeable feature in the plot is that there are groups of 18 bar-passing events. Each spike represents a bar-passing event and each group of spikes corresponds to a plate segment on the rotor. The number above each segment represents its position on the rotor. Note the similarities between the forces recorded over the same segments, but on different revolutions (i.e. segment #4 and #5).

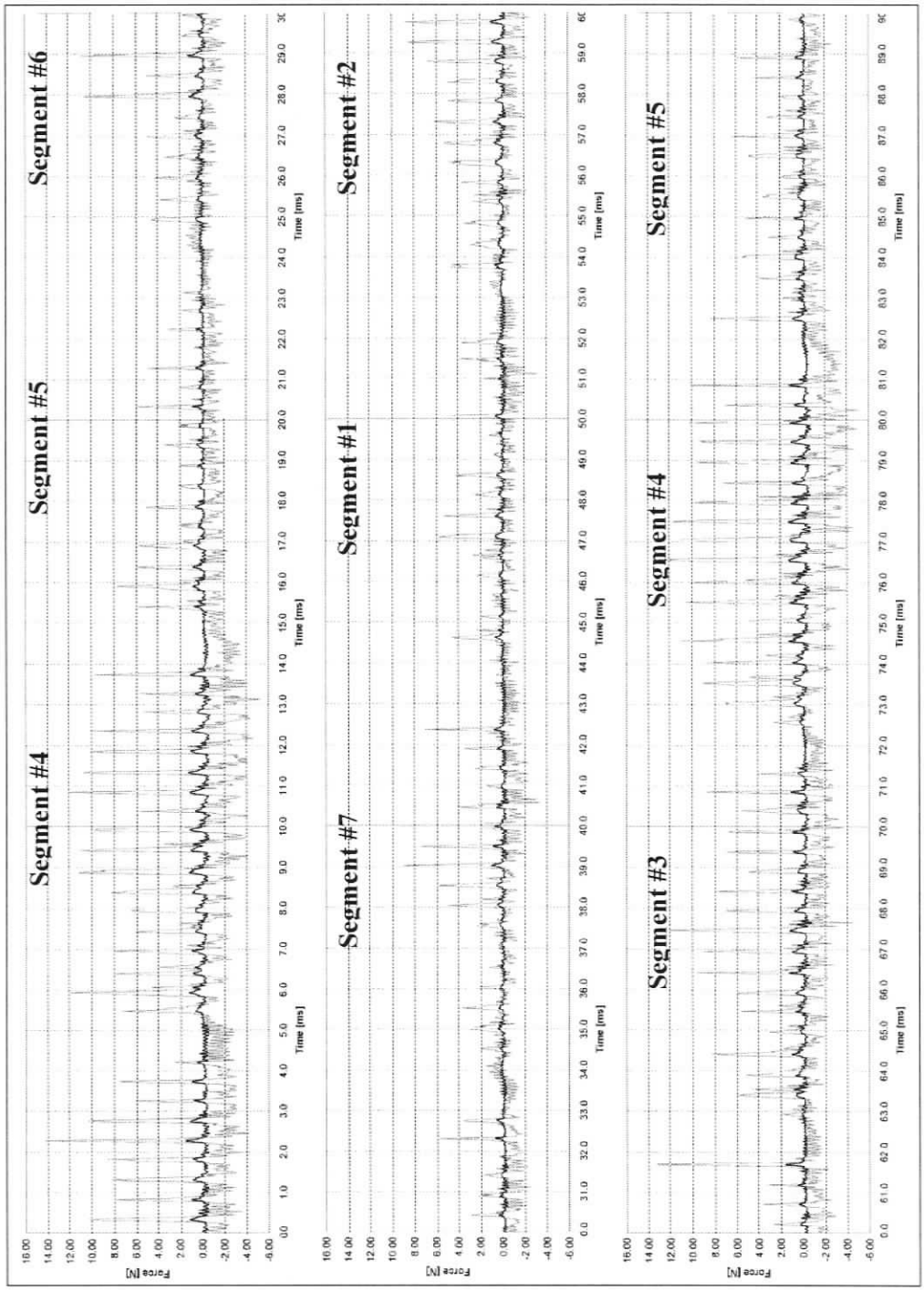

Figure 6-1, Unfiltered Normal and Shear Forces measured in the Conflo® JC-00 refiner. Normal forces are grey, shear forces are black. (90 ms of data shown from experiment S9B1-5. Time: 9:23:21.000- 9:23:21.090. [SEL=0.47 J/m])

The power spectrum for this data shows peaks at the bar-passing frequency, the segment-passing frequency and the rotor frequency Figure 6-2. A bar-passing frequency of 2.0 kHz (at 900 rpm), corresponds to a period of 0.5 ms. This agrees with the time between impacts shown in Figure 6-1. The segments cycle at a frequency of 104 Hz which equates to a period of 9.6 ms. Finally, the rotor frequency at 900 rpm is 15 Hz. The origin of the peak at 4 kHz is unknown.

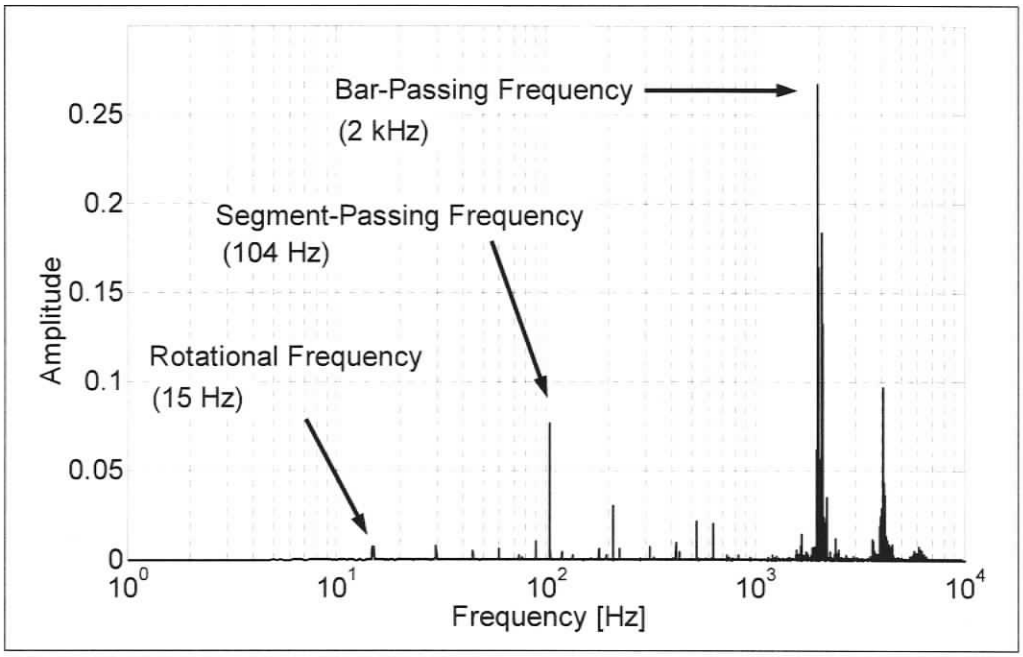

Figure 6-2, Power spectrum of data recorded at a refiner speed of 900 rpm (Experiment S9B1-5. Time: 9:23:20 - 9:23:21 [SEL=0.47 J/m])

Figure 6-3 and Figure 6-4 show the normal and shear forces, respectively, for a small time period to give a clearer view of the profile of typical bar-passing events. At a refiner speed of 900 rpm an event is typically ~0.2 ms in duration compared to the bar-passing period of 0.5 ms. Although their profiles are similar, the shear force magnitudes are typically 10-20% of the normal force magnitudes. It is also important to note the resonant vibrations following the main bar-passing events, as discussed in Chapter 5.

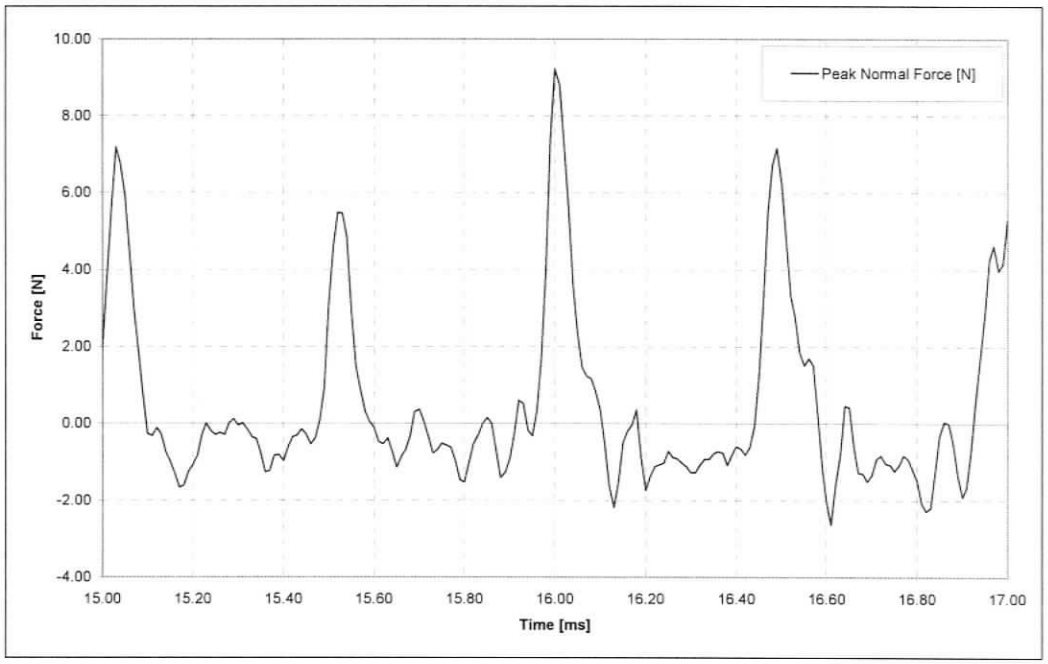

Figure 6-3, Typical Unfiltered Normal Force Profiles (Experiment S9B1-1. Time: 9:22:52.015 - 9:22:52.017. [SEL=0.47 J/m])

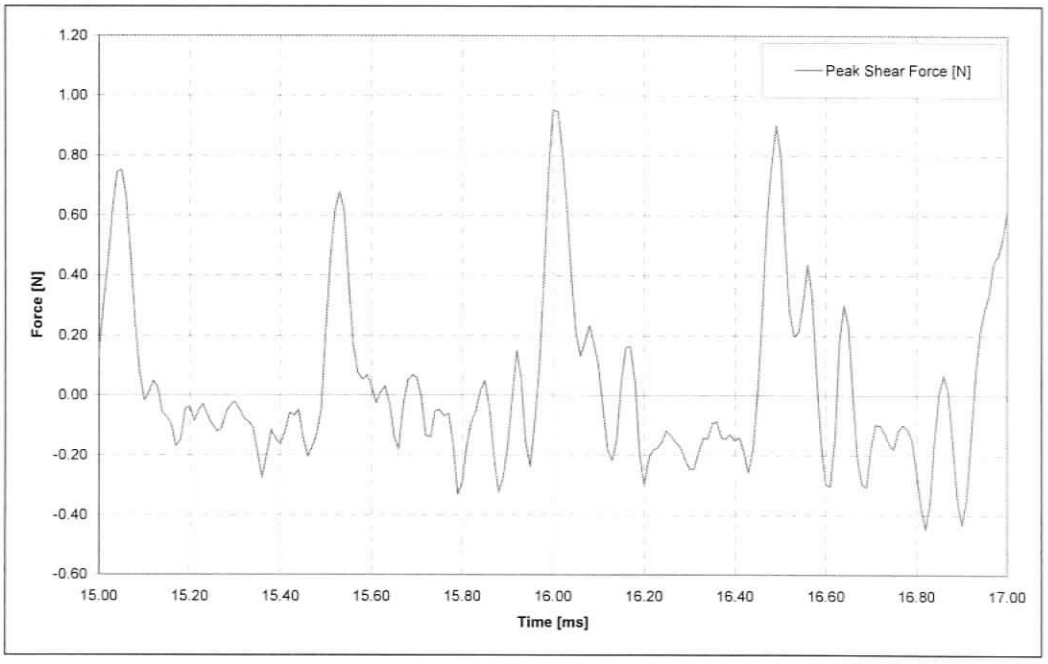

Figure 6-4, Typical Unfiltered Shear Force Profiles (Experiment S9B1-1. Time: 9:22:52.015 - 9:22:52.017. [SEL=0.47 J/m])

6.3 Plate Segment Identification

Once the bar-passing events have been classified and labelled according to their position within a plate segment, the segment numbers are added along with the revolution in which the bar-passing event occurred. To correctly identify the bar-passing events with their proper plate segment, a bar count was completed for each plate segment. This is shown in Figure 6-5, which shows the distribution of bar-passing events according to their respective bar number on the rotor. One can see that there is a distinct difference between the number of bar-passing events at bars #12, 13, 15, and 16 on segment #1 when compared to all other segments. This "characteristic signature" of segment #1 is present in every data sample and is used as a point of reference in processing segment level data.

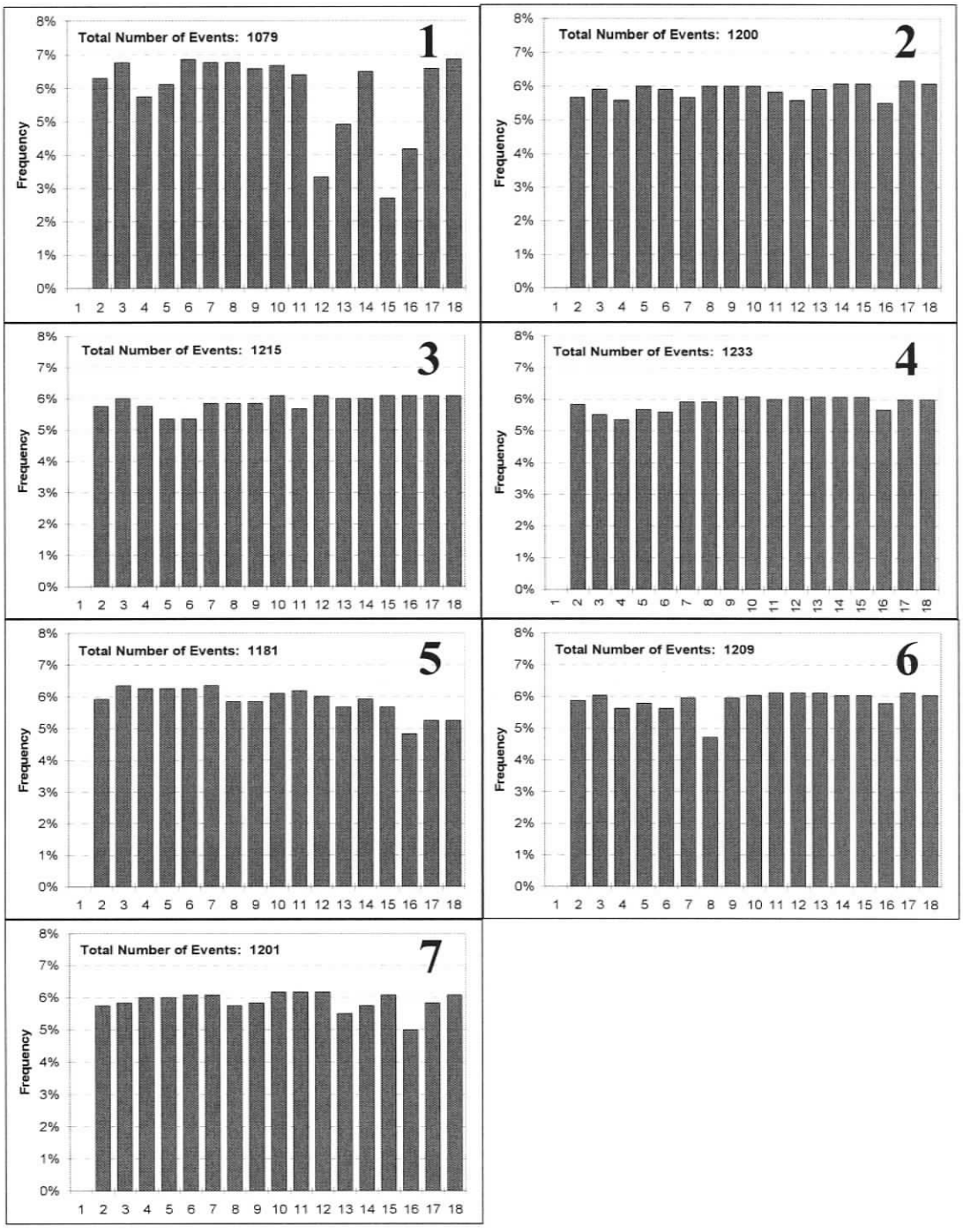

Figure 6-5, Typical bar counts at each plate segment on the rotor. The horizontal axis identifies the rotor bar number (Experiment S9-1. Time: 9:06:00-9:06:05. [SEL=0.38 J/m])

6.4 Occurrence Ratio

The ratio of detected bar-passing events to the total bar crossings is defined as the *occurrence ratio*. This parameter was first introduced in Chapter 5 as a method of validating the *Event Classifier's* input parameters to ensure that the maximum number of events are recorded. Table 6-1 shows the occurrence ratios for each sample.

Table 6-1, Occurrence Ratio of Events during Refining

Experiment	Sample 1	2	3	4	5	6	7	8	9
S12	0.93	0.94	0.95	0.91	0.95	0.96	0.97	0.94	0.97
S9	0.93	0.95	0.88	0.96	0.96	0.96	0.96	0.96	0.91
S9B1	0.95	0.96	0.96	0.96	0.96	0.95	0.97	0.97	0.97
S9B2	0.98	0.98	0.97	0.97	0.97	0.98	0.97	0.97	0.97

Although the occurrence ratio is a measure of the Classifier's ability to identify bar-passing events, an occurrence ratio of 0.98 does not necessarily mean that two percent of the total bar-passing events were not recorded. As shown in Figure 6-1 there are instances of bar-crossings without events and it is believed that this is due to the absence of pulp between the refiner bars. Manual verification of the data shows the accuracy of event detection is greater than the occurrence ratios recorded for the samples. Therefore, the actual percentage of pulp present between the refiner bars at each data sample is greater than the occurrence ratio for that sample.

6.5 Event Parameter Distributions

Since each bar-passing event is unique, a useful way of summarizing the data is with distributions of key event parameters as discussed in Section 5.3.3. Figure 6-6 and Figure 6-7 show typical distributions for normal and shear forces, respectively. A Weibull distribution has been fit to this data with the parameters β, η and R^2. These parameters will be discussed later in this chapter. For this particular sample, the normal and shear force medians are 4.68 N and 0.66 N, respectively. The distributions shown are taken from 15 671 recorded events. Weibull parameters from all samples are included in Appendix C.

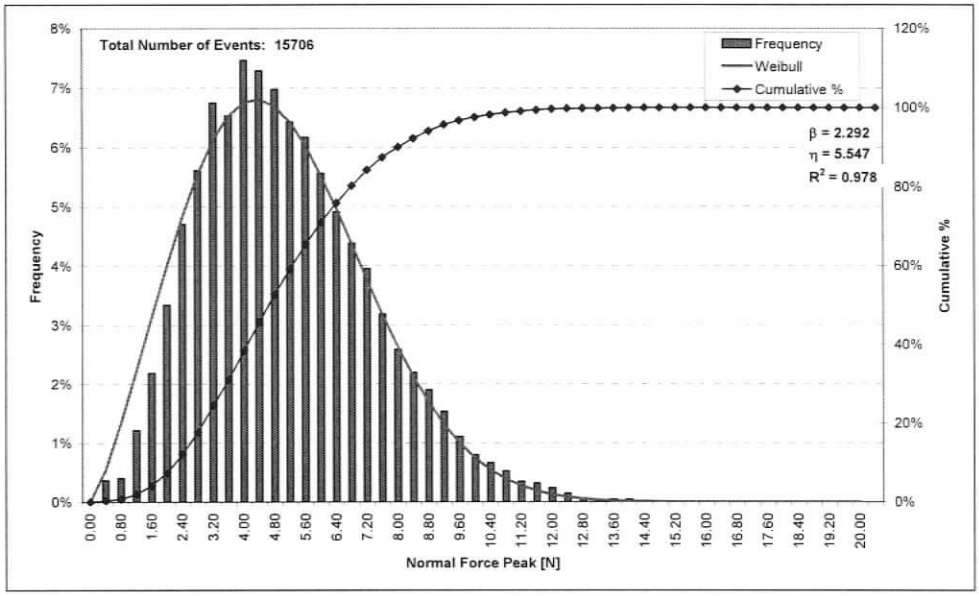

Figure 6-6, Normalized distribution of Normal Force Peaks [N] (Experiment S9B2-6. Time: 11:18:07-11:18:16. [SEL=0.47 J/m])

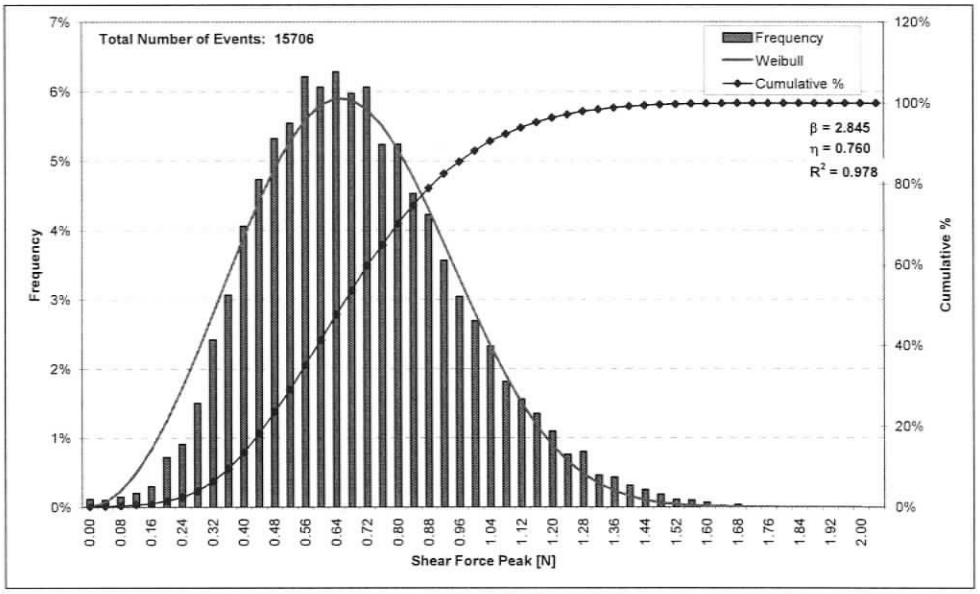

Figure 6-7, Normalized distribution of Shear Force Peaks [N] (Experiment S9B2-6. Time: 11:18:07-11:18:16. [SEL=0.47 J/m])

The corresponding distribution of the coefficient of friction is shown in Figure 6-8. The coefficient of friction is calculated as the ratio of the peak shear force to the peak normal force. The median coefficient of friction for this sample is 0.14. This value is close to that obtained by Goncharov et al. [6] who measured a coefficient of friction of 0.11 in medium hardness, unbleached sulphite pulp with a stock consistency of 2.5-3%.

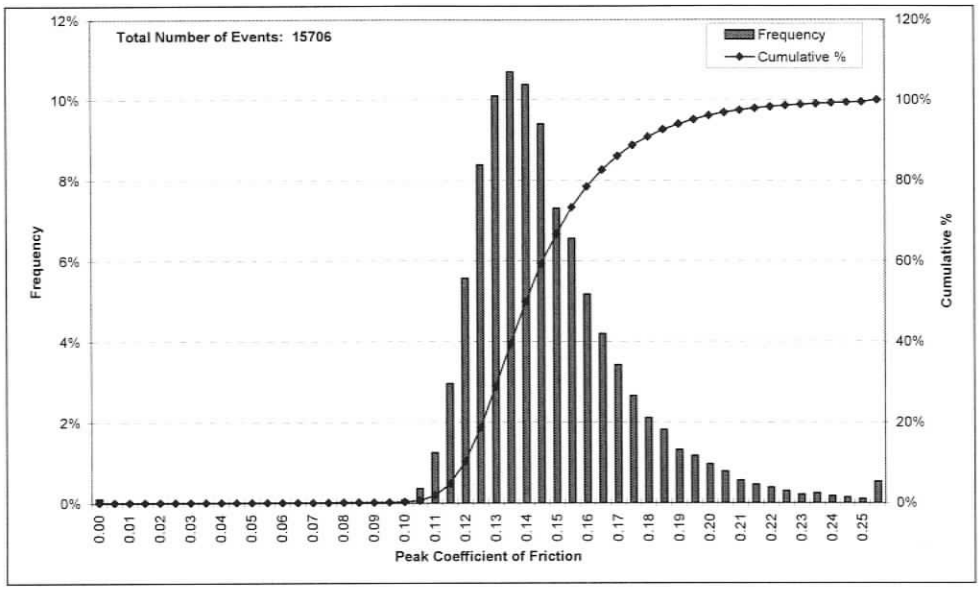

Figure 6-8, Normalized distribution of Coefficients of Friction (Experiment S9B2-6. Time: 11:18:07-11:18:16. [SEL=0.47 J/m])

The shear work recorded for this sample is similar in shape to the shear force distribution Figure 6-9. This suggests that the events recorded have a similar profile and that the work done is closely related to the magnitude of the shear force.

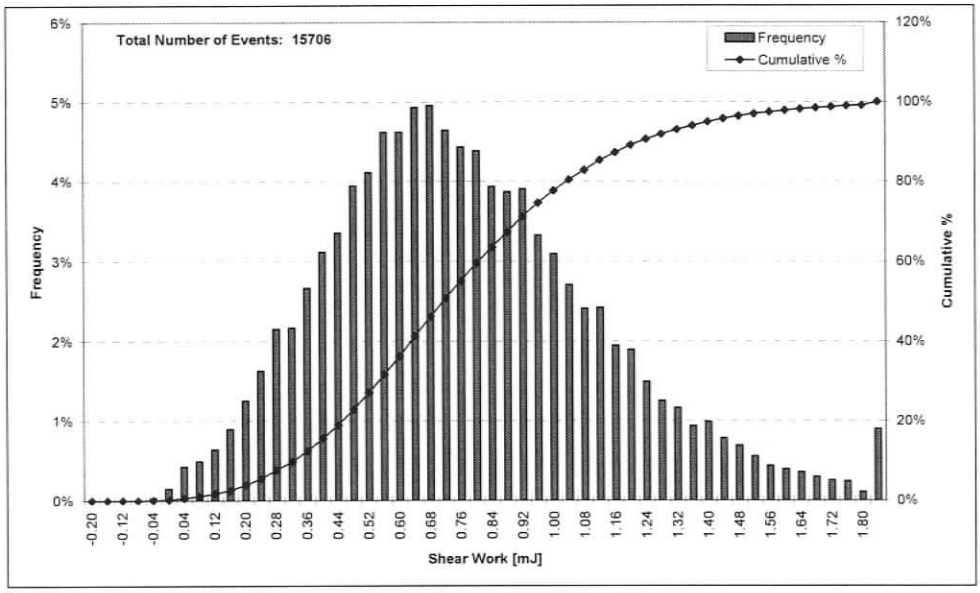

Figure 6-9, Normalized distribution of Shear Work [mJ] (Experiment S9B2-6. Time: 11:18:07-11:18:16. [SEL=0.47 J/m])

Finally, the shear lead distribution was studied, as shown in Figure 6-10. The mean shear lead is -0.005 ms, corresponding to a lead of 2.5% of the event length.

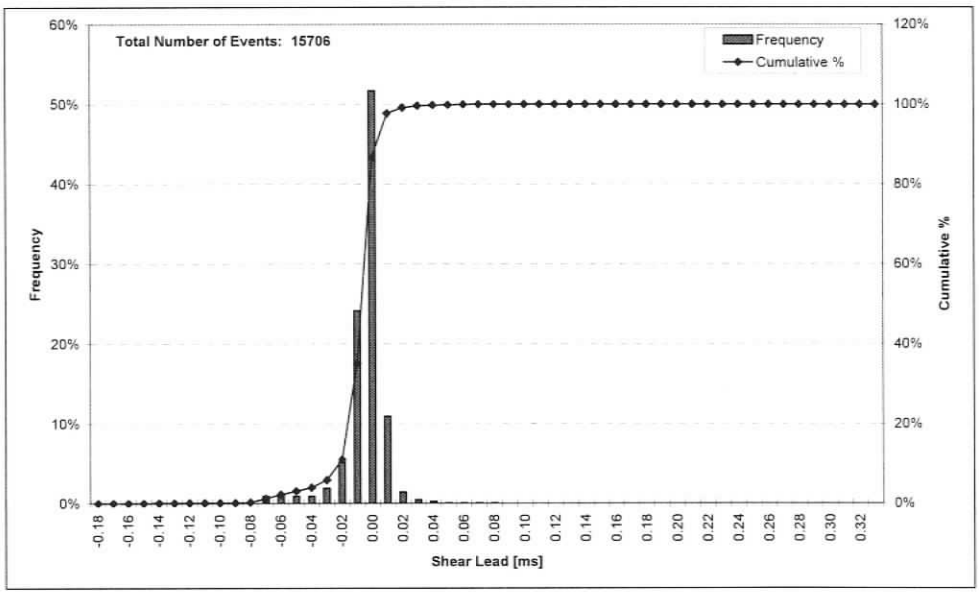

Figure 6-10, Normalized distribution of Shear Lead [ms] (Experiment S9B2-6. Time: 11:18:07-11:18:16. [SEL=0.47 J/m])

6.6 The Weibull Distribution

As discussed earlier in the chapter, a two-parameter Weibull function was used to characterize the force distributions. The two parameters are a shape parameter, β, and a scaling parameter, η. The Weibull function is commonly used since it allows for analysis of distributions that have multiple shapes [21]. A third parameter for the Weibull exists, symbolized by γ, which is used for translation along the abscissa.

The Weibull function is useful in that it allows for key information to be gathered about the distribution using only the function parameters and the total number of events. The tables in Appendix C show the Weibull parameters for all experiments.

The Weibull probability distribution function is represented as:

$$f(x)=\frac{\beta}{\eta}\left(\frac{x-\gamma}{\eta}\right)^{\beta-1}\cdot e^{-\left(\frac{x-\gamma}{\eta}\right)^{\beta}} \quad (6\text{-}1)$$

The Weibull cumulative distribution function is represented as:

$$f(x)=1-e^{-\left(\frac{x-\gamma}{\eta}\right)^{\beta}} \quad (6\text{-}2)$$

The median value of a two-parameter Weibull probability distribution can be calculated by rearranging the two-parameter cumulative distribution function and setting f(x) to 0.5. This is shown below:

$$x=\eta\left(-\ln(0.5)\right)^{\left(\frac{1}{\beta}\right)} \quad (6\text{-}3)$$

6.6.1 Effect of Varying the Weibull Parameters

Figure 6-11, Figure 6-12 and Figure 6-13 show the effects of how changing each parameter have to the shape, size and location of a Weibull distribution.

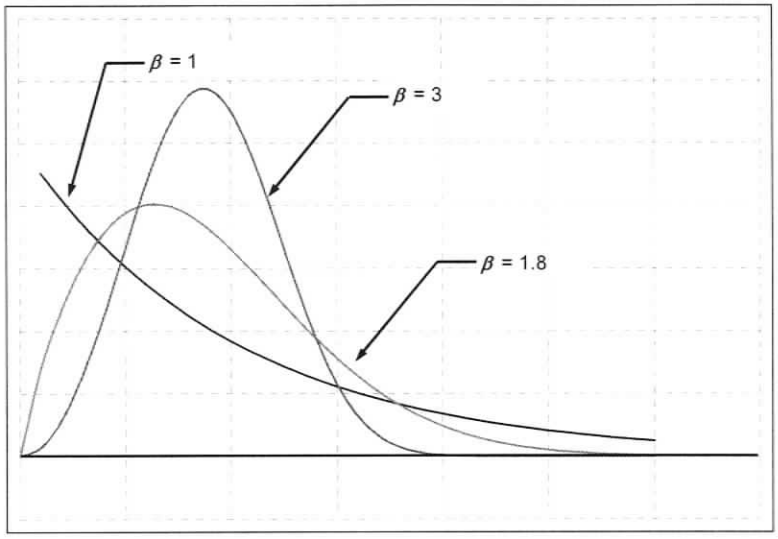

Figure 6-11, The effect of varying β in a Weibull Distribution

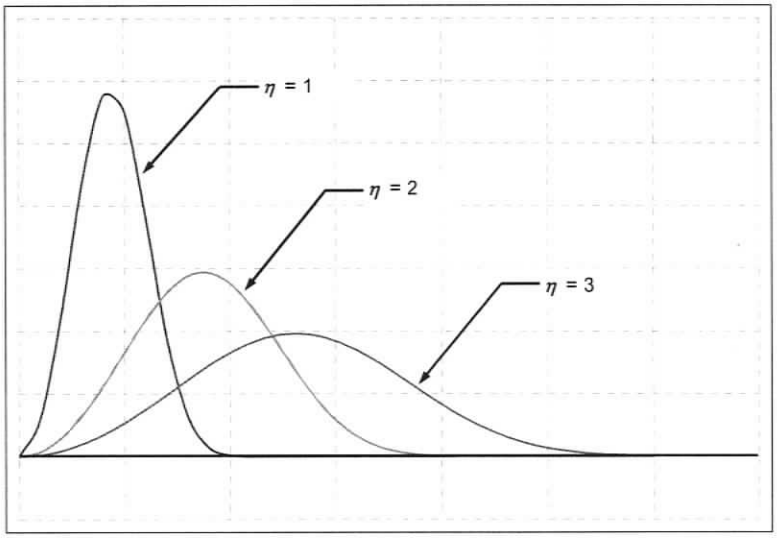

Figure 6-12, The effect of varying η in a Weibull Distribution

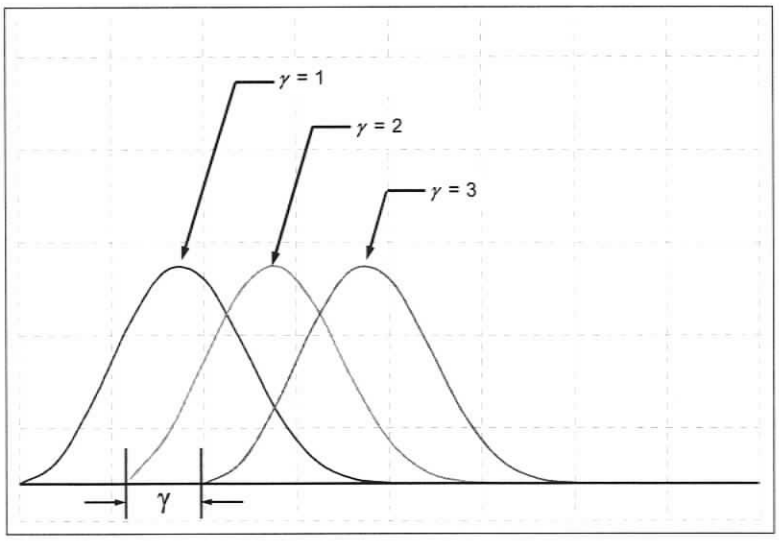

Figure 6-13, The effect of varying γ in a Weibull Distribution

It should be noted that η is always equal to the value that represents 63% of the data in the cumulative distribution function. While β is useful for understanding the shape of a distribution, η is not as meaningful as the median value for describing the scale of the distribution; therefore, the median is used in representing the data instead of η

Only two-parameter Weibull functions were used because it was difficult to successfully implement the correct γ parameter in an automated algorithm. Since both the Normal and Shear Force distributions begin at zero, the two-parameter Weibull function was adequate. The coefficient of friction and shear work distributions are not represented by a Weibull function because their distributions do not start at zero. The Shear Work distribution has negative values when an event recorded has a negative shear peak. This occurrence is rare, but still creates difficulties for representing the data accurately in the form of a two-parameter Weibull function. For these reasons, both the coefficient of friction and the shear work distributions require a three-parameter Weibull function. Further investigation is needed for automated determination of the parameter γ to allow these distributions to be fit to a Weibull distribution.

6.7 Summary

Force data was examined for all the experiments. It was found that there are a high percentage of bar-passing events compared to the total bar-crossings in the refiner. This indicates that pulp is likely present between the plates of the refiner at all times. A Weibull distribution function was fit to the normal shear force data and enables characterization of these distributions using two-parameters.

7 Results and Discussion II – Comparisons between Event Parameters and Specific Edge Load

7.1 Introduction

The relationships between bar-passing forces and other important event parameters with specific edge load were investigated at the refiner level. Force measurements are also compared with theoretical values and these comparisons are discussed.

7.2 Variations in Event Parameters at the Refiner Level

Figures 7-1 through 7-5 show the event parameter median values from the distributions for each data sample. A separate linear regression was completed for the experiments operated at 900 RPM and 1200 RPM.

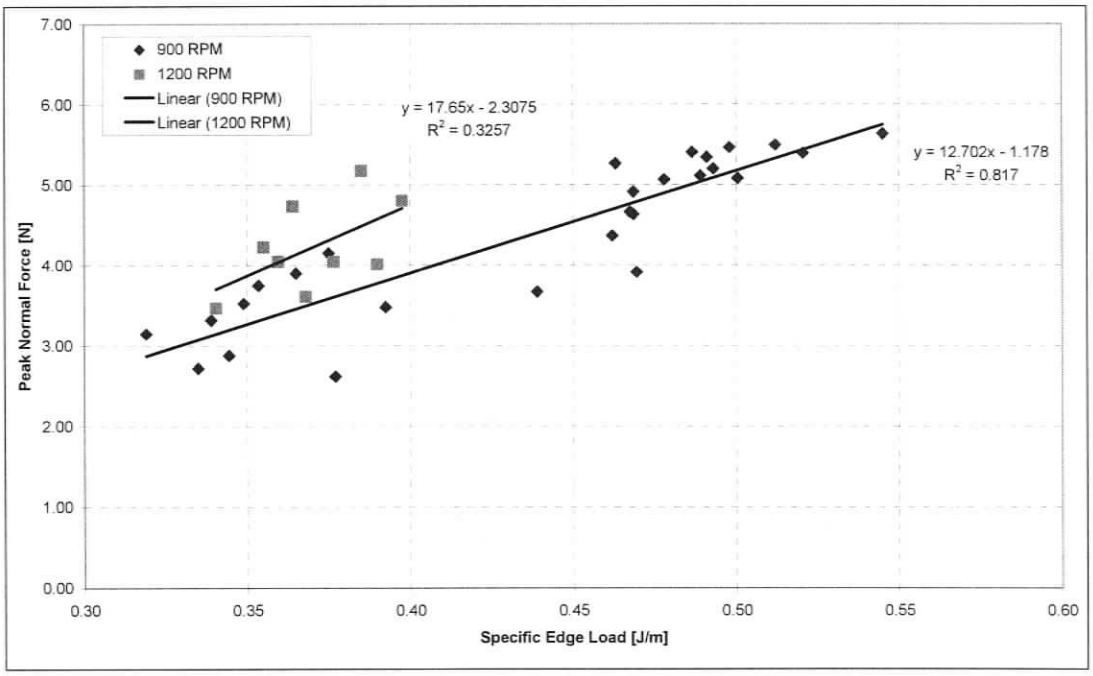

Figure 7-1, Comparison of Median Normal Forces at Various SEL

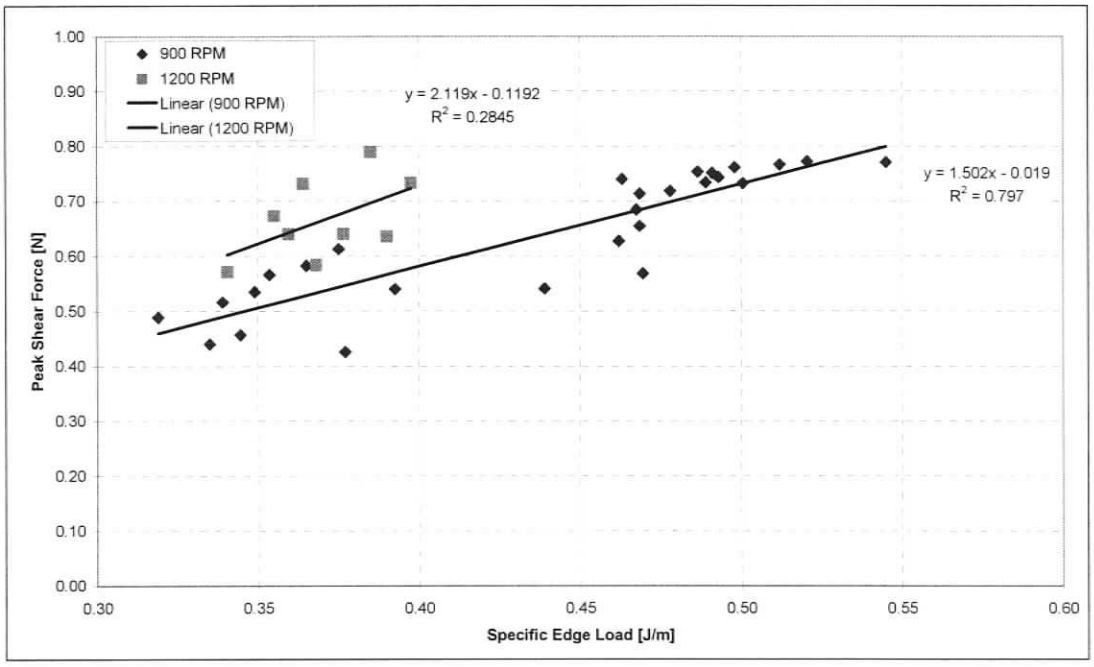

Figure 7-2, Comparison of Median Shear Forces at Various SEL

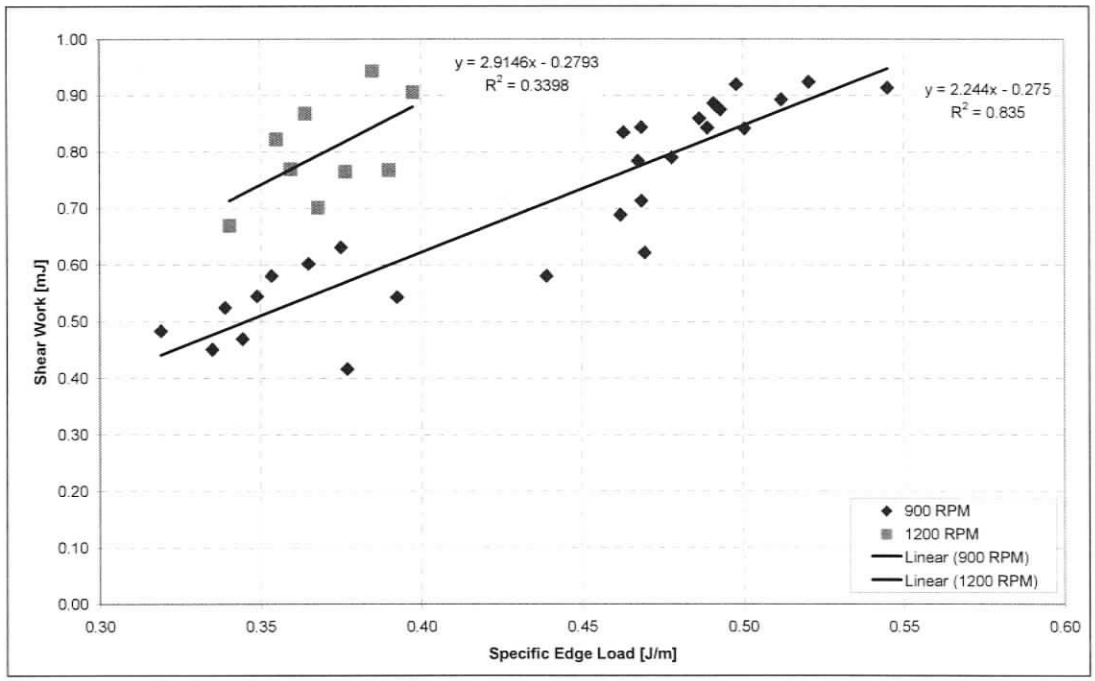

Figure 7-3, Comparison of Median Shear Work at Various SEL

Figures 7-1 through 7-3 show an increase in normal and shear force and also shear work with increasing specific edge load. Separate regressions have been fit to the 900 rpm and 1200 rpm data. There is a poor correlation value for the 1200 rpm data. Since experiment S12 (1200 rpm) was run under only a small range of SEL, the degree of scatter between data points has a more dominant effect on the correlation value. A wider range of SEL over experiments run at 1200 rpm is needed, therefore, to understand if there is a similarity in trend between experiments run at different speeds.

The median coefficient of friction values for each data sample were also analysed and compared at each SEL; a slight decrease was observed with increasing SEL. This is shown in Figure 7-4. The low correlation value for the 1200 rpm data is attributed to the same reasons stated previously.

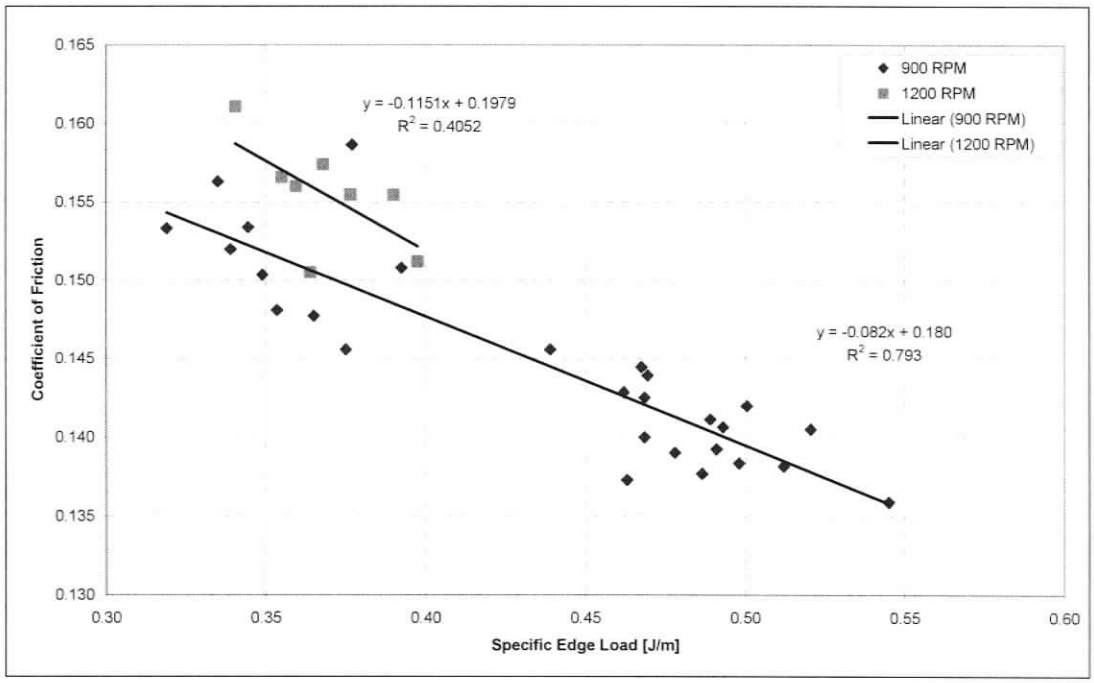

Figure 7-4, Comparison of the Median Coefficient of Friction at Various SEL

The effect of specific edge load on the mean shear lead was investigated and the results show that a change in SEL has no significant effect on the shear lead. The mean shear lead was calculated to be -0.005 ms, and can be seen in Figure 7-5.

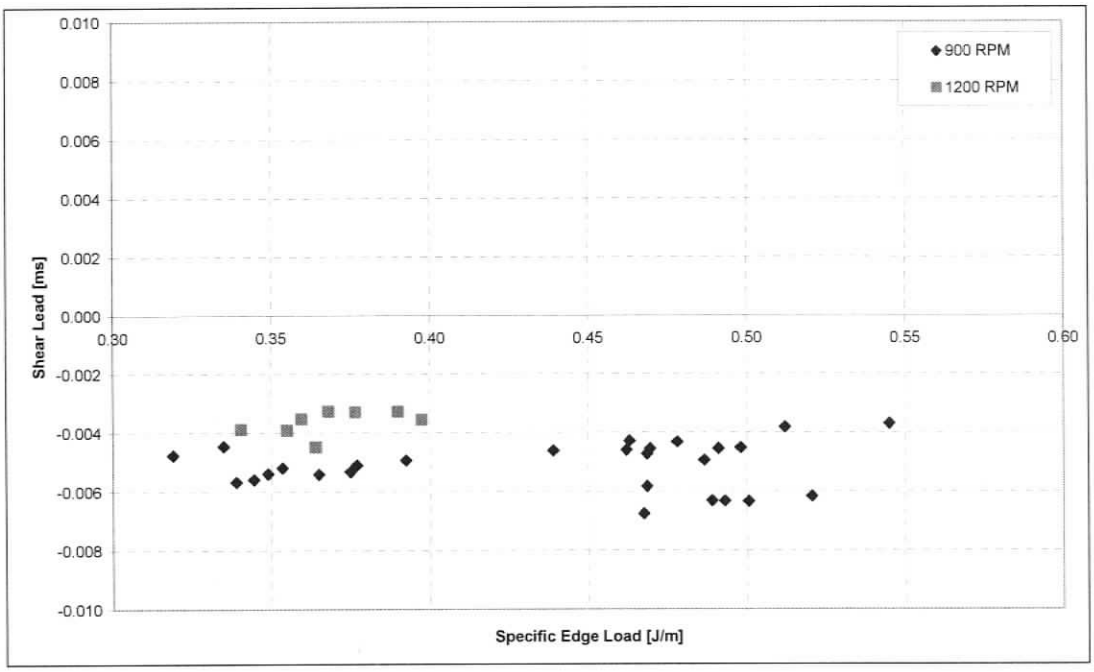

Figure 7-5, Comparison of the Median Shear Lead at Various SEL

It is apparent that from their respective distributions, the median forces increase with an increase in specific edge load. It is known that high forces result in fibre cutting and distributions allow one to predict the probability of these harmful forces at different SEL.

Median forces alone do not give any indication whether the shape or the scale of the distribution is the factor. For instance, if with increasing SEL, the same proportion of forces increase in magnitude, the median will increase but the shape of the distribution will stay the same. If with increasing SEL the lower magnitude forces do not increase in occurrence compared to the higher forces, the median will shift because the distribution's shape has changed. Figure 7-6 shows the Weibull shape parameter, β, for each data sample plotted against SEL. It is evident in this figure that, in these experiments, the shape of the normal and shear distributions are not strongly dependent on SEL.

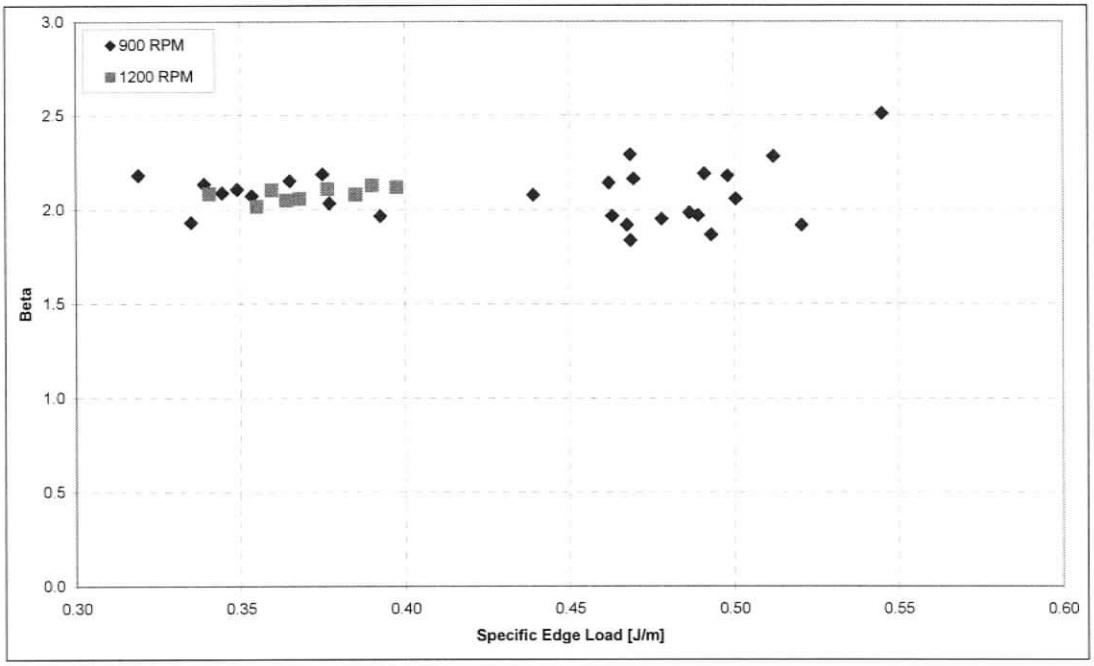

Figure 7-6, Comparison of the Normal Force Distribution Shape, β at Various SEL

7.3 Comparing Sensor Measurements with Theoretical Force Values

SEL is equal to the energy expended on the pulp over one bar-passing period, per unit length of bar. This is shown in Equation 7-1, derived by Kerekes et al. [11], where the work done per unit bar length during a bar-passing event is equal to an average shear force, F_S multiplied by the sliding distance, s in which the force is applied. The sliding distance is the same as the event length, Δt_{EVENT} used in Section 5.3.2. The bar angle[11] is ϕ. It is stressed that F_S is a force per unit bar length and is represented in terms of N/m.

[11] Defined in Section 3.2.2 as the angle on the tangent plane between the bars and the axis of the rotor, or in the case of a disc refiner, between the tangent plane and a radial line of the rotor

$$F_S \cdot s = \frac{SEL}{1 + 2\tan\phi} \qquad (7\text{-}1)$$

$$\therefore \hat{W}_S = \frac{SEL}{1 + 2\tan\phi} \qquad (7\text{-}2)$$

Where $\hat{W}_S$ is the work done per unit bar length during a bar-crossing. The average bar angle, ϕ, on the Conflo rotor was measured and is 29°.

If we multiply $\hat{W}_S$ by the length of bar, l, over which the work is done; the total work is equal to W_S.

$$W_{S\,SEL} = \frac{SEL}{1 + 2\tan\phi} \cdot l \qquad (7\text{-}3)$$

For an SEL of 0.5 J/m, the work done during a bar-passing event is 0.237 J per metre of bar length. The sensor length is 5 mm; therefore the total expected work done on the sensor during a bar-passing event is 1.19 mJ.

The average shear work measured by the sensor per bar-passing event varies between data samples. Therefore the regression line shown in Figure 7-3 is used as an average shear work measured by the sensor per bar-passing event. This regression line is shown in Equation 7-4.

$$W_{S\,SENSOR} = 2.244 \cdot SEL - 0.275 \qquad (7\text{-}4)$$

Where W_S is the work measured by the sensor.

Using Equation 7-4, the average work done on the sensor for an SEL of 0.5 J/m is 0.847 mJ.

In addition to the time-varying shear forces measure by the sensor, it is thought that there is a steady shear force that arises from the viscous drag between the rotor and the stator. As discussed in Section 3.3.1, the sensor and charge amplifier do not respond to steady state or low frequency loads.

A rough approximation of the work done by this steady viscous force in the refiner was attempted assuming Couette flow between two smooth cylinders [22]. The sensor is located roughly in the centre of the axial length of refiner. It is, therefore, assumed that the sensor measures the average force applied to a refiner bar. The shear stress due to Couette flow at the sensor location is:

$$\tau_S = \frac{\mu r_i \omega}{r_o - r_i} \qquad (7\text{-}5)$$

Where μ is the dynamic viscosity of the pulp, ω is the angular velocity of the refiner, r_i and r_o are the radius of the rotor and stator, respectively, at their bar tips.

The shear work done on the sensor per bar-crossing is equal to:

$$W_S = \tau_S \cdot l \cdot b \qquad (7\text{-}6)$$

Where l is the sensor length and b is the bar spacing.

A theoretical value for pulp viscosity was developed by Kerekes et al. [23]:

$$\mu = 1.5 \cdot 10^{-3} C_m^{\,3.1} \qquad (7\text{-}7)$$

The consistency of the pulp during trials was 3.15%. Using Equation 7-7, this corresponds to a pulp viscosity of 0.053 Ns^2/m.

The radial location, r_o of the sensor is 0.136 m. Although the rotor-stator gap was not measured in the experiments, it is known by the operators that, under normal operating conditions, it is on the order of 0.15 mm. Therefore, for a rotor speed of 900 rpm, the shear stress is equal to 4493 N/m^2. With a sensor length of 5 mm and a bar spacing of 6.4 mm, the shear work done on the sensor by viscous effects is 0.144 mJ.

Combining the viscosity calculations with the shear work measured by the sensor in the refiner, the total shear work done over the sensor during a bar-crossing is 0.991 mJ. Comparing this value with the value of 1.19 mJ obtained using the SEL; the values move closer to each other. It is stressed that this is a rough approximation; however, it provides insight as to the possibility of a non-zero, steady force present in the refiner that contributes to the motor load.

A comparison between the work expended during a bar-passing event based on SEL and sensor measurements is illustrated in Figure 7-7. The addition of a non-zero force contributing to shear work on the sensor, such as a viscous force, is included.

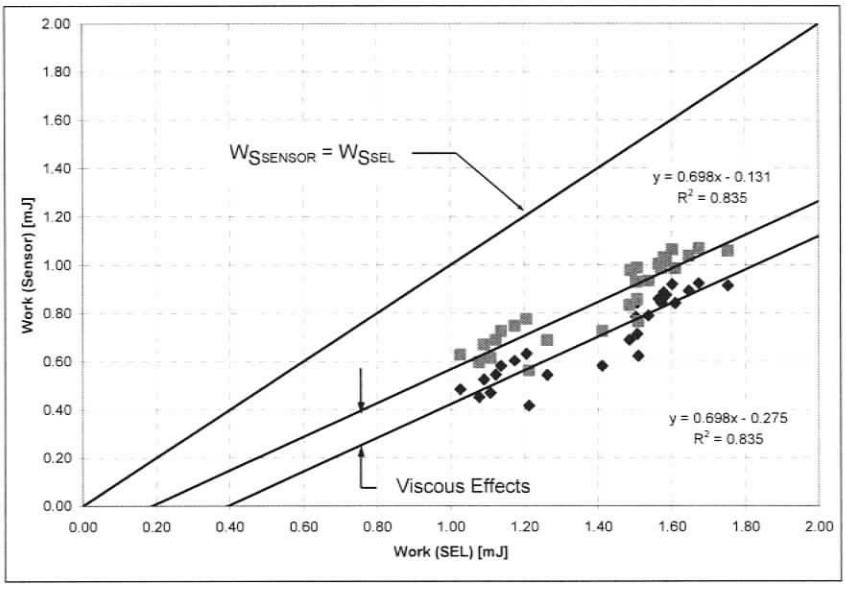

Figure 7-7, Comparison between Work measured by the sensor and Work calculated from SEL

The calculations assume that the surfaces on the refiner are smooth, that the pulp consistency is uniform throughout the refiner and that the rotor is cylindrical. The Conflo is conical in shape, not cylindrical and the plate gap is not known. In addition, the rotor and stator are not concentric (this is discussed in Section 8.4.2). All of these factors will contribute to higher viscous forces compared to these calculations.

7.4 Summary

Event parameters were analysed at the refiner level. Normal and shear forces along with shear work increase in magnitude with an increase in specific edge load. The coefficient of friction of the pulp varies between 0.13 and 0.16 and slightly decreases with an increase in specific edge load. The shape of the normal and shear force distributions are independent of changes to specific edge load. It is known that high forces result in fibre cutting, and these results show that with increasing SEL, both normal and shear forces increase. These distributions allow one to predict the probability of harmful fibre cutting forces at different SEL. The forces measured are lower than the expected theoretical values. Viscous effects in the refiner are offered to account for work not measured during a bar-passing event.

With only a small range of specific edge load for experiment S12, the effects of SEL on bar-passing events are difficult to analyse. Therefore, it is recommended that future trials explore the effect of speed on normal and shear forces by comparing different speeds at a wide range of SEL.

8 Results and Discussion III – Segment and Bar Variations between Event Parameters and Specific Edge Load

8.1 Introduction

The relationships between bar-passing forces and specific edge load were investigated. The data was analysed on three different levels: the refiner level, which included all of the bar-passing events within a sample; the segment level, which displays bar-passing events sorted between plate segments; and finally the individual bar level, where three bars were analysed within a particular plate segment.

8.2 Variations in Event Parameters at the Segment Level

Figure 8-1 shows the distribution of forces over each segment for experiment S9-1 and the Weibull calculated median normal forces for their corresponding plate segment are as identified in Table 8-1. The median normal force at each segment increases from segments #1-4 and then decreases from segments #4-7.

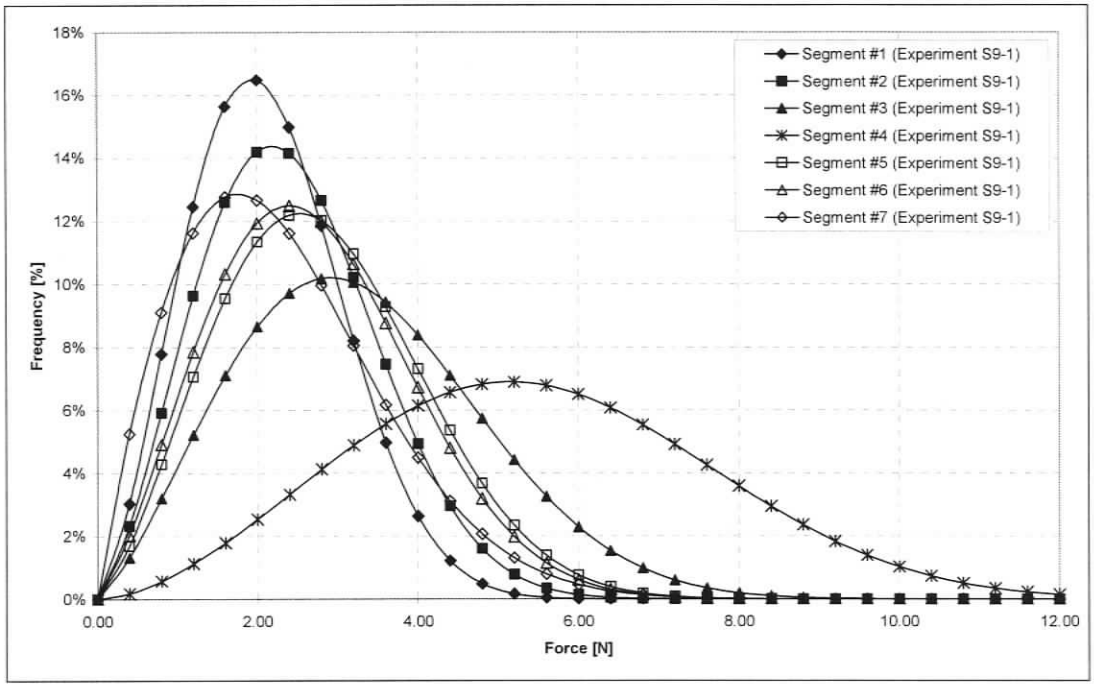

Figure 8-1, Comparison of Normalized Normal Force Distributions for Each Segment (Experiment S9-1. Time: 9:06:00-9:06:05. [SEL=0.38 J/m])

Table 8-1, Median Forces at each plate segment (Experiment S9-1. Time: 9:06:00-9:06:05. [SEL=0.38 J/m])

Segment #	Median Normal Force [N]
1	2.07
2	2.35
3	3.18
4	5.37
5	2.73
6	2.61
7	2.15

Figure 8-2 shows the median normal forces for each segment with respect to changes in SEL. The same trends occurring with median values on the refiner level extend to the segment level; median values increase with an increase in SEL. However, the rate at which these values increase varies depending on the plate segment. This same pattern occurs for shear forces and shear work for all of the samples taken during the refining trials (Figure 8-3 and Figure 8-4, respectively). The implications of different force magnitudes at each segment

will be discussed in Section 8.4. The regression lines are included in Tables 8-2 through 8-4, respectively, with their R^2 values to avoid cluttering the figures.

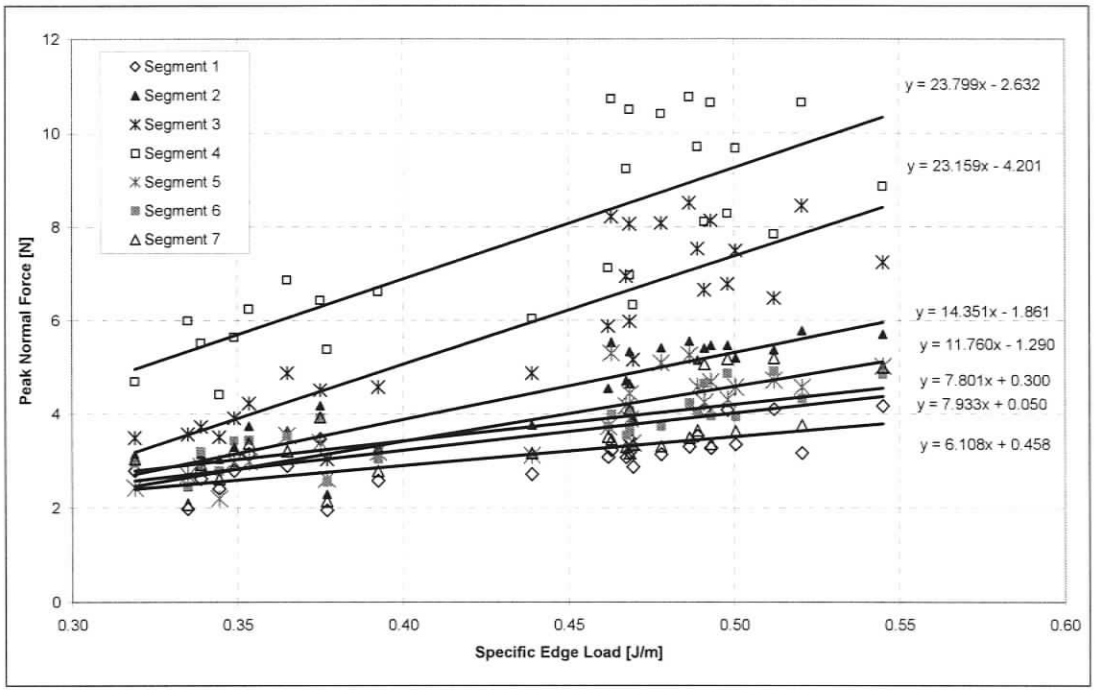

Figure 8-2, Comparison of Median Normal Forces for Each Plate Segment at Various SEL.

Table 8-2, Linear regression values for all plate segments (Normal Forces)

Segment	Slope	Y-Intercept	R^2
1	6.108	0.458	0.526
2	14.351	-1.861	0.808
3	23.159	-4.201	0.761
4	23.799	-2.632	0.620
5	11.760	-1.290	0.754
6	7.801	0.300	0.628
7	7.933	0.050	0.447

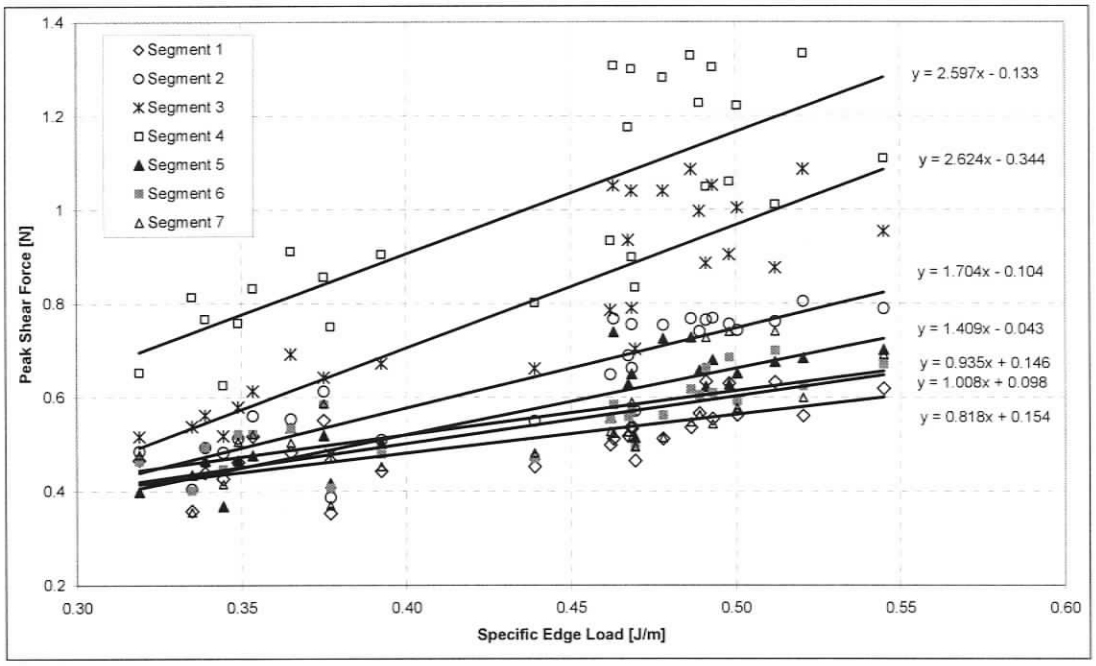

Figure 8-3, Comparison of Median Shear Forces for Each Plate Segment at Various SEL

Table 8-3, regression values for all plate segments (Shear Forces)

Segment	Slope	Y-Intercept	R^2
1	0.818	0.154	0.564
2	1.704	-0.104	0.798
3	2.624	-0.344	0.758
4	2.597	-0.133	0.614
5	1.409	-0.043	0.750
6	0.935	0.146	0.629
7	1.008	0.098	0.488

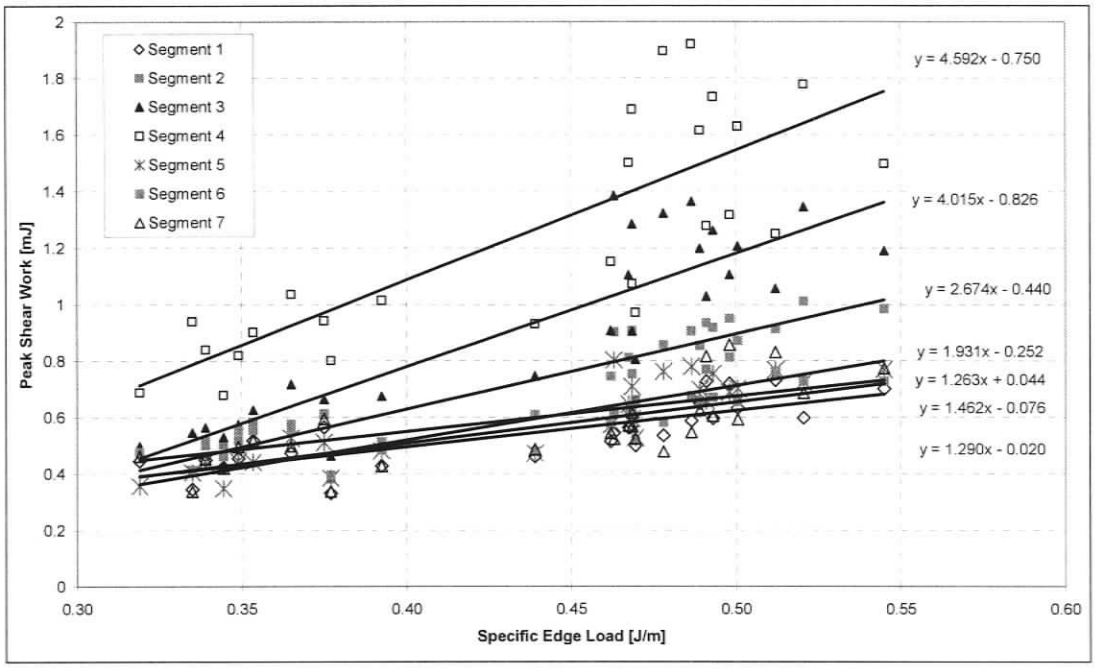

Figure 8-4, Comparison of Median Shear Work for Each Plate Segment at Various SEL

Table 8-4, Linear regression values for all plate segments (Shear Work)

Segment	Slope	Y-Intercept	R^2
1	1.290	-0.020	0.650
2	2.674	-0.440	0.858
3	4.015	-0.826	0.768
4	4.592	-0.750	0.584
5	1.931	-0.252	0.796
6	1.263	0.044	0.622
7	1.462	-0.076	0.538

8.3 Variations in Event Parameters at the Bar Level

Data for three bars on segment #4 were examined to reveal trends that might exist among forces at a particular bar with changes in refining conditions. Segment #4 was chosen for analysis since the forces at this segment are the highest and most regular occurring of all segments on the rotor. The three bars selected are bars #4, #8, and #12. These bars are equidistant from each other on the segment: one is located in the middle of the segment and the other two are located one quarter and three quarters of the way into the segment.

Figures 8-5 through 8-7 show the median normal forces for each bar with respect to changes in SEL. The trends present at the refiner and segment levels extend to the individual bar level. It is noted that the slopes of the lines in these figures are similar to the slope for all on segment #4 (shown in Figure 8-5) and all have similar R^2 values. The variations between the three bars on segment #4 are much less than the variations from segment to segment. Tables 8-5 through 8-7 show the occurrence ratios for bars #4, #8 and #12 on segment #4. One can see that there is still a high occurrence of forces measured at the bar level. The correlation between the trend lines and the data are not as high as the correlations present in at the refiner and segment levels. This may be because at the bar level there are less data points from which the median values of each distribution were taken. With tighter refining conditions, larger data samples would be able to be analysed and would increase the number of data points present in the bar level distributions.

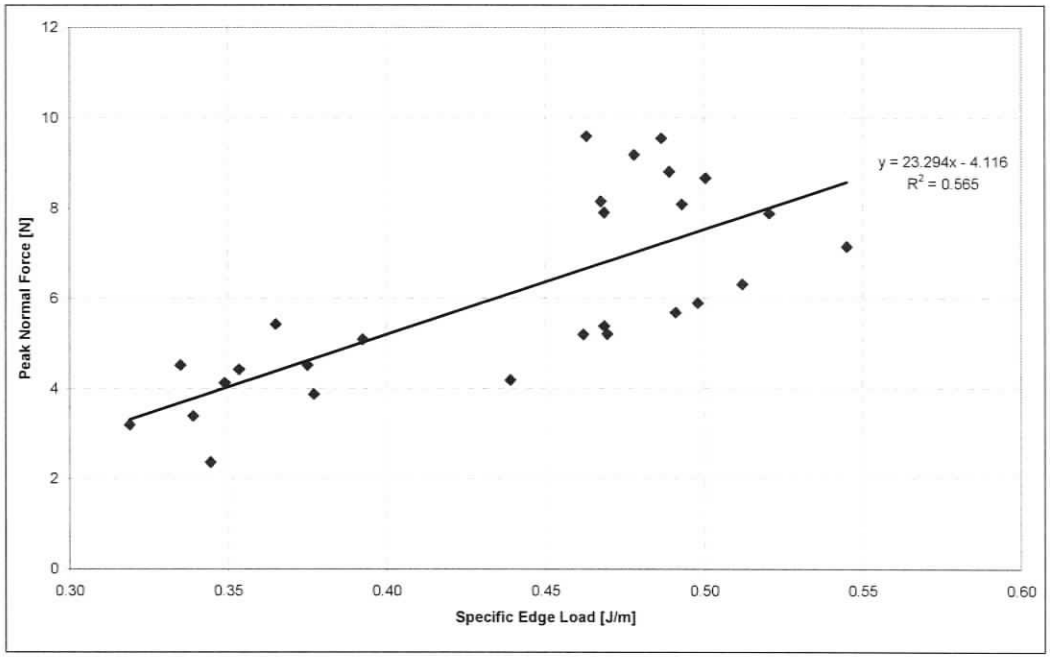

Figure 8-5, Comparison of Median Normal Forces for Bar #4 on Segment #4 at Various SEL.

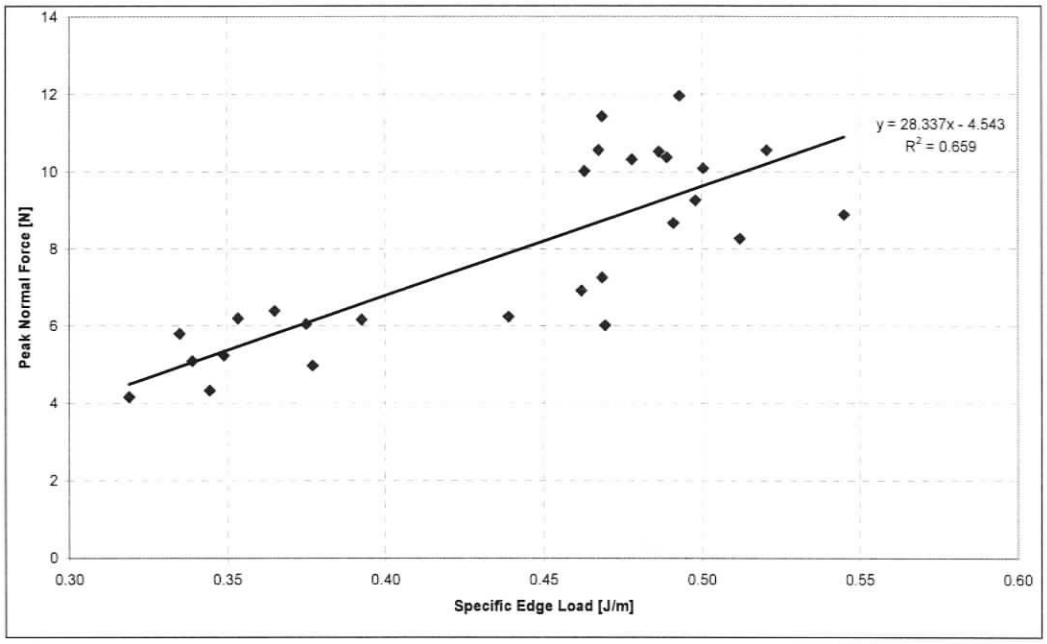

Figure 8-6, Comparison of Median Normal Forces for Bar #8 on Segment #4 at Various SEL.

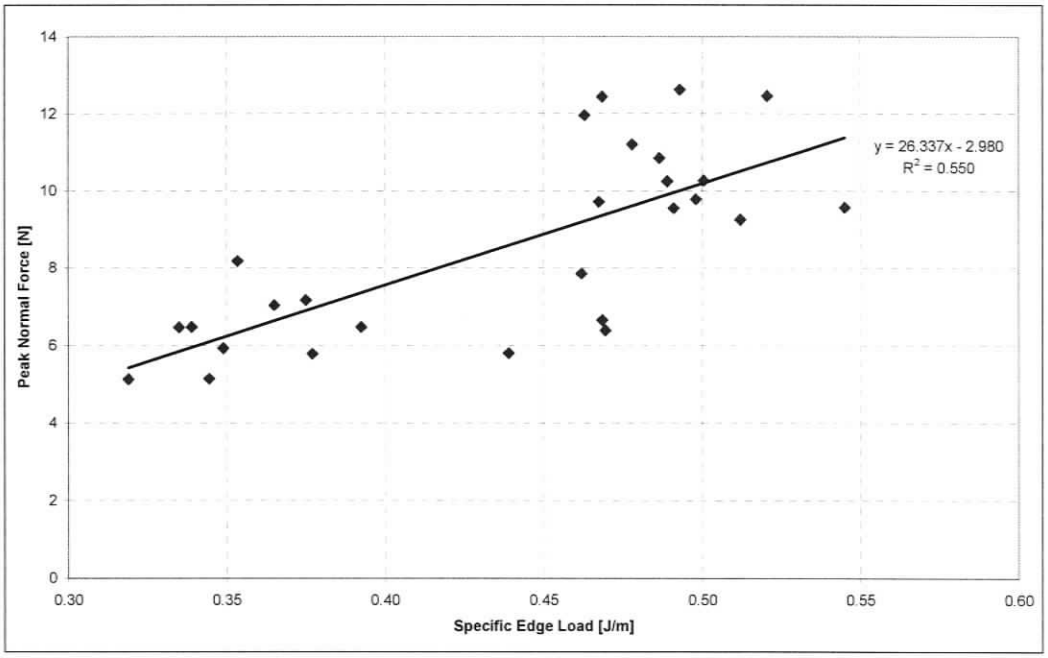

Figure 8-7, Comparison of Median Normal Forces for Bar #12 on Segment #4 at Various SEL.

Table 8-5, Occurrence Ratio of Events for Bar #4 on Segment #4

Experiment \ Sample	1	2	3	4	5	6	7	8	9
S12	0.95	0.99	0.99	0.98	0.99	0.99	0.98	0.99	0.99
S9	0.88	0.95	0.90	0.98	0.95	1.00	0.99	0.99	0.97
S9B1	0.96	0.98	0.99	0.97	1.00	0.99	0.99	1.00	1.00
S9B2	0.99	1.00	1.00	0.97	0.99	0.99	0.98	0.98	0.99

Table 8-6, Occurrence Ratio of Events for Bar #8 on Segment #4

Experiment \ Sample	1	2	3	4	5	6	7	8	9
S12	0.99	0.98	0.99	0.99	1.00	0.99	0.99	0.99	0.99
S9	0.97	1.00	0.94	0.99	0.98	1.00	0.98	0.97	0.99
S9B1	1.00	0.98	0.99	0.97	1.00	0.99	0.99	0.99	1.00
S9B2	0.99	0.98	1.00	0.97	0.98	0.97	0.97	0.99	0.99

Table 8-7, Occurrence Ratio of Events for Bar #12 on Segment #4

Experiment \ Sample	1	2	3	4	5	6	7	8	9
S12	0.98	0.99	0.99	0.98	1.00	0.99	0.99	0.97	0.96
S9	1.00	0.98	0.94	0.99	0.98	1.00	0.98	0.99	1.00
S9B1	0.99	1.00	0.99	0.99	1.00	0.99	0.99	1.00	0.99
S9B2	0.99	1.00	1.00	0.99	0.99	0.99	0.98	0.99	0.99

8.4 The Effect of Rotor Tram on Force Levels

The investigation of forces measured in the refiner showed cyclic variations in force magnitudes between the segments on the rotor. In this section of the chapter, the implications of these variations and their relation to the alignment of the rotor are discussed.

8.4.1 Force Profiles

As alluded to in Section 8.2, a pattern was evident over one revolution of the rotor. It was observed that the highest forces regularly occur at segment #4. Figure 8-8 and Figure 8-9

show both normal and shear forces in the refiner over 0.3 s. At a refiner speed of 900 rpm, this is equal to 4.5 revolutions of the rotor.

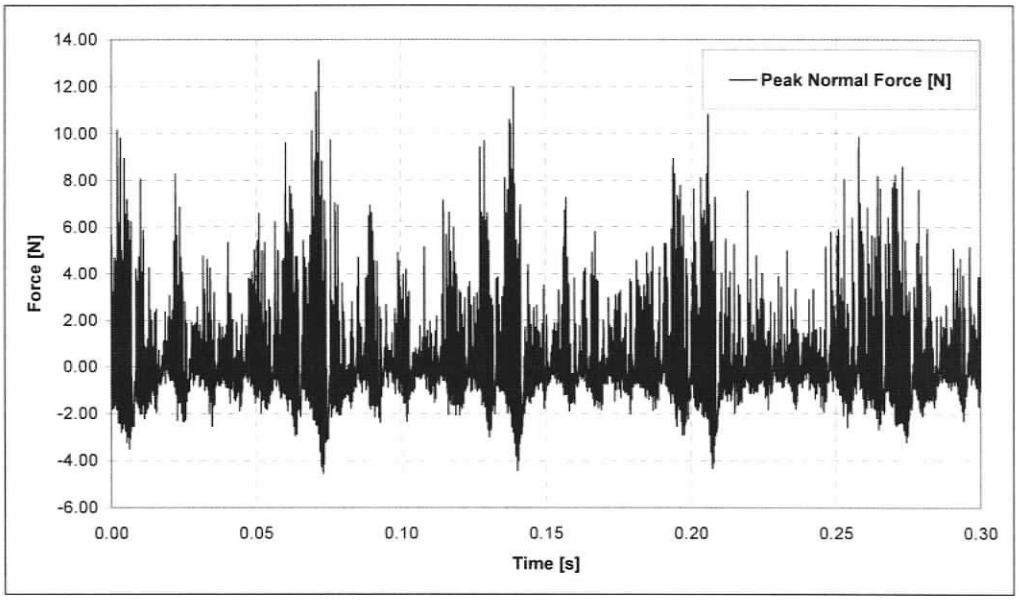

Figure 8-8, Normal Force Data showing the Effect of Out-of-Tram (Experiment S9B1-1. Time: 9:22:50.000-9:22:50.333. [SEL=0.47 J/m])

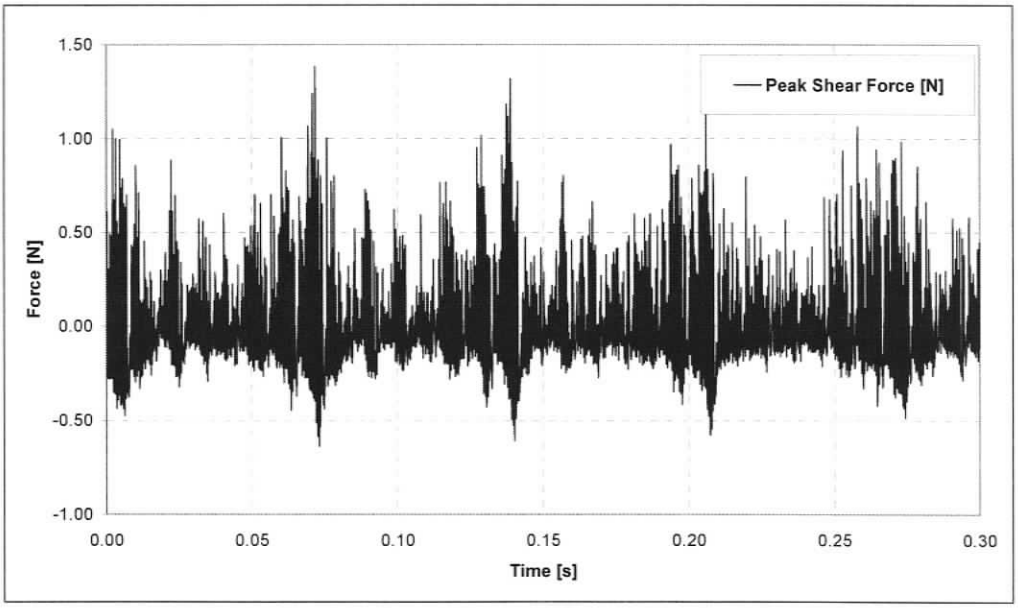

Figure 8-9, Shear Force Data showing the Effect of Out-of-Tram (Experiment S9B1-1. Time: 9:22:50.000-9:22:50.333. [SEL=0.47 J/m])

The cyclical variation in refining forces with each revolution of the rotor is clearly visible in Figure 8-8 and Figure 8-9. The variation appears in both the normal force data and the shear force data. In some cases the force variation is as large as 300%.

8.4.2 Rotor Alignment

After initial review of the data this pattern was immediately evident and attributed to rotor out-of-tram. To check this hypothesis, the rotor was removed from the refiner and the hub which the rotor mounts to was measured for run-out. The rotor hub was retrofitted onto a larger shaft and had a run-out of 0.06 mm. This misalignment is small in mechanical terms, but when compared to the plate gap of 0.15 mm, it is substantial. This means that with an average plate gap of 0.15 mm, the actual gap will vary between 0.09 mm and 0.24 mm. Assuming that higher forces are related to smaller gaps, the smallest gap occurs at segment 4 and the largest at segment 1. The plate gap at each segment is estimated to be as shown in Table 8-8.

Table 8-8, Estimated plate gap for each segment on the rotor

Segment #	Plate Gap [mm]	Plate Gap [in]
1	0.20	0.0080
2	0.16	0.0064
3	0.11	0.0044
4	0.09	0.0035
5	0.11	0.0044
6	0.16	0.0064
7	0.20	0.0080

8.4.3 Force Magnitudes

Figures 8-10 through 8-13 show comparisons between median forces for each experiment. The fourth segment clearly shows the highest median forces in all cases. Segments #1 and #7 have the lowest force magnitudes and are diametrically opposite to segment #4.

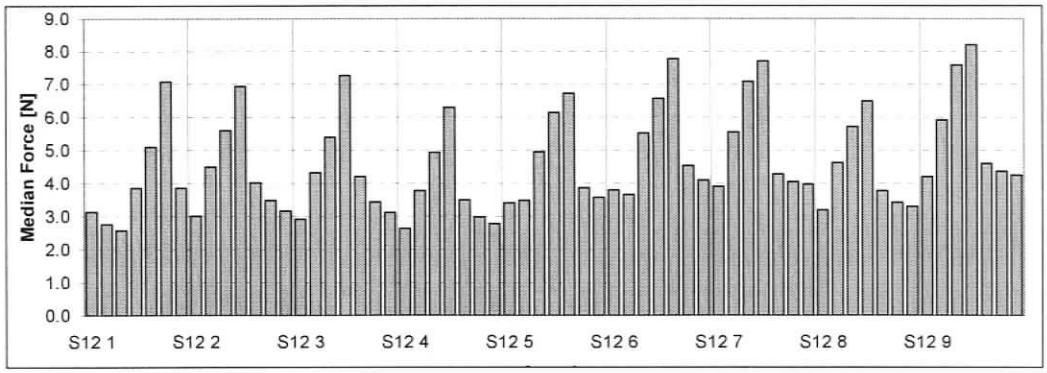

Figure 8-10, Median Normal Forces recorded at each Plate Segment (Experiment S12)

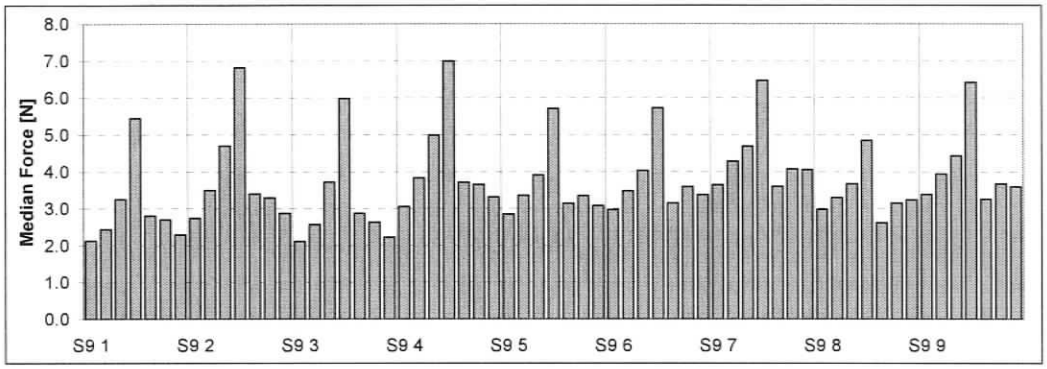

Figure 8-11, Median Normal Forces recorded at each Plate Segment (Experiment S9)

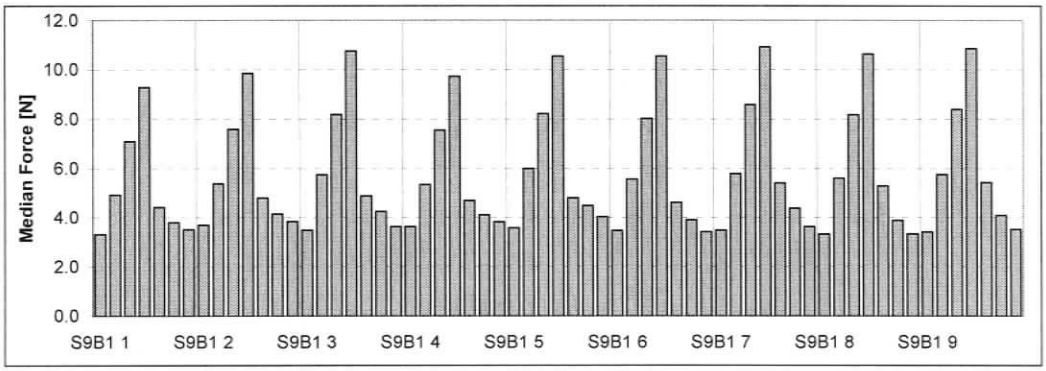

Figure 8-12, Median Normal Forces recorded at each Plate Segment (Experiment S9B1)

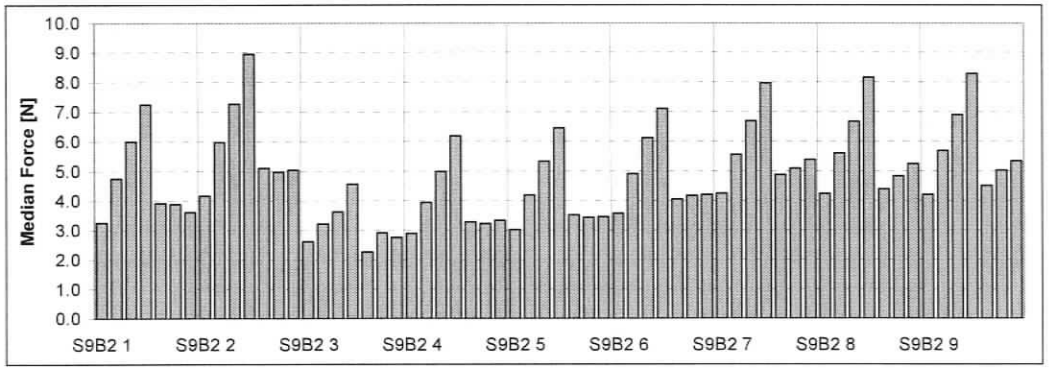

Figure 8-13, Median Normal Forces recorded at each Plate Segment (Experiment S9B2)

8.5 Summary

Event parameters were analysed at the segment and bar levels. Normal and shear forces along with shear work increase in magnitude with an increase in specific edge load. These trends are similar to the trends present with median forces investigated at the refiner level. Variations in the normal and shear forces are present between plate segments. Measurements of shear and normal forces during bar-passing events revealed a strong relationship between refiner tram and force magnitudes. Out of tram on the order of 40% of the gap can result in variations in peak forces on the order of 300%. Assuming the out of tram in industrial refiners is at equivalent levels, it is apparent that tram plays an important role in the distribution of forces that occur in low consistency refining. Differences between experimental conditions could have a greater effect the force distributions between experiments on the individual bar level than on refiner and segment levels because combining data from multiple bars located at different places throughout the refiner will have a smearing effect on the data.

9 CONCLUSIONS

A piezoelectric force sensor was developed for measuring forces on bars during low consistency mechanical pulp refining. The design is based on a sensor previously designed for high consistency refining with a modified probe. The altered probe mimics the bar profile of a Sunds Defibrator Conflo® JC-00 refiner. The lowest natural frequency of the sensor in a mounted configuration is 15 kHz. This is approximately five times greater than the bar-passing frequency of the refiner. The Conflo refiner stator was altered to accept the sensor, providing accurate alignment and orientation of the sensor probe with a stator bar, while also firmly securing the sensor.

RFS4-LC is capable of measuring forces in low consistency refiners over a larger range of conditions than previous sensors. This improvement can be attributed to several design advances, of which the following stand out: a stiffer housing and mounting technique, the use of piezoelectric ceramics as the transducing material, a positive seal against the ingress of water, and the use of high-speed data acquisition systems. As a result of all these enhancements, the entire waveform from each bar-passing event is captured for a detailed analysis. Compared to existing LC sensor designs, RFS4-LC is smaller in size, increasing the capability of installing the sensor in a wider range of refiners. The transducing materials in RFS4 are piezoelectric ceramic elements, which provide greater sensitivity over strain-based transducers (tensiometers). Previously developed sensors have relied on large deflections in the protruding element to measure forces, thus limiting their sensitivity.

During the trials, the motor load and feed rates fluctuated causing the actual refining conditions to be quite different from the targeted levels. Data was extracted at pseudo-steady state refining conditions for analysis.

Resonance of the sensor was present in the data following forces occurring during bar-passing events. A custom algorithm was developed by Mr. Dustin Olender and the author that successfully identifies bar-passing events out of the force data. Another custom algorithm was developed by the author that successfully matches identified events with their

corresponding bar and segment locations on the rotor. Data can be extracted and analysed based on the segment and individual bar that the bar-passing event occurred.

The results show that a bar-passing event occurs for almost all bar-crossings. The average occurrence of bar-passing events detected per bar crossing is 96%. The regularity of these events suggests that there is almost always pulp present between the sensor and the rotor. By extrapolation, it seems likely that this condition may occur throughout the refiner.

Analysis shows that the two-parameter Weibull function is a good fit to the normal and shear force distributions. The shape of the force distributions is relatively independent of changes to specific edge load. However, the median forces increase with an increase in SEL. The peak coefficient of friction varies between 0.13 and 0.16 during the trials, decreasing slightly with an increase in SEL. Knowledge of the distributions could allow for comparisons to be drawn between refining conditions and force magnitudes and profiles, and provide greater insight to the mechanisms responsible for fibre development in papermaking. For instance, knowledge of the distribution of forces could allow one to predict the probability of forces responsible for fibre cutting at different SEL, with "In Process" control using force measurements.

The forces measured by the sensor are lower than theoretically calculated values based on SEL. This underestimation is attributed to pseudo steady viscous forces, not measured by the sensor. An estimate of the viscous force was calculated based on a Couette flow approximation to provide an explanation for this discrepancy.

Finally, a relationship between refiner tram and force magnitudes was discovered in the data. Out of tram on the order of 40% of the gap causes variations in peak forces on the order of 300%. Therefore, out of tram plays an important role in the distribution of forces that occur in low consistency refining.

10 RECOMMENDATIONS

Comparisons made in this study between refining conditions and forces might be subject to transient effects in the motor load and feed rate. Therefore future experimentation should focus on tighter controls, or a larger range of experimental conditions. Smaller variations in the refining conditions will also allow for pulp samples to be analyzed and compared with the force data.

It is recommended that comparisons be made between the force measurements with pulp present and with only water passing through the refiner at the same plate gap to better approximate viscous effects in the refiner.

If possible, eliminating out-of-tram in the Conflo refiner will narrow the distribution of forces at each refining condition. This might allow for better comparison of trends between force data and refining conditions.

Finally, modifications to the sensor are recommended to minimize resonance. This can be accomplished using a shorter probe combined with deeper mounting into the stator, such that part of the sensor housing is exposed in the grooves between bars.

REFERENCES

[1] KAPPEL, J., "Mechanical pulps: From wood to bleached pulp" TAPPI Press., Atlanta, GA., (1999).

[2] SMOOK, G.A., "Handbook for pulp and paper technologists", 2nd Ed., Angus Wilde Publications., Vancouver, BC., (1992).

[3] NORDMAN, L., LEVLIN, J.E., MAKKONEN, T., and JOKISALO, H., "Conditions in an LC-refiner as observed by physical measurements.", Paperi ja Puu. 63(4):169-180, (1981).

[4] SUNDS DEFIBRATOR, "Conflo refiners for stock preparation and recycled fiber" Product Application Note., Stockholm, Sweden, (1997).

[5] GONCHAROV, V.N., SMIRNOVA, E.A., and SHEMYAKIN, E.V., "Method for the determination of stresses between refiner blades.", Bumazh. Promst. (27):134-138, English Trans., (1970).

[6] GONCHAROV, V.N., "Force factors in a disk refiner and their effect on the beating process.", Bumazh. Promst. 12(5):12-14, English Trans., (1971).

[7] SENGER, J.J., "The forces on pulp fibres during refining.", M.A.Sc. Thesis, Dept. of Mechanical Engineering, University of British Columbia, Vancouver, BC (1998).

[8] SENGER, J.J. and OUELLET, D., "Factors affecting the shear forces in high consistency refining.", Journal of Pulp and Paper Science. 28(11):364-369 (2002).

[9] MARTINEZ, D.M., BATCHELOR, W.J., KEREKES, R.J., and OUELLET, D., "Forces on fibres in low consistency refining: Normal force.", Journal of Pulp and Paper Science. 23(1):J11-18 (1997).

[10] BATCHELOR, W.J., MARTINEZ, D.M., KEREKES, R.J., and OUELLET, D., "Forces on fibres in low consistency refining: Shear force.", Journal of Pulp and Paper Science. 23(1):J40-45 (1997).

[11] KEREKES, R.J., Private Communication. December, 2005.

[12] MIHELICH, W.G., WILD, D.J., BEAULIEU, S.B., BEATH, L.R., "Single-stage chip refining – some major operating parameters and their effects on pulp quality", International Mechanical Pulping Conference, Ottawa, 78-82, (1971).

[13] OHLS, P.E., and SYRJÄNEN, A., "Importance of disc parallelism in single disc chip refiner", International Mechanical Pulping Conference, San Francisco, 153-161, (1975).

[14] FRAZIER, W.C., "Refiner tram and its contribution to pulping and pulp movement in high consistency refiners", International Mechanical Pulping Conference, Oslo, Norway, 38-41, (2005).

[15] BANKES, A., "The design and development of a mechanical wood pulp force sensor", M.A.Sc. Thesis, Dept. of Mechanical Engineering, Queen's University, Kingston, ON (2000).

[16] SIADAT, A. "Measurement of Forces on Refiner Bars", M.A.Sc. Thesis, Dept. of Mechanical Engineering, University of British Columbia, Vancouver, BC (2001).

[17] SIADAT, A., BANKES, A., WILD, P.M., SENGER, J., OUELLET, D., "Development of a Piezoelectric Force Sensor for a Chip Refiner," Institution of Mechanical Engineers, Part E, Journal of Process Mechanical Engineering, 217: 133-140, (2003).

[18] SENGER, J., OLMSTEAD, M., OUELLET, D., WILD, P.M., "Measurement of Shear and Normal Forces in the Refining Zone of a TMP Refiner," Journal of Pulp and Paper Science, 30(9): 247-251, (2004).

[19] SENGER, J., OUELLET, D., WILD, P.M., BYRNES, P., SABOURIN, M., "A Technique to Measure Residence Time in TMP Refiners Based on Inherent Process Fluctuations," International Mechanical Pulping Conference, Oslo, Norway, 19-25 (2005).

[20] Custom LabVIEW LC Refiner Control Front Panel. Pulp and Paper Research Institute of Canada, (2005).

[21] TAN, P., "Four approaches to inference on Weibull parameters" Dept. of Mathematics, Carleton University, ON (1974).

[22] MUNSON, B.R., YOUNG, D.F., OKIISHI, T.H., "Fundamentals of fluid mechanics" 3rd Ed. John Wiley and Sons, Inc., Toronto. (1998).

[23] KEREKES, R.J., BENNINGTON, C.P., "Power requirements for pulp suspension fluidization" TAPPI Journal, 79(2): 253-258, (1996).

APPENDIX A – REFINING CONDITIONS

A.1. Experiment S9

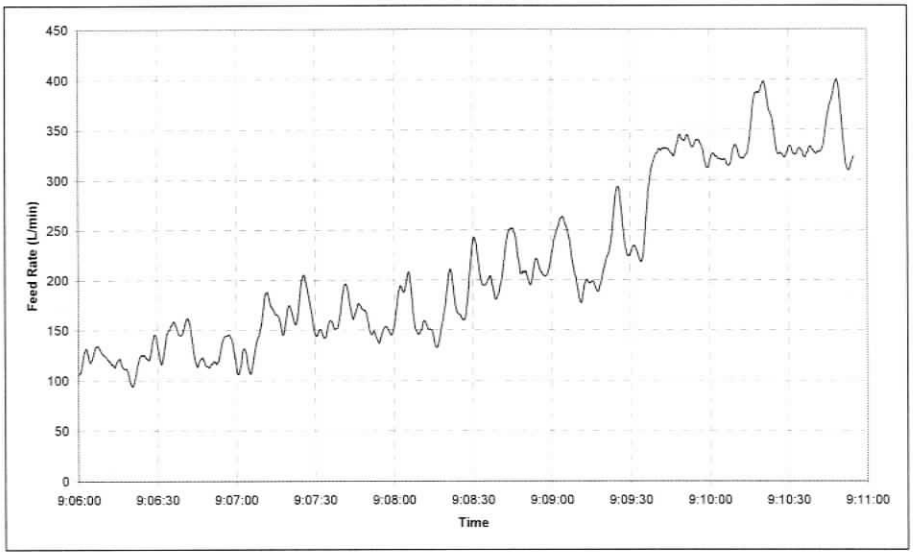

Figure A-1, Feed Rate (Experiment S9)

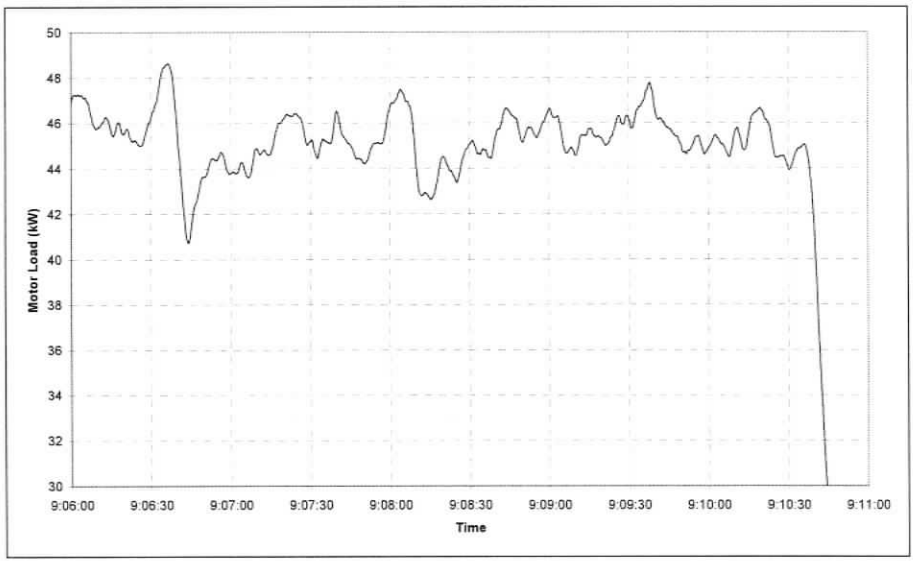

Figure A-2, Motor Load (Experiment S9)

Table A-1, Calculated Sample Conditions (Experiment S9)

	S9						BOF:	9:00:51 AM	
	Specific Energy			SEL			Time		
	Low	High	Avg	Low	High	Avg	Begin	End	[s]
S9 1	117	142	129.5	0.377	0.377	0.377	9:06:00 AM	9:06:05 AM	5
S9 2	92	142	117.0	0.390	0.395	0.393	9:06:34 AM	9:06:38 AM	4
S9 3	84	105	94.5	0.330	0.340	0.335	9:06:59 AM	9:07:07 AM	8
S9 4	77	110	93.5	0.364	0.366	0.365	9:07:20 AM	9:07:27 AM	7
S9 5	90	110	100.0	0.338	0.340	0.339	9:07:48 AM	9:07:52 AM	4
S9 6	73	93	83.0	0.348	0.350	0.349	9:07:54 AM	9:07:58 AM	4
S9 7	74	109	91.5	0.370	0.380	0.375	9:08:00 AM	9:08:08 AM	8
S9 8	58	63	60.5	0.318	0.320	0.319	9:08:12 AM	9:08:17 AM	5
S9 9	42	43	42.5	0.350	0.357	0.354	9:09:13 AM	9:09:22 AM	9

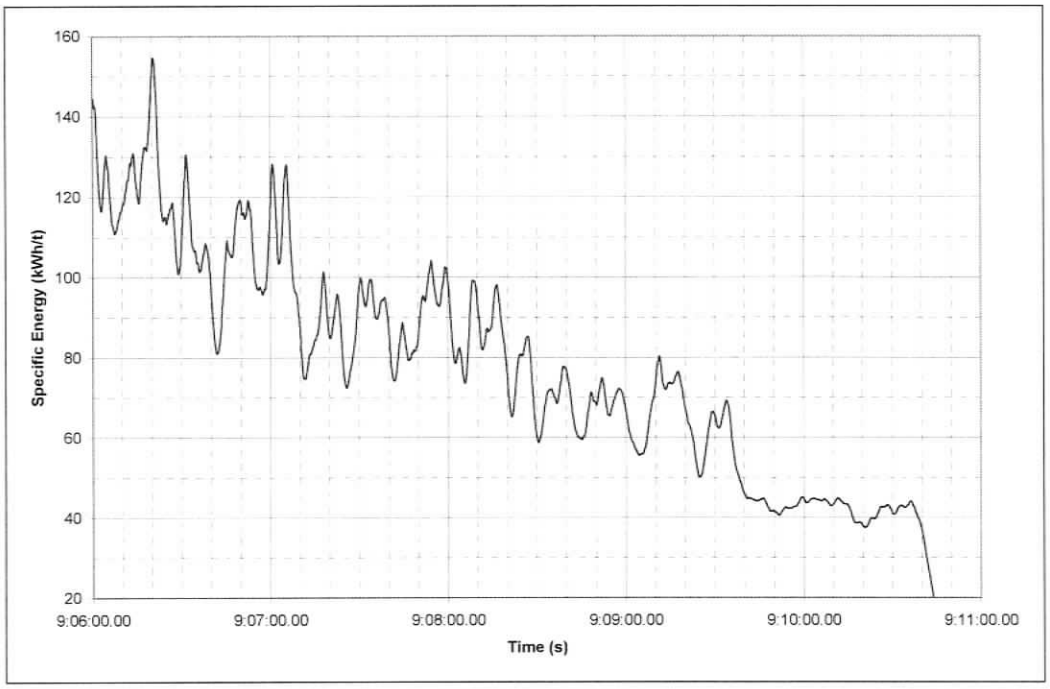

Figure A-3, Specific energy (Experiment S9)

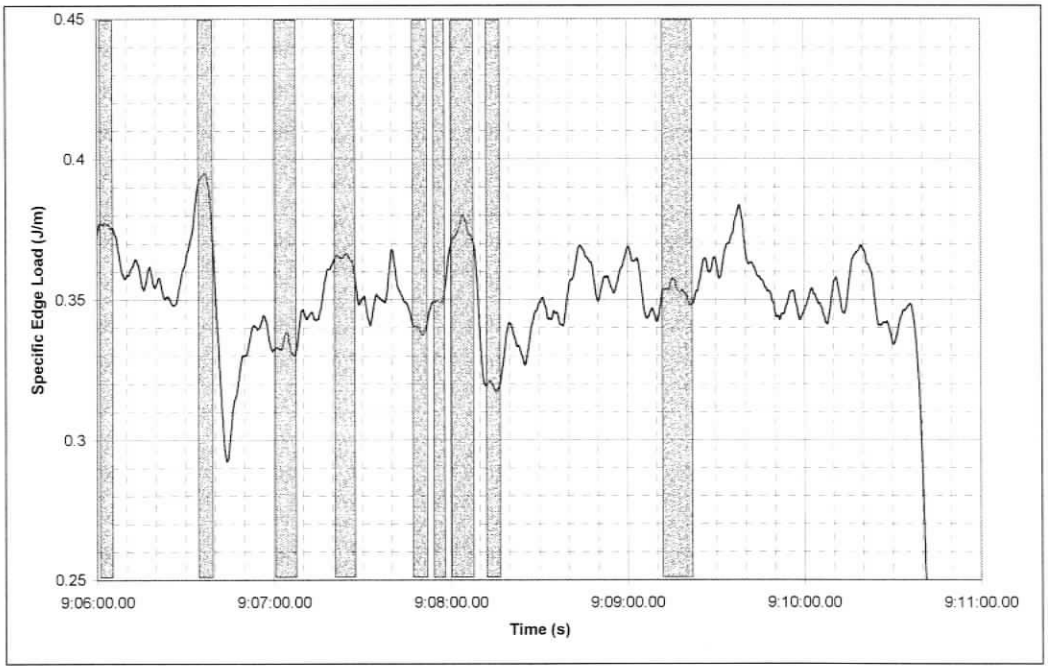

Figure A-4, Specific edge load (Experiment S9)

A.2. Experiment S9B1

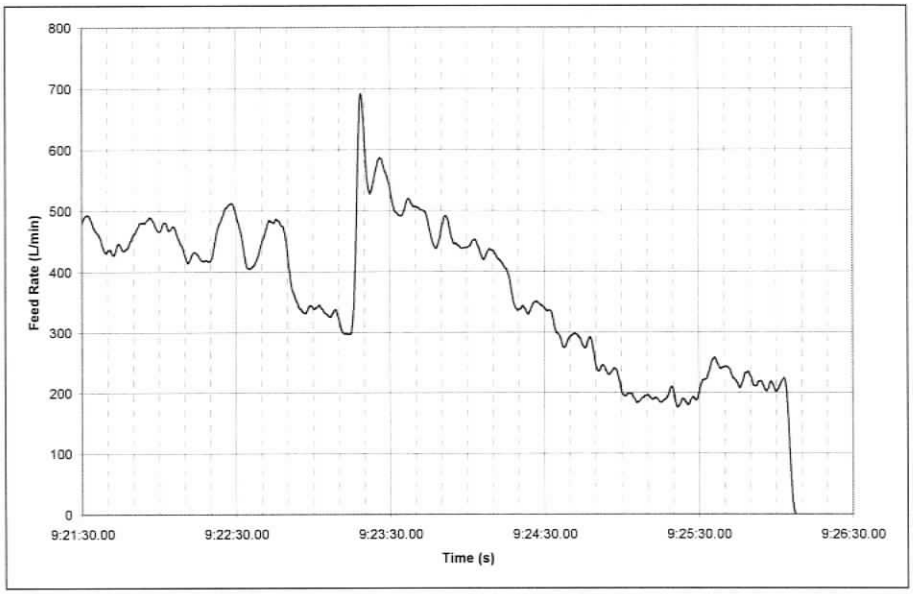

Figure A-5, Feed Rate (Experiment S9B1)

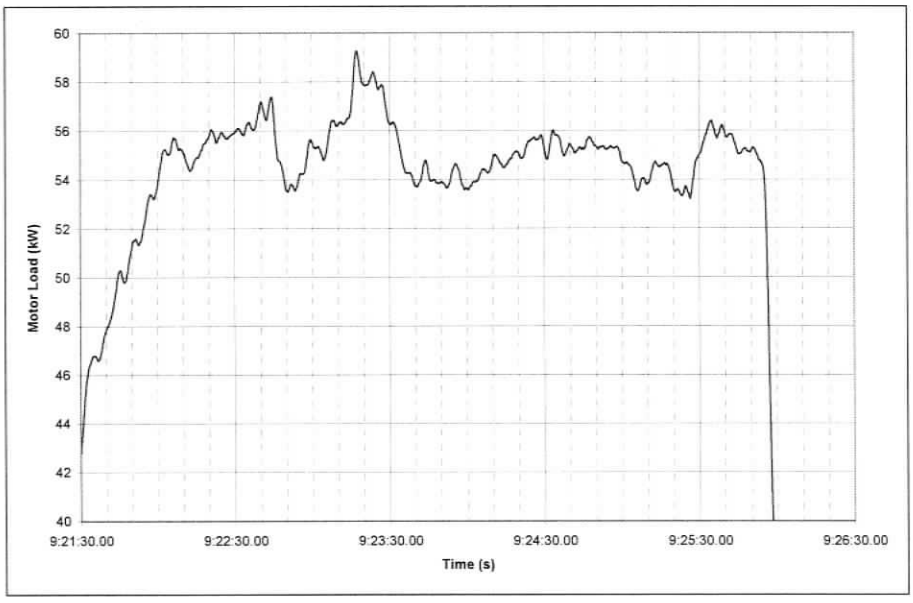

Figure A-6, Motor Load (Experiment S9B1)

Table A-2, Calculated Sample Conditions (Experiment S9B1)

	S9B1						BOF:	9:16:29 AM	
	Specific Energy			SEL			Time		
	Low	High	Avg	Low	High	Avg	Begin	End	[s]
S9B1 1	44	57	50.5	0.465	0.470	0.468	9:22:50 AM	9:22:55 AM	5
S9B1 2	58	58	58.0	0.487	0.491	0.489	9:22:59 AM	9:23:03 AM	4
S9B1 3	41	48	44.5	0.490	0.496	0.493	9:22:20 AM	9:22:30 AM	10
S9B1 4	61	69	65.0	0.500	0.501	0.501	9:23:08 AM	9:23:14 AM	6
S9B1 5	34	40	37.0	0.520	0.521	0.521	9:23:20 AM	9:23:22 AM	2
S9B1 6	39	42	40.5	0.467	0.470	0.469	9:23:46 AM	9:23:54 AM	8
S9B1 7	81	90	85.5	0.486	0.487	0.487	9:24:50 AM	9:24:59 AM	9
S9B1 8	100	102	101.0	0.476	0.480	0.478	9:25:13 AM	9:25:18 AM	5
S9B1 9	100	107	103.5	0.461	0.465	0.463	9:25:21 AM	9:25:27 AM	6

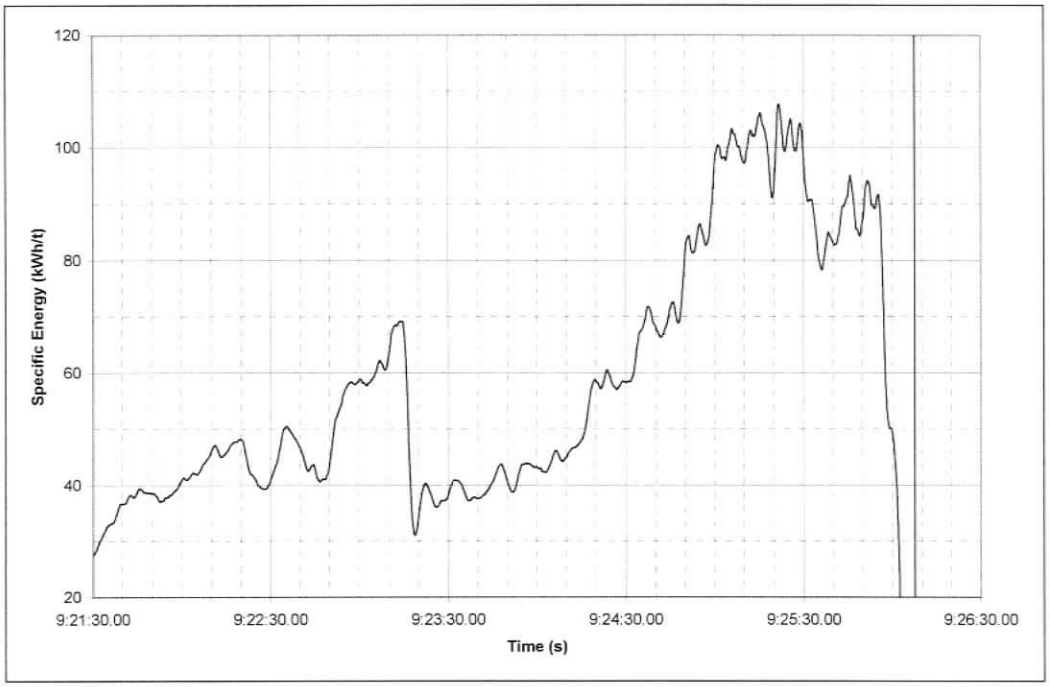

Figure A-7, Specific energy (Experiment S9B1)

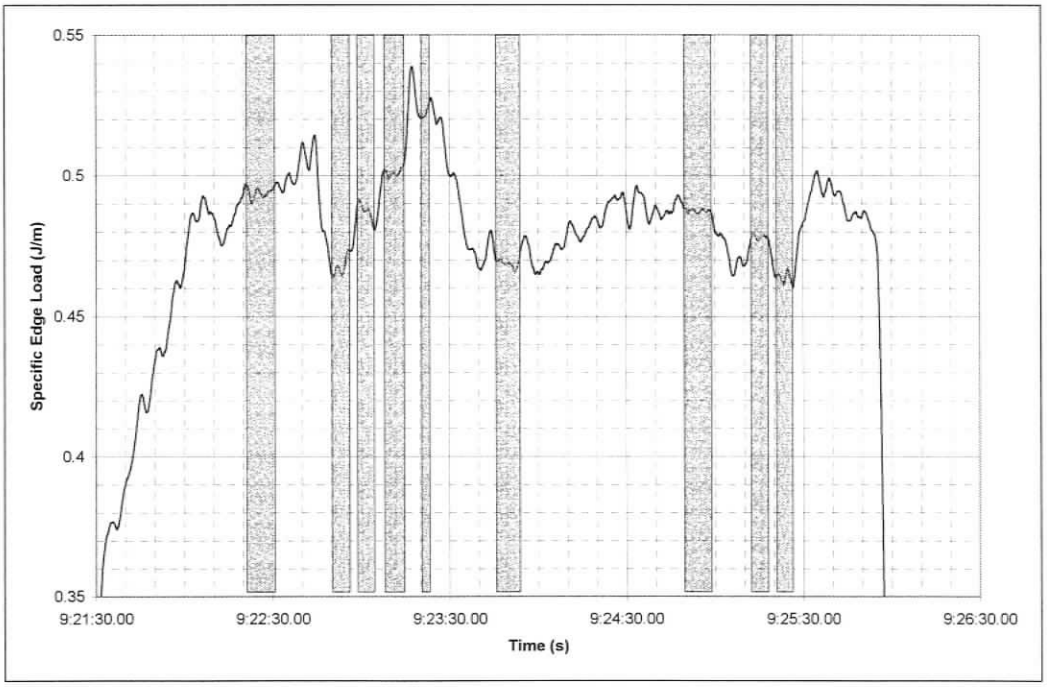

Figure A-8, Specific edge load (Experiment S9B1)

A.3. Experiment S9B2

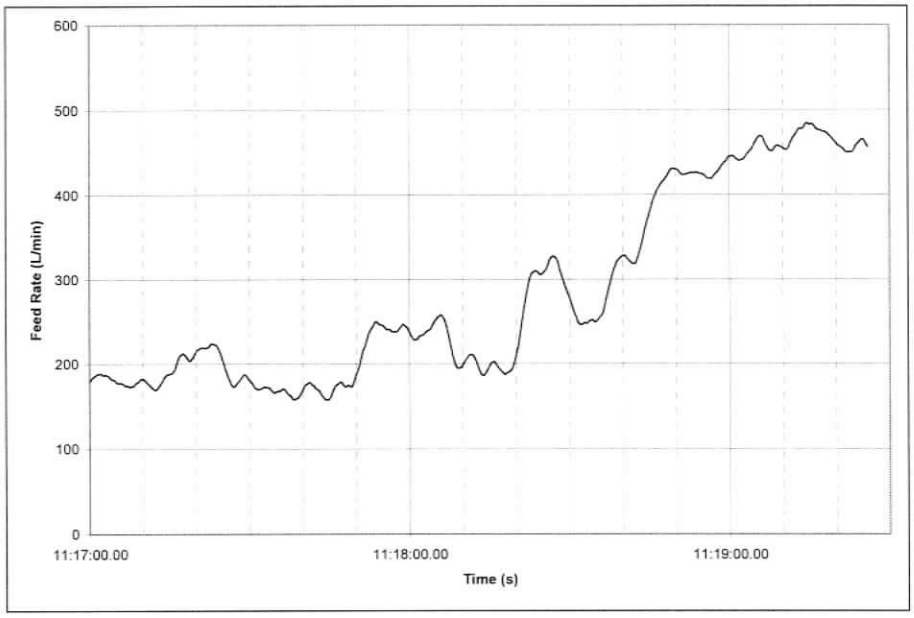

Figure A-9, Feed Rate (Experiment S9B1)

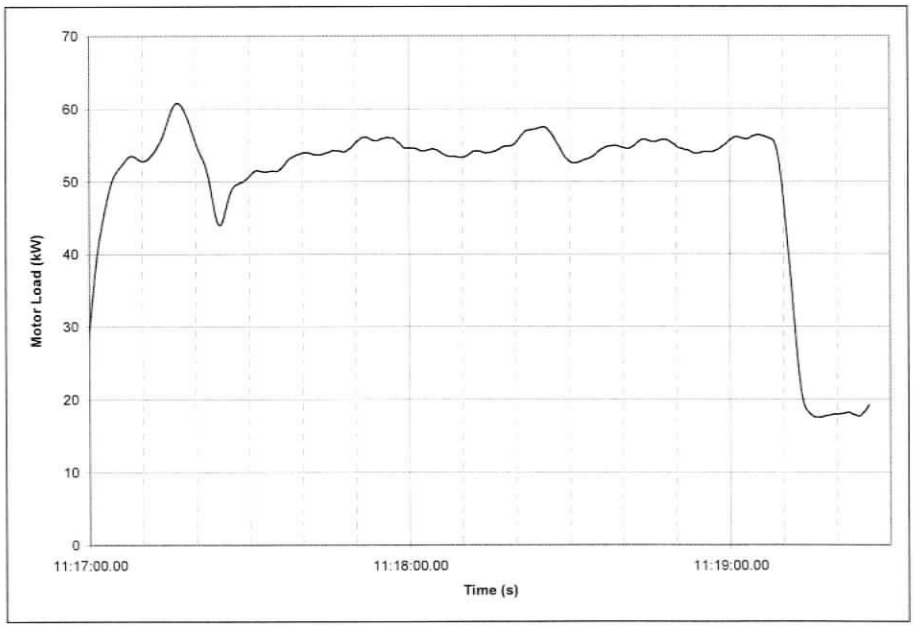

Figure A-10, Motor Load (Experiment S9B1)

Table A-3, Calculated Sample Conditions (Experiment S9B2)

	S9B2						BOF:	11:15:16 AM	
	Specific Energy			SEL			Time		
	Low	High	Avg	Low	High	Avg	Begin	End	[s]
S9B2 1	102	110	106.0	0.455	0.469	0.462	11:17:07 AM	11:17:12 AM	5
S9B2 2	105	118	111.5	0.533	0.557	0.545	11:17:15 AM	11:17:18 AM	3
S9B2 3	64	70	67.0	0.342	0.347	0.345	11:17:24 AM	11:17:25 AM	1
S9B2 4	104	107	105.5	0.436	0.442	0.439	11:17:31 AM	11:17:36 AM	5
S9B2 5	108	121	114.5	0.466	0.473	0.470	11:17:40 AM	11:17:48 AM	8
S9B2 6	78	102	90.0	0.465	0.472	0.469	11:18:07 AM	11:18:16 AM	9
S9B2 7	61	73	67.0	0.509	0.515	0.512	11:18:22 AM	11:18:26 AM	4
S9B2 8	46	60	53.0	0.489	0.493	0.491	11:18:43 AM	11:18:49 AM	6
S9B2 9	44	46	45.0	0.494	0.502	0.498	11:19:00 AM	11:19:08 AM	8

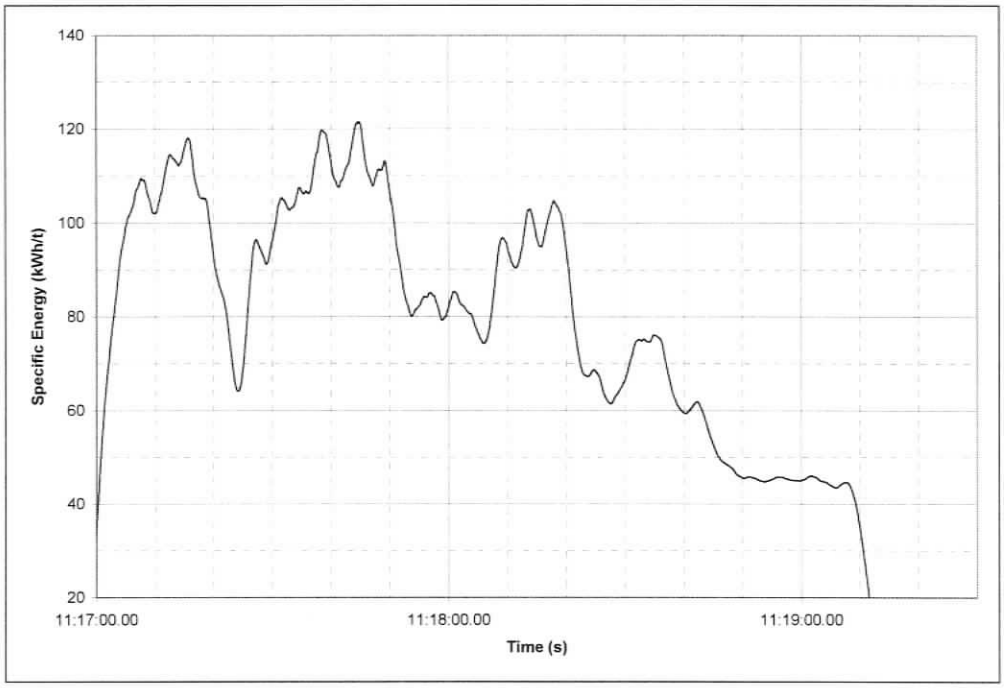

Figure A-11, Specific energy (Experiment S9B2)

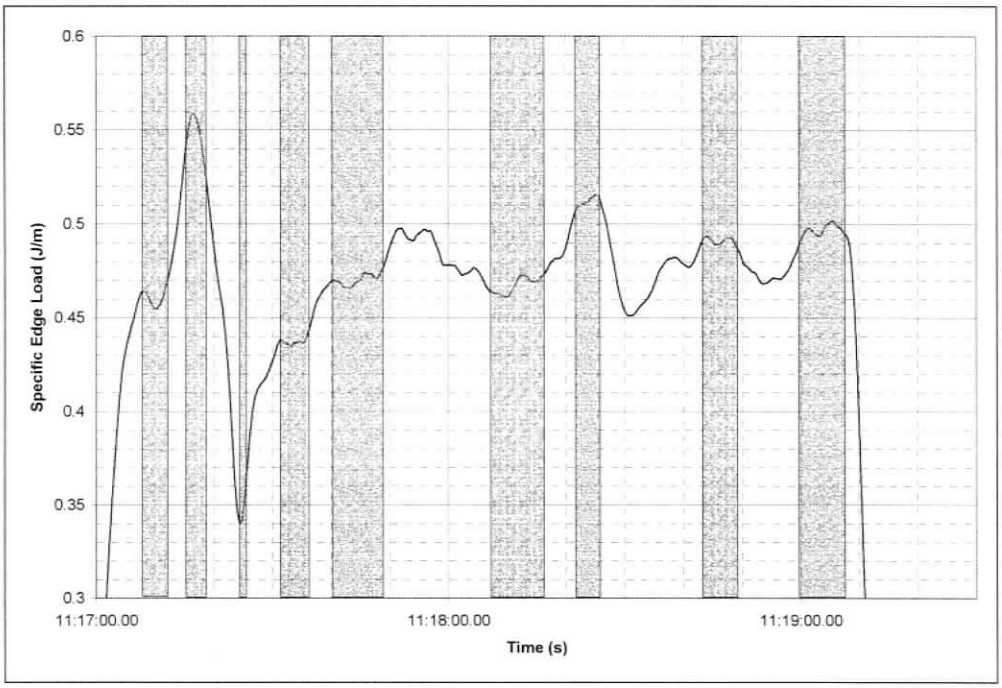

Figure A-12, Specific edge load (Experiment S9B2)

A.4. Experiment S12

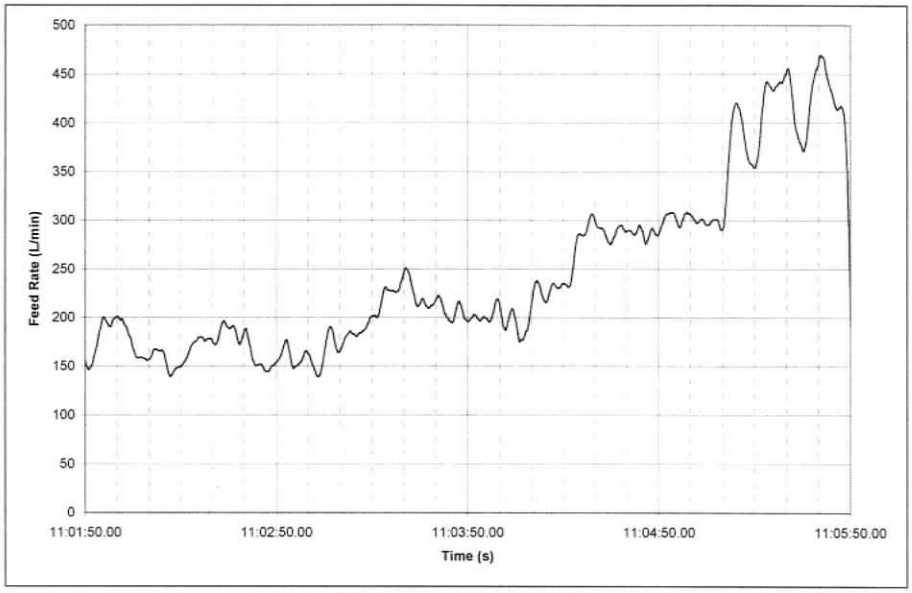

Figure A-13, Feed Rate (Experiment S9B2)

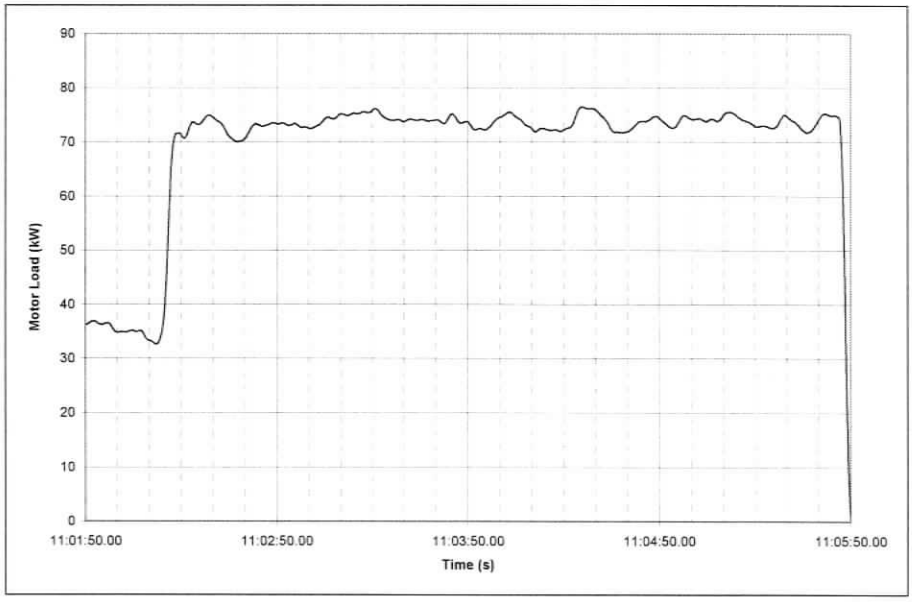

Figure A-14, Motor Load (Experiment S9B2)

Table A-4, Calculated Sample Conditions (Experiment S12)

	S12						BOF:	11:00:50 AM	
	Specific Energy			SEL			Time		
	Low	High	Avg	Low	High	Avg	Begin	End	[s]
S12 1	114	138	126.0	0.365	0.371	0.368	11:02:45 AM	11:02:55 AM	10
S12 2	85	96	90.5	0.375	0.378	0.377	11:03:32 AM	11:03:41 AM	9
S12 3	106	116	111.0	0.386	0.394	0.390	11:03:13 AM	11:03:20 AM	7
S12 4	98	106	102.0	0.338	0.343	0.341	11:02:36 AM	11:02:40 AM	4
S12 5	65	68	66.5	0.354	0.356	0.355	11:04:36 AM	11:04:40 AM	4
S12 6	71	76	73.5	0.395	0.400	0.398	11:04:25 AM	11:04:30 AM	5
S12 7	45	54	49.5	0.362	0.366	0.364	11:05:21 AM	11:05:27 AM	6
S12 8	84	90	87.0	0.358	0.361	0.360	11:04:13 AM	11:04:20 AM	7
S12 9	46	50	48.0	0.383	0.387	0.385	11:05:42 AM	11:05:46 AM	4

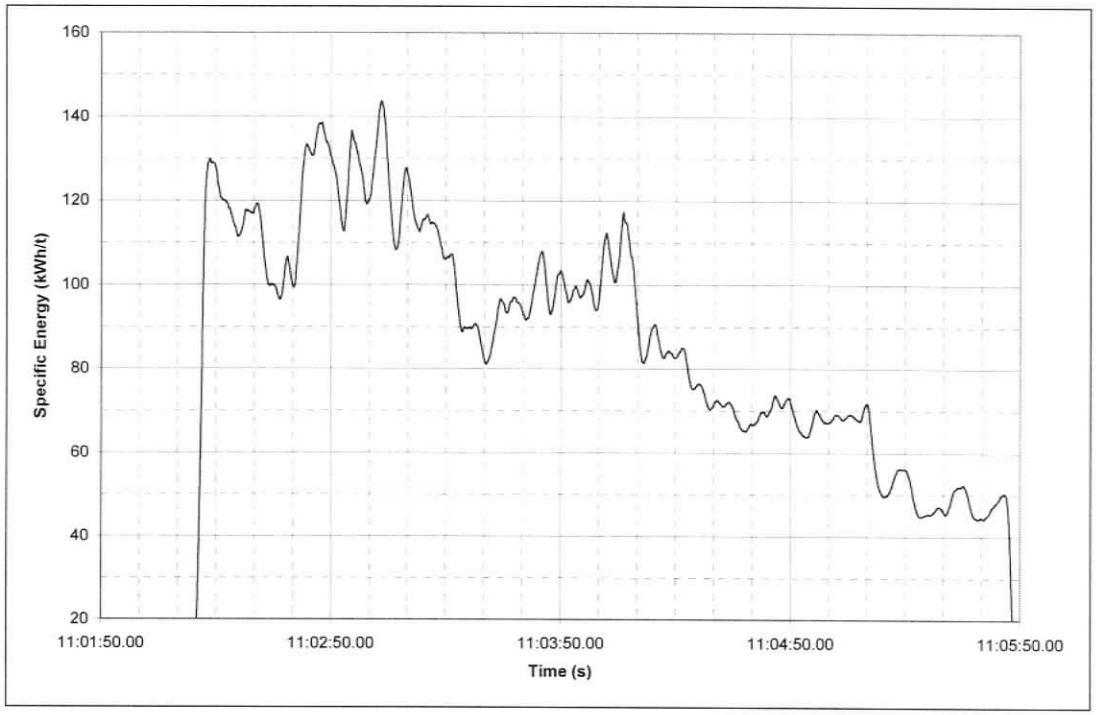

Figure A-15, Specific energy (Experiment S12)

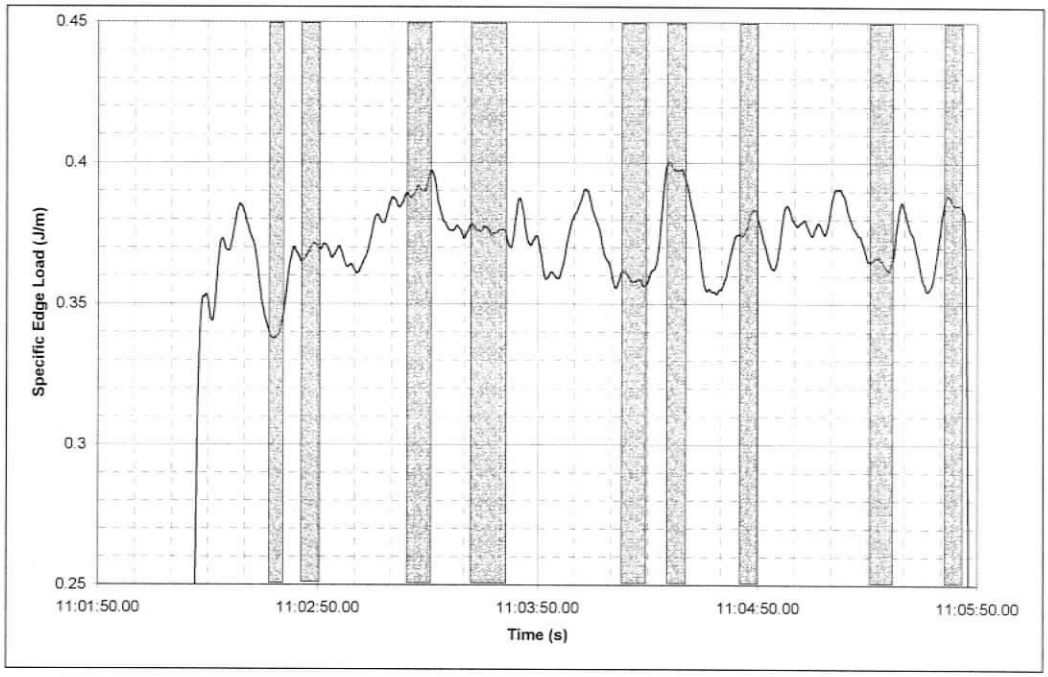

Figure A-16, Specific edge load (Experiment S12)

APPENDIX B – EVENT CLASSIFICATION AND BAR IDENTIFICATION LOGIC FLOW CHARTS

B.1. Event Classification Logic

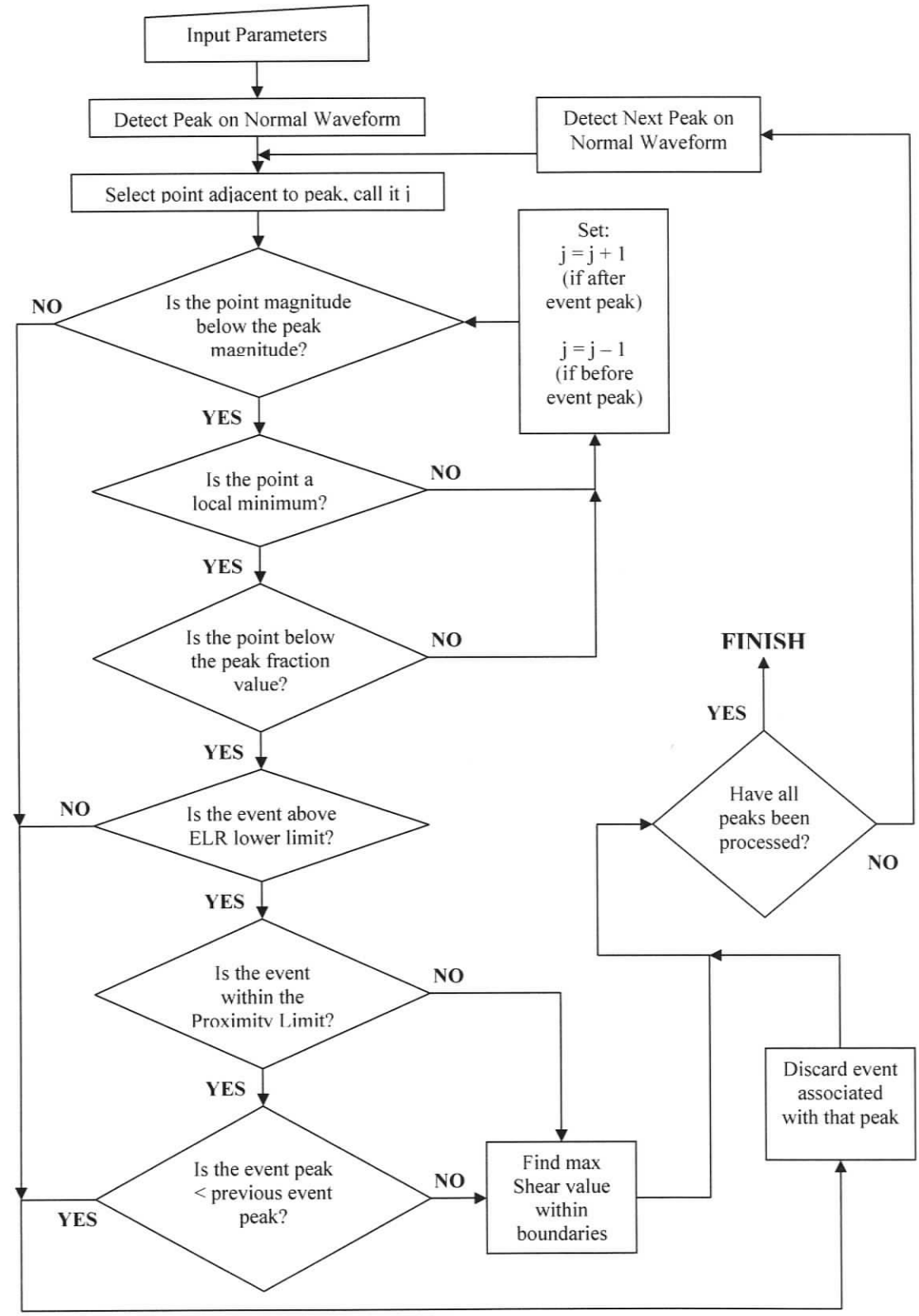

Figure B-1, Event Classifier Logic Flow Chart

B.2. Bar Identification Logic

B.2.1. Bar Identification Main Routine

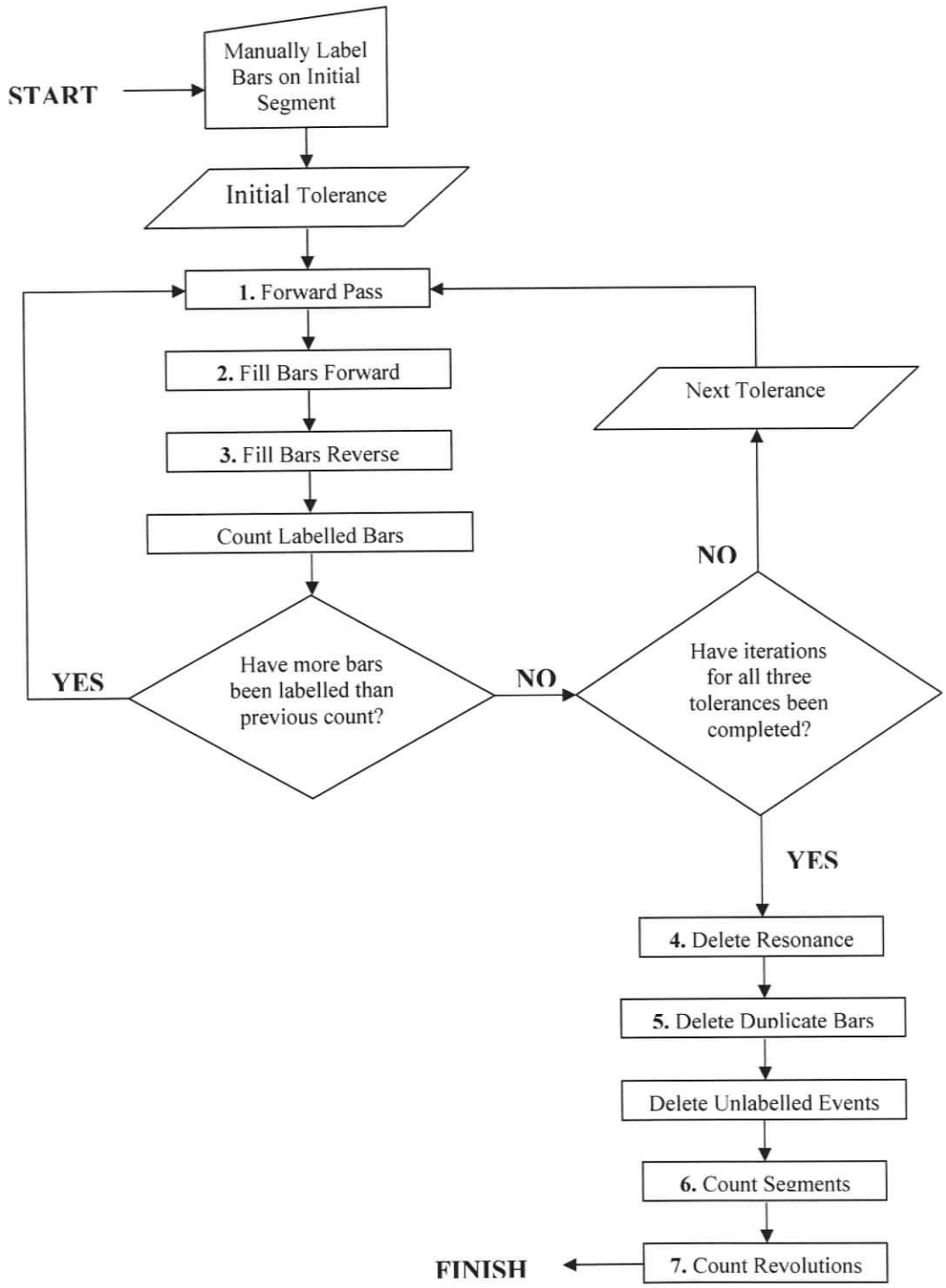

Figure B-2, Bar Identification Main Procedure Logic Flow Chart

Table B-1, Bar-Labelling Tolerances for Bar-Passing and Segment-Passing periods

Experiment S12			
	Tolerance #1	Tolerance #2	Tolerance #3
Minimum Bar-Passing Period (ms)	0.33	0.33	0.3
Maximum Bar-Passing Period (ms)	0.42	0.42	0.45
Minimum Segment-Passing Period (ms)	7.1	7.08	7.05
Maximum Segment-Passing Period (ms)	7.25	7.28	7.31

Experiment S9, S9B1, S9B2			
	Tolerance #1	Tolerance #2	Tolerance #3
Minimum Bar-Passing Period (ms)	0.44	0.44	0.4
Maximum Bar-Passing Period (ms)	0.56	0.56	0.6
Minimum Segment-Passing Period (ms)	9.47	9.44	9.4
Maximum Segment-Passing Period (ms)	9.67	9.7	9.74

B.2.2. "Forward Pass" Subroutine

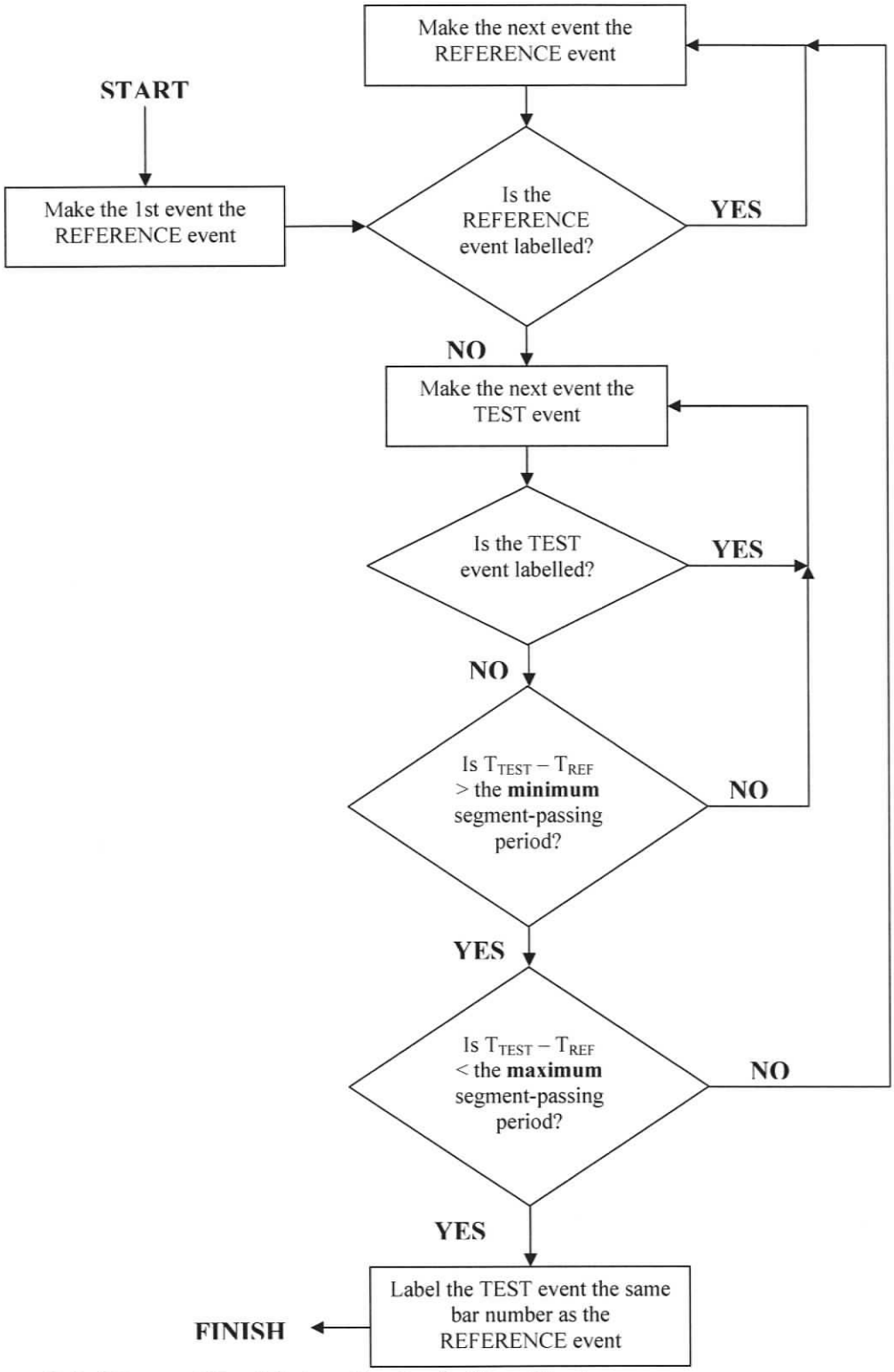

Figure B-3, "Forward Pass" Subroutine Logic Flow Chart

B.2.3. "Fill Bars Forward" Subroutine

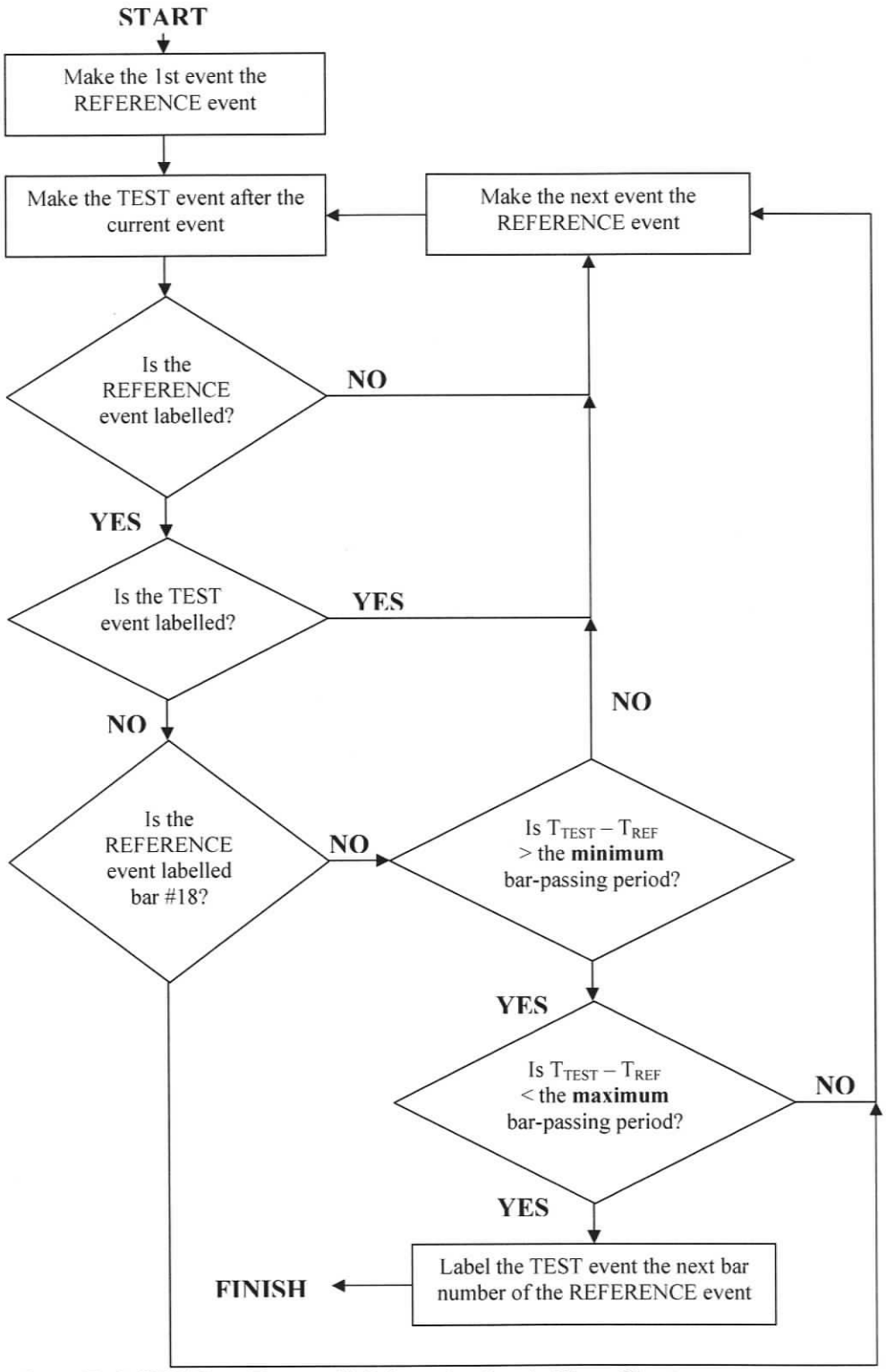

Figure B-4, "Fill Bars Forward" Subroutine Logic Flow Chart

B.2.4. "Fill Bars Reverse" Subroutine

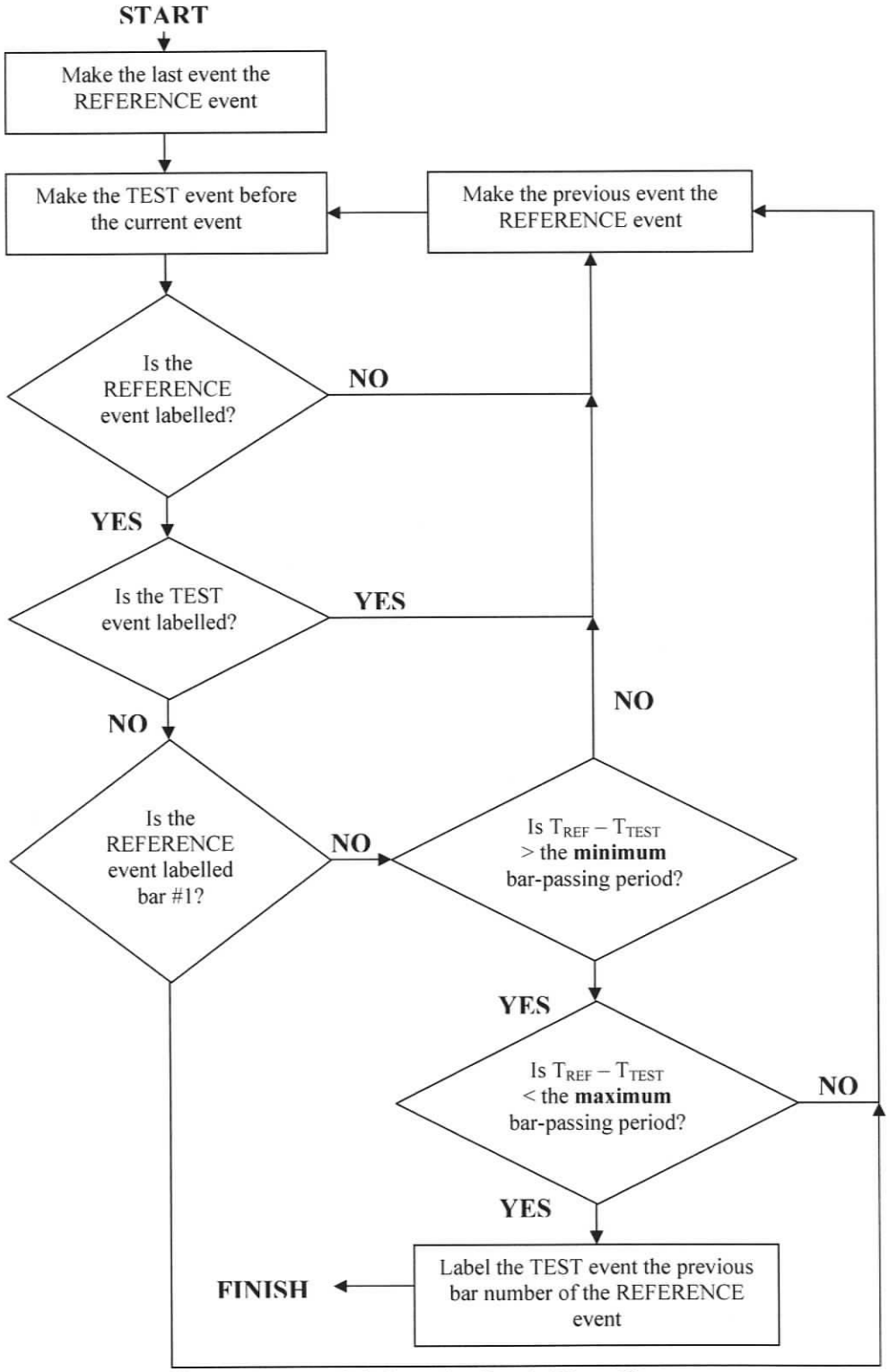

Figure B-5, "Fill Bars Reverse" Subroutine Logic Flow Chart

B.2.5. "Delete Resonance" Subroutine

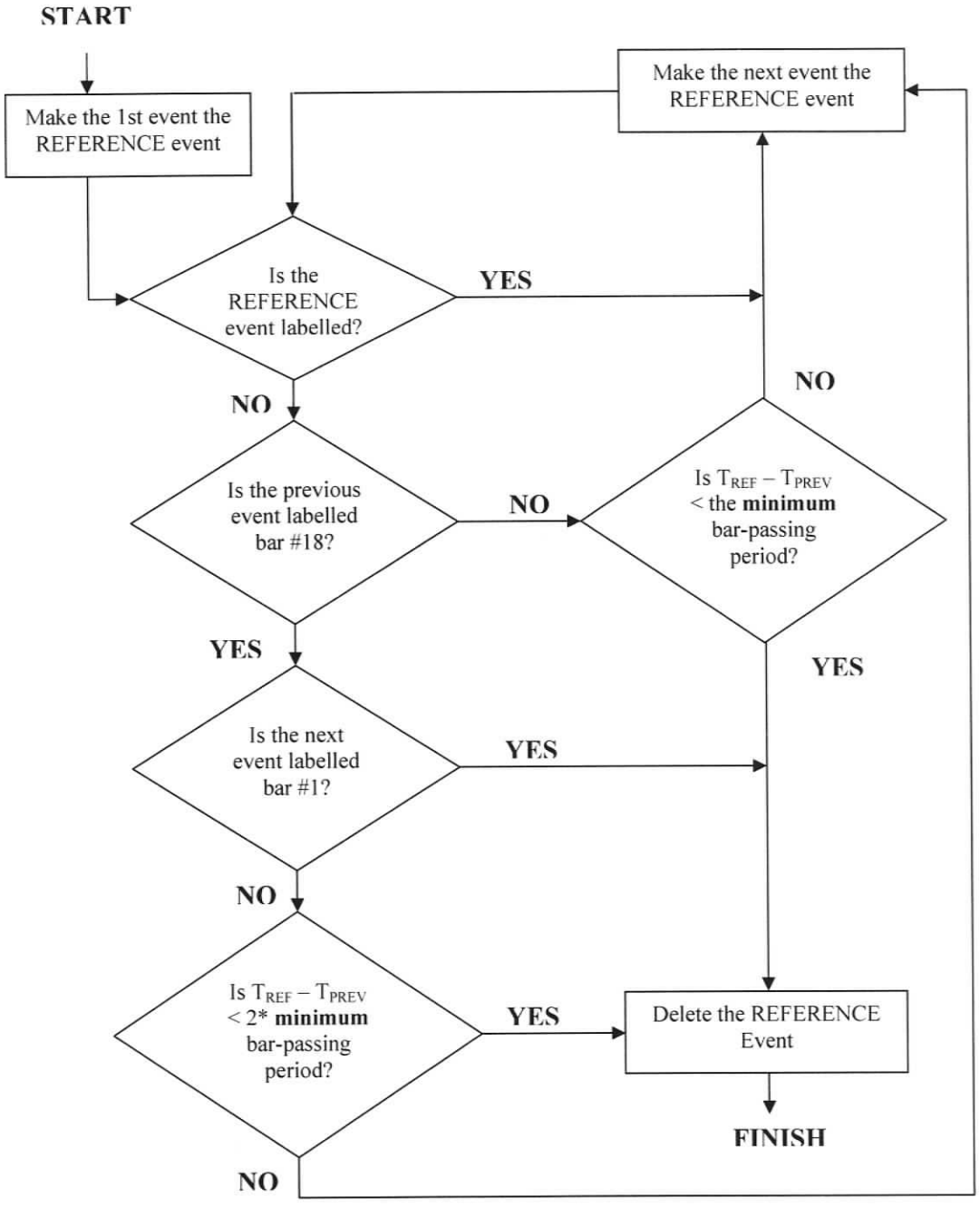

Figure B-6, "Delete Resonance" Subroutine Logic Flow Chart

B.2.6. "Delete Duplicates" Subroutine

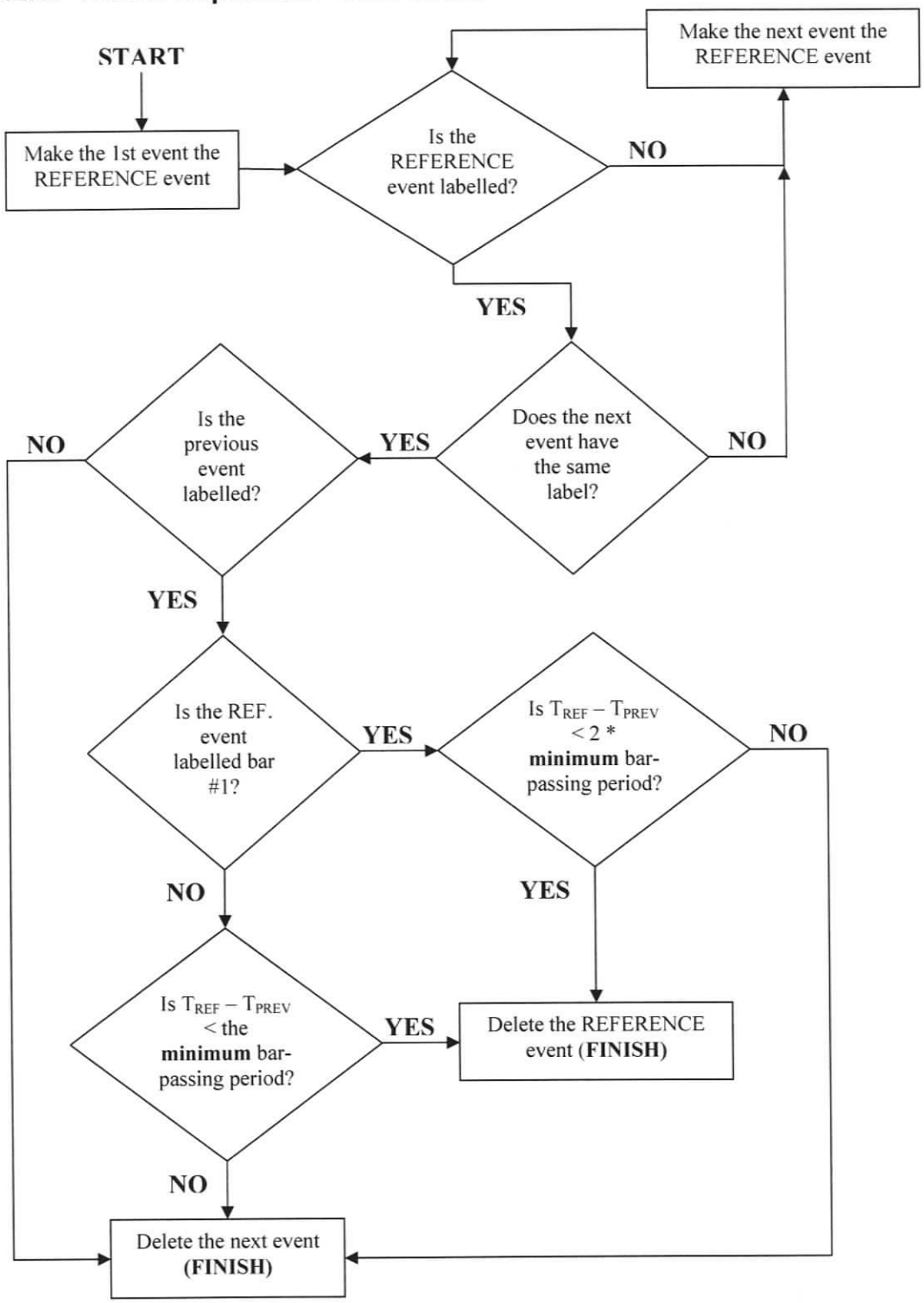

Figure B-7, "Delete Duplicates" Subroutine Logic Flow Chart

B.2.7. Count Segments

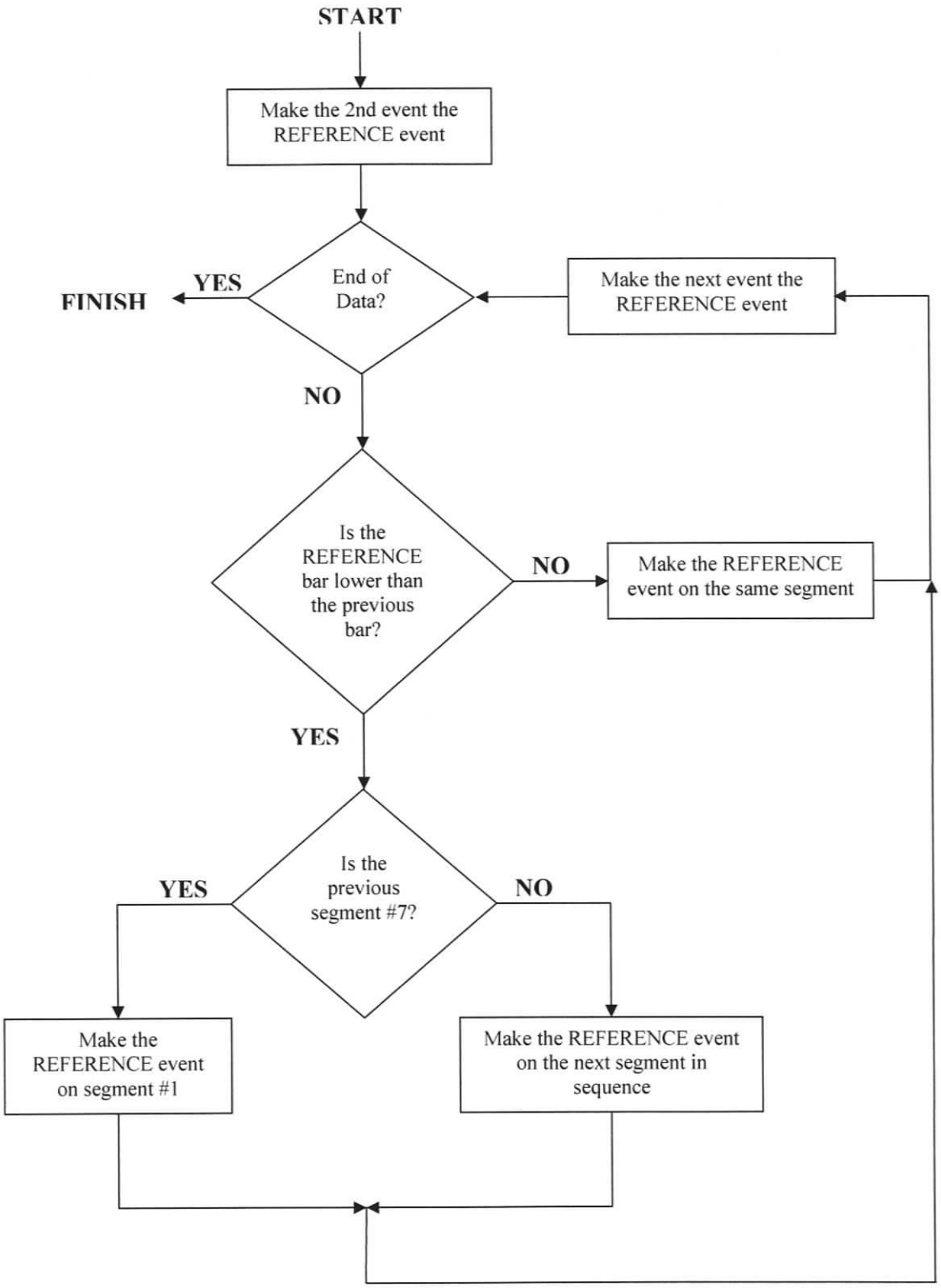

Figure B-8, "Count Segments" Subroutine Logic Flow Chart

B.2.8. Count Revolutions

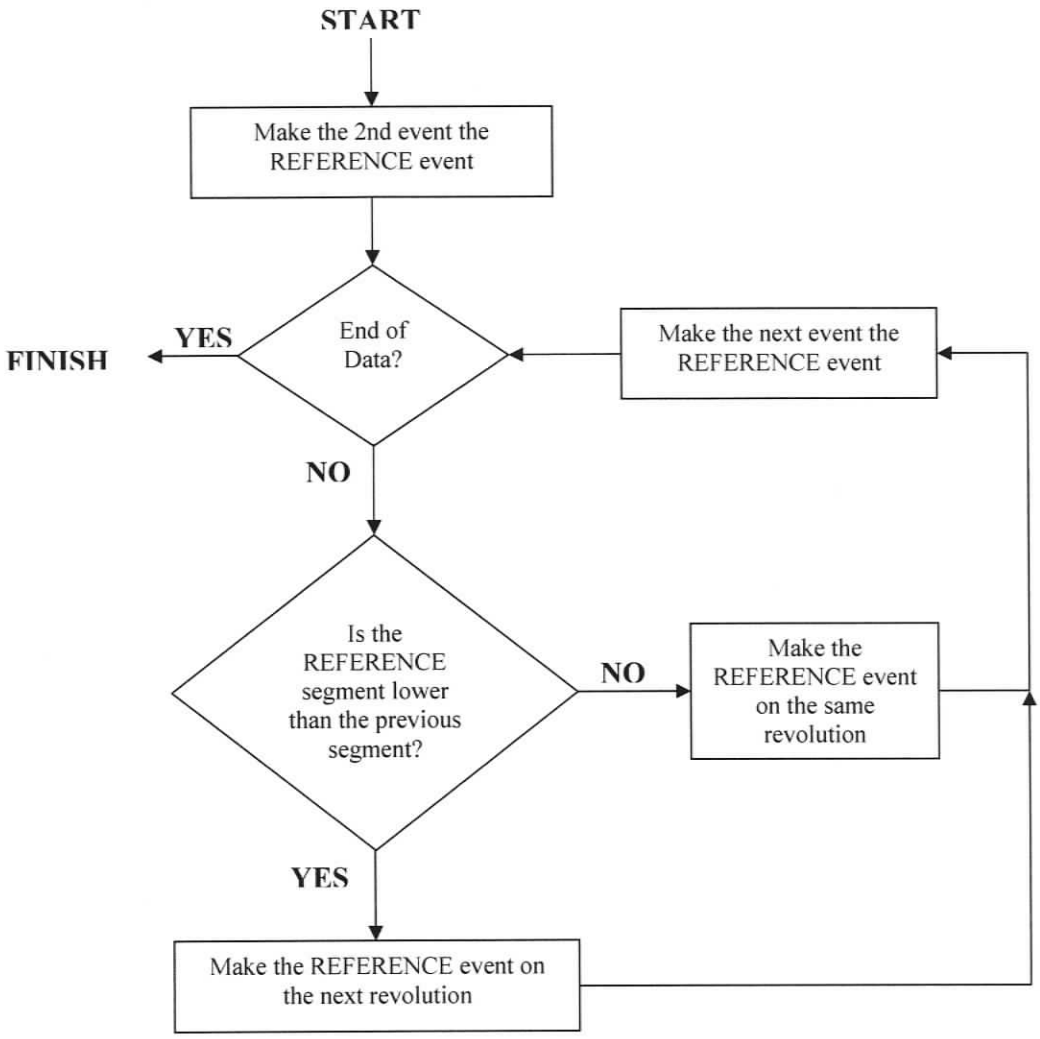

Figure B-9, "Count Revolutions" Subroutine Logic Flow Chart

APPENDIX C –WEIBULL FORCE DISTRIBUTIONS AND MEDIAN VALUES

C.1. Refiner Level

Table C-1, Normal and Shear Force Weibull Parameters (Refiner Level)

	Normal Force				Shear Force			
Experiment	β	η	R^2	Median	β	η	R^2	Median
S9 1	2.03	3.39	0.96	2.83	2.45	0.52	0.96	0.45
S9 2	1.97	4.45	0.97	3.70	2.34	0.66	0.96	0.56
S9 3	1.93	3.59	0.96	2.97	2.33	0.55	0.97	0.47
S9 4	2.15	4.81	0.98	4.06	2.63	0.69	0.98	0.60
S9 5	2.13	4.12	0.98	3.47	2.55	0.61	0.96	0.53
S9 6	2.11	4.32	0.97	3.63	2.63	0.63	0.97	0.55
S9 7	2.19	5.05	0.97	4.27	2.70	0.72	0.97	0.63
S9 8	2.18	3.90	0.98	3.30	2.60	0.58	0.97	0.51
S9 9	2.07	4.71	0.97	3.95	2.57	0.68	0.97	0.59
S9B1 1	1.92	5.92	0.98	4.89	2.35	0.83	0.97	0.71
S9B1 2	1.97	6.39	0.98	5.30	2.43	0.88	0.98	0.76
S9B1 3	1.87	6.66	0.98	5.47	2.37	0.91	0.98	0.78
S9B1 4	2.06	6.32	0.98	5.29	2.59	0.88	0.98	0.76
S9B1 5	1.92	6.79	0.98	5.61	2.39	0.93	0.99	0.80
S9B1 6	1.84	6.42	0.98	5.26	2.28	0.89	0.98	0.75
S9B1 7	1.98	6.81	0.99	5.66	2.44	0.92	0.98	0.79
S9B1 8	1.95	6.50	0.99	5.39	2.40	0.88	0.98	0.76
S9B1 9	1.97	6.72	0.98	5.58	2.38	0.90	0.98	0.77
S9B2 1	2.14	5.32	0.98	4.49	2.62	0.74	0.97	0.65
S9B2 2	2.51	6.69	0.99	5.78	3.11	0.89	0.99	0.79
S9B2 3	2.09	3.70	0.96	3.10	2.47	0.55	0.94	0.48
S9B2 4	2.08	4.53	0.97	3.80	2.56	0.65	0.97	0.56
S9B2 5	2.16	4.77	0.97	4.03	2.66	0.67	0.97	0.59
S9B2 6	2.29	5.55	0.98	4.73	2.84	0.76	0.98	0.67
S9B2 7	2.28	6.47	0.96	5.51	2.84	0.87	0.95	0.77
S9B2 8	2.19	6.40	0.98	5.41	2.73	0.87	0.98	0.76
S9B2 9	2.18	6.56	0.98	5.54	2.74	0.89	0.98	0.78
S12 1	2.06	4.53	0.97	3.79	2.34	0.70	0.95	0.60
S12 2	2.11	4.95	0.97	4.16	2.47	0.75	0.95	0.65
S12 3	2.13	4.93	0.95	4.15	2.57	0.75	0.95	0.65
S12 4	2.08	4.34	0.97	3.64	2.36	0.68	0.94	0.59
S12 5	2.02	5.21	0.96	4.35	2.49	0.79	0.96	0.68
S12 6	2.12	5.80	0.96	4.88	2.58	0.86	0.94	0.74
S12 7	2.05	5.96	0.98	4.98	2.44	0.87	0.95	0.75
S12 8	2.10	4.93	0.96	4.14	2.49	0.75	0.95	0.65
S12 9	2.08	6.35	0.98	5.32	2.60	0.92	0.97	0.80

C.2. Segment Level

C.2.1. Experiment S9

Table C-2, Normal and Shear Force Weibull Parameters (Experiment S9, Segments)

Sample & Plate Segment		Normal Force				Shear Force			
		β	η	R^2	Median	β	η	R^2	Median
S9 1	1	2.44	2.40	0.97	2.07	2.61	0.42	0.93	0.36
S9 1	2	2.41	2.73	0.95	2.35	2.99	0.45	0.95	0.39
S9 1	3	2.31	3.73	0.98	3.18	2.68	0.57	0.98	0.49
S9 1	4	2.66	6.16	0.97	5.37	3.24	0.84	0.98	0.75
S9 1	5	2.38	3.18	0.98	2.73	2.73	0.49	0.99	0.43
S9 1	6	2.33	3.06	0.91	2.61	2.75	0.48	0.93	0.42
S9 1	7	1.91	2.60	0.90	2.15	2.55	0.42	0.97	0.37
S9 2	1	2.06	3.18	0.96	2.66	2.63	0.52	0.97	0.45
S9 2	2	2.64	3.95	0.98	3.44	2.84	0.60	0.93	0.52
S9 2	3	2.45	5.37	0.99	4.63	2.60	0.76	0.93	0.66
S9 2	4	2.97	7.64	0.97	6.75	3.61	1.01	0.98	0.92
S9 2	5	1.80	3.95	0.91	3.22	2.20	0.58	0.92	0.49
S9 2	6	2.05	3.75	0.92	3.14	2.64	0.57	0.97	0.49
S9 2	7	2.23	3.30	0.98	2.80	2.62	0.52	0.98	0.45
S9 3	1	1.96	2.46	0.91	2.04	2.36	0.42	0.94	0.36
S9 3	2	2.58	2.90	0.99	2.52	3.00	0.46	0.99	0.41
S9 3	3	2.27	4.29	0.97	3.65	2.64	0.63	0.96	0.55
S9 3	4	2.92	6.82	0.97	6.01	3.61	0.91	1.00	0.82
S9 3	5	2.02	3.37	0.95	2.81	2.42	0.51	0.95	0.44
S9 3	6	2.22	2.96	0.94	2.51	2.67	0.46	0.94	0.40
S9 3	7	2.32	2.50	0.95	2.14	2.84	0.41	0.99	0.36
S9 4	1	2.14	3.55	0.98	2.99	2.74	0.56	0.99	0.49
S9 4	2	2.45	4.35	0.98	3.74	2.96	0.64	0.95	0.57
S9 4	3	2.45	5.71	0.99	4.92	2.85	0.80	0.96	0.70
S9 4	4	3.29	7.79	1.00	6.97	4.00	1.01	0.99	0.92
S9 4	5	2.35	4.27	0.99	3.65	2.79	0.63	0.99	0.55
S9 4	6	2.53	4.14	0.98	3.58	2.94	0.61	0.96	0.54
S9 4	7	2.17	3.82	0.95	3.23	2.71	0.58	0.97	0.51

Sample & Plate Segment		Normal Force				Shear Force			
		β	η	R^2	Median	β	η	R^2	Median
S9 5	1	1.97	3.30	0.95	2.74	2.43	0.53	0.93	0.46
S9 5	2	2.72	3.77	0.98	3.30	3.29	0.57	0.97	0.51
S9 5	3	2.25	4.48	0.97	3.81	2.62	0.65	0.95	0.57
S9 5	4	2.62	6.46	0.97	5.61	3.29	0.87	0.99	0.77
S9 5	5	2.11	3.59	0.97	3.02	2.46	0.54	0.96	0.47
S9 5	6	2.49	3.78	0.98	3.26	2.83	0.57	0.96	0.50
S9 5	7	2.28	3.52	1.00	3.00	2.51	0.54	0.97	0.47
S9 6	1	2.07	3.45	0.99	2.89	2.40	0.55	0.93	0.47
S9 6	2	2.12	3.98	0.89	3.35	3.02	0.59	0.97	0.52
S9 6	3	2.27	4.65	0.96	3.95	2.97	0.67	0.99	0.59
S9 6	4	2.80	6.42	0.96	5.63	3.57	0.86	0.99	0.78
S9 6	5	2.15	3.64	0.94	3.07	2.85	0.54	0.98	0.48
S9 6	6	2.49	4.08	0.99	3.52	2.87	0.60	0.97	0.53
S9 6	7	1.94	3.91	0.93	3.24	2.35	0.59	0.92	0.50
S9 7	1	1.95	4.27	0.96	3.54	2.51	0.65	0.96	0.56
S9 7	2	2.39	4.89	0.94	4.19	3.14	0.70	0.98	0.62
S9 7	3	2.23	5.38	0.95	4.56	2.75	0.75	0.97	0.66
S9 7	4	2.68	7.33	0.97	6.40	3.39	0.96	0.99	0.86
S9 7	5	2.35	4.13	0.96	3.53	2.83	0.60	0.95	0.53
S9 7	6	2.40	4.65	0.97	3.99	2.82	0.67	0.96	0.59
S9 7	7	2.28	4.66	0.99	3.97	2.68	0.68	0.98	0.59
S9 8	1	2.03	3.48	0.99	2.91	2.54	0.55	0.99	0.47
S9 8	2	2.59	3.72	0.97	3.23	3.00	0.56	0.94	0.50
S9 8	3	2.41	4.21	0.99	3.62	2.80	0.62	0.99	0.54
S9 8	4	2.68	5.50	0.98	4.80	3.10	0.76	0.94	0.67
S9 8	5	1.98	3.02	0.95	2.51	2.36	0.47	0.93	0.40
S9 8	6	2.31	3.61	0.98	3.08	2.68	0.55	0.99	0.48
S9 8	7	2.29	3.69	0.97	3.15	2.75	0.56	0.97	0.49
S9 9	1	1.87	4.00	0.95	3.28	2.30	0.62	0.94	0.53
S9 9	2	2.20	4.54	0.95	3.84	2.88	0.66	0.96	0.58
S9 9	3	2.36	5.11	0.98	4.38	2.86	0.73	0.98	0.64
S9 9	4	2.53	7.30	0.97	6.31	3.18	0.94	0.96	0.84
S9 9	5	2.15	3.78	0.96	3.18	2.75	0.56	0.99	0.49
S9 9	6	2.34	4.21	0.97	3.60	2.76	0.62	0.96	0.54
S9 9	7	2.23	4.12	0.97	3.50	2.64	0.62	0.95	0.54

C.2.2. Experiment S9B1

Table C-3, Normal and Shear Force Weibull Parameters (Exper. S9B1, Segments)

Sample & Plate Segment		Normal Force				Shear Force			
		β	η	R^2	Median	β	η	R^2	Median
S9B1 1	1	1.98	3.89	0.97	3.23	2.36	0.61	0.91	0.52
S9B1 1	2	2.71	5.58	0.98	4.87	3.32	0.79	0.98	0.71
S9B1 1	3	2.83	7.95	0.96	6.99	3.43	1.05	0.97	0.95
S9B1 1	4	3.48	10.19	0.94	9.17	4.67	1.27	0.98	1.18
S9B1 1	5	1.94	5.15	0.97	4.27	2.48	0.73	0.98	0.63
S9B1 1	6	2.12	4.36	0.97	3.67	2.64	0.65	0.96	0.56
S9B1 1	7	2.23	4.02	0.97	3.41	2.49	0.62	0.92	0.53
S9B1 2	1	2.12	4.33	0.98	3.64	2.74	0.66	0.99	0.58
S9B1 2	2	2.32	6.11	0.94	5.22	2.90	0.85	0.94	0.75
S9B1 2	3	3.25	8.46	1.00	7.56	3.91	1.11	1.00	1.01
S9B1 2	4	4.05	10.73	0.99	9.81	4.90	1.34	0.99	1.24
S9B1 2	5	2.08	5.57	0.96	4.67	2.69	0.77	1.00	0.67
S9B1 2	6	2.38	4.74	0.99	4.07	2.97	0.69	0.99	0.61
S9B1 2	7	2.12	4.41	0.95	3.71	2.50	0.65	0.91	0.57
S9B1 3	1	2.05	4.07	0.98	3.40	2.60	0.64	0.99	0.56
S9B1 3	2	2.57	6.53	0.98	5.66	3.14	0.89	0.96	0.79
S9B1 3	3	2.64	9.30	0.96	8.10	3.36	1.18	0.98	1.06
S9B1 3	4	3.63	11.87	1.00	10.73	4.54	1.43	1.00	1.31
S9B1 3	5	2.15	5.68	0.99	4.79	2.69	0.79	0.99	0.69
S9B1 3	6	2.08	4.95	0.96	4.15	2.71	0.72	0.99	0.62
S9B1 3	7	2.07	4.21	0.96	3.53	2.60	0.63	0.96	0.55
S9B1 4	1	2.08	4.24	0.98	3.56	2.64	0.66	0.96	0.58
S9B1 4	2	3.02	5.98	0.99	5.29	3.74	0.84	0.98	0.76
S9B1 4	3	3.40	8.38	0.99	7.52	4.03	1.10	0.99	1.01
S9B1 4	4	4.50	10.55	0.99	9.72	5.36	1.33	0.98	1.24
S9B1 4	5	2.13	5.47	0.97	4.60	2.72	0.76	0.98	0.67
S9B1 4	6	2.33	4.69	0.95	4.01	3.07	0.68	0.98	0.61
S9B1 4	7	2.22	4.39	0.96	3.72	2.76	0.66	0.97	0.58

Sample & Plate Segment		Normal Force β	η	R^2	Median	Shear Force β	η	R^2	Median
S9B1 5	1	2.18	4.15	0.97	3.51	2.66	0.66	0.99	0.58
S9B1 5	2	2.80	6.77	0.99	5.94	3.47	0.92	0.97	0.83
S9B1 5	3	2.72	9.33	0.99	8.15	3.31	1.20	1.00	1.07
S9B1 5	4	2.31	11.79	0.73	10.06	4.50	1.43	1.00	1.32
S9B1 5	5	1.93	5.64	0.94	4.66	2.33	0.80	0.95	0.68
S9B1 5	6	2.23	5.17	0.99	4.39	2.58	0.74	0.98	0.64
S9B1 5	7	2.19	4.74	0.99	4.01	2.83	0.69	0.99	0.61
S9B1 6	1	2.13	4.02	0.98	3.38	2.38	0.64	0.93	0.55
S9B1 6	2	2.55	6.33	0.98	5.48	3.29	0.86	0.98	0.77
S9B1 6	3	2.57	9.17	0.98	7.95	3.30	1.17	1.00	1.04
S9B1 6	4	3.35	11.69	0.96	10.48	4.23	1.42	0.97	1.30
S9B1 6	5	1.99	5.42	0.99	4.50	2.41	0.77	0.98	0.66
S9B1 6	6	2.07	4.51	0.97	3.78	2.62	0.67	0.98	0.58
S9B1 6	7	2.21	3.94	0.98	3.34	2.75	0.60	0.97	0.53
S9B1 7	1	2.03	4.09	0.98	3.41	2.52	0.63	0.97	0.54
S9B1 7	2	3.01	6.47	0.99	5.73	3.52	0.88	0.96	0.79
S9B1 7	3	3.42	9.50	0.98	8.54	3.86	1.20	0.97	1.09
S9B1 7	4	4.97	11.73	0.96	10.90	5.82	1.43	0.98	1.34
S9B1 7	5	2.18	6.26	0.97	5.29	2.73	0.84	0.97	0.74
S9B1 7	6	2.36	4.98	0.96	4.27	2.83	0.70	0.95	0.62
S9B1 7	7	2.48	4.13	0.99	3.56	3.05	0.62	0.99	0.55
S9B1 8	1	2.21	3.85	0.99	3.26	2.85	0.60	0.99	0.53
S9B1 8	2	2.84	6.28	0.97	5.52	3.48	0.85	0.98	0.77
S9B1 8	3	3.46	9.05	0.96	8.14	4.00	1.16	0.97	1.06
S9B1 8	4	5.37	11.38	0.98	10.63	6.38	1.39	0.99	1.31
S9B1 8	5	2.48	6.09	0.99	5.25	2.81	0.84	0.93	0.73
S9B1 8	6	2.33	4.44	0.94	3.80	3.00	0.64	0.99	0.57
S9B1 8	7	2.18	3.84	0.96	3.25	2.63	0.59	0.96	0.51
S9B1 9	1	2.10	3.99	0.98	3.35	2.55	0.61	0.98	0.52
S9B1 9	2	2.87	6.43	0.97	5.66	3.41	0.87	0.97	0.78
S9B1 9	3	3.17	9.36	0.92	8.34	3.65	1.18	0.92	1.07
S9B1 9	4	3.80	11.73	0.77	10.65	4.18	1.42	0.75	1.30
S9B1 9	5	2.30	6.26	0.93	5.34	2.88	0.85	0.94	0.75
S9B1 9	6	2.74	4.62	0.98	4.04	3.31	0.66	0.99	0.59
S9B1 9	7	2.14	4.06	0.95	3.42	2.50	0.61	0.95	0.53

C.2.3. Experiment S9B2

Table C-4, Normal and Shear Force Weibull Parameters (Exper. S9B2, Segments)

Sample & Plate Segment		Normal Force				Shear Force			
		β	η	R^2	Median	β	η	R^2	Median
S9B2 1	1	2.16	3.78	0.99	3.19	2.73	0.58	0.99	0.51
S9B2 1	2	2.70	5.37	0.96	4.69	3.22	0.75	0.92	0.67
S9B2 1	3	2.78	6.77	0.99	5.94	3.28	0.90	0.99	0.81
S9B2 1	4	3.39	8.06	0.98	7.23	4.10	1.03	0.99	0.94
S9B2 1	5	1.92	4.51	0.88	3.73	2.69	0.64	0.94	0.56
S9B2 1	6	2.53	4.43	0.99	3.83	2.82	0.64	0.96	0.56
S9B2 1	7	2.23	4.17	0.97	3.54	2.55	0.61	0.95	0.53
S9B2 2	1	2.30	4.81	0.99	4.10	3.10	0.69	1.00	0.61
S9B2 2	2	2.86	6.69	0.96	5.88	3.62	0.89	0.98	0.80
S9B2 2	3	4.06	7.95	0.99	7.26	4.50	1.03	0.98	0.95
S9B2 2	4	3.42	9.77	0.87	8.78	4.26	1.22	0.92	1.12
S9B2 2	5	2.90	5.77	0.99	5.09	3.42	0.80	0.99	0.72
S9B2 2	6	2.50	5.55	0.90	4.79	3.22	0.76	0.96	0.68
S9B2 2	7	2.85	5.66	0.99	4.98	3.41	0.78	0.99	0.70
S9B2 3	1	2.23	3.09	0.97	2.62	2.12	0.51	0.87	0.43
S9B2 3	2	2.19	3.79	0.87	3.21	2.93	0.55	0.91	0.49
S9B2 3	3	2.26	4.26	0.99	3.62	2.77	0.61	0.99	0.53
S9B2 3	4	2.35	5.33	0.98	4.56	2.99	0.73	0.99	0.65
S9B2 3	5	1.69	2.82	0.87	2.27	2.42	0.44	0.93	0.38
S9B2 3	6	2.42	3.39	0.97	2.91	2.40	0.53	0.93	0.45
S9B2 3	7	2.39	3.21	0.95	2.76	2.67	0.50	0.92	0.43
S9B2 4	1	2.07	3.35	0.96	2.81	2.62	0.53	0.96	0.46
S9B2 4	2	2.49	4.48	0.96	3.87	2.99	0.64	0.95	0.56
S9B2 4	3	2.34	5.65	0.92	4.83	2.96	0.76	0.95	0.68
S9B2 4	4	2.79	6.94	0.92	6.08	3.69	0.90	0.98	0.82
S9B2 4	5	2.22	3.76	0.95	3.19	2.70	0.55	0.96	0.48
S9B2 4	6	2.15	3.68	0.93	3.10	2.75	0.54	0.98	0.48
S9B2 4	7	2.12	3.82	0.97	3.21	2.47	0.56	0.95	0.49

Sample & Plate Segment		Normal Force β	Normal Force η	Normal Force R^2	Normal Force Median	Shear Force β	Shear Force η	Shear Force R^2	Shear Force Median
S9B2 5	1	2.08	3.49	0.97	2.93	2.67	0.54	0.97	0.47
S9B2 5	2	2.48	4.75	0.94	4.09	3.30	0.66	0.98	0.59
S9B2 5	3	2.82	5.98	0.96	5.25	3.26	0.81	0.95	0.72
S9B2 5	4	3.08	7.16	0.91	6.35	3.76	0.93	0.94	0.84
S9B2 5	5	2.19	4.02	0.93	3.40	2.75	0.59	0.94	0.51
S9B2 5	6	2.38	3.89	0.96	3.33	2.67	0.57	0.93	0.50
S9B2 5	7	2.25	3.94	0.95	3.35	2.81	0.57	0.97	0.50
S9B2 6	1	2.04	4.18	0.97	3.49	2.62	0.63	0.98	0.54
S9B2 6	2	2.70	5.52	0.96	4.82	3.42	0.76	0.98	0.68
S9B2 6	3	2.88	6.84	0.93	6.03	3.65	0.90	0.99	0.81
S9B2 6	4	3.55	7.84	0.99	7.07	4.01	1.00	0.97	0.92
S9B2 6	5	2.53	4.61	0.97	3.99	3.16	0.66	0.98	0.58
S9B2 6	6	2.60	4.71	0.99	4.09	2.88	0.67	0.94	0.59
S9B2 6	7	2.32	4.80	0.97	4.10	2.86	0.68	0.98	0.60
S9B2 7	1	2.04	4.91	0.96	4.10	2.61	0.72	0.95	0.63
S9B2 7	2	2.88	6.21	0.96	5.47	3.16	0.85	0.90	0.76
S9B2 7	3	3.50	7.41	0.99	6.67	4.13	0.98	0.99	0.89
S9B2 7	4	2.57	8.89	0.84	7.71	3.93	1.12	0.97	1.02
S9B2 7	5	2.25	5.61	0.95	4.77	3.01	0.77	0.98	0.68
S9B2 7	6	2.26	5.80	0.95	4.93	2.64	0.80	0.92	0.69
S9B2 7	7	2.22	6.13	0.90	5.20	2.74	0.84	0.87	0.73
S9B2 8	1	1.85	4.97	0.96	4.07	2.39	0.73	0.97	0.63
S9B2 8	2	2.77	6.31	0.98	5.53	3.54	0.86	0.99	0.78
S9B2 8	3	2.83	7.52	1.00	6.60	3.38	0.99	1.00	0.89
S9B2 8	4	2.94	9.13	0.95	8.06	3.69	1.16	0.96	1.05
S9B2 8	5	2.21	5.04	0.97	4.27	2.64	0.72	0.96	0.62
S9B2 8	6	2.39	5.53	0.99	4.74	2.85	0.77	0.99	0.68
S9B2 8	7	2.27	5.99	0.96	5.10	2.98	0.83	0.98	0.73
S9B2 9	1	1.84	4.96	0.96	4.07	2.37	0.73	0.97	0.62
S9B2 9	2	2.86	6.40	0.99	5.63	3.31	0.87	0.95	0.78
S9B2 9	3	2.77	7.79	0.99	6.82	3.36	1.02	0.99	0.91
S9B2 9	4	2.97	9.31	0.98	8.23	3.73	1.17	0.99	1.06
S9B2 9	5	2.16	5.21	0.95	4.40	2.88	0.73	0.99	0.64
S9B2 9	6	2.19	5.82	0.96	4.93	2.81	0.80	0.98	0.70
S9B2 9	7	2.43	6.11	0.99	5.25	2.92	0.84	0.97	0.74

C.2.4. Experiment S12

Table C-5, Normal and Shear Force Weibull Parameters (Experiment S12, Segments)

Sample & Plate Segment		Normal Force				Shear Force			
		β	η	R^2	Median	β	η	R^2	Median
S12 1	1	2.25	3.46	0.95	2.94	2.51	0.56	0.91	0.49
S12 1	2	2.51	3.08	0.95	2.66	2.45	0.53	0.87	0.46
S12 1	3	2.34	2.90	0.95	2.48	2.60	0.49	0.96	0.43
S12 1	4	2.47	4.28	0.92	3.69	2.78	0.67	0.91	0.59
S12 1	5	2.43	5.68	0.90	4.89	2.97	0.83	0.92	0.74
S12 1	6	3.54	7.71	0.94	6.95	3.64	1.07	0.86	0.96
S12 1	7	2.10	4.32	0.91	3.63	2.41	0.66	0.89	0.57
S12 2	1	2.17	3.43	0.93	2.90	2.49	0.57	0.93	0.49
S12 2	2	2.53	5.01	0.94	4.34	2.96	0.76	0.92	0.67
S12 2	3	2.30	6.29	0.91	5.37	2.69	0.91	0.88	0.80
S12 2	4	2.89	7.66	0.92	6.75	3.27	1.06	0.90	0.94
S12 2	5	2.23	4.53	0.93	3.85	2.68	0.70	0.93	0.61
S12 2	6	2.29	3.88	0.93	3.31	2.62	0.63	0.92	0.55
S12 2	7	2.39	3.56	0.94	3.05	2.63	0.60	0.89	0.52
S12 3	1	2.17	3.31	0.92	2.79	2.60	0.55	0.96	0.47
S12 3	2	2.70	4.79	0.92	4.19	3.02	0.74	0.92	0.66
S12 3	3	2.81	5.98	0.94	5.25	3.26	0.88	0.92	0.78
S12 3	4	3.74	7.93	0.94	7.18	4.06	1.09	0.90	1.00
S12 3	5	2.01	4.74	0.85	3.95	2.62	0.71	0.87	0.62
S12 3	6	2.34	3.84	0.91	3.29	2.96	0.62	0.94	0.54
S12 3	7	2.35	3.48	0.92	2.98	2.82	0.59	0.94	0.52
S12 4	1	2.60	2.97	0.97	2.58	2.41	0.52	0.91	0.44
S12 4	2	2.59	4.23	0.98	3.67	2.73	0.69	0.91	0.60
S12 4	3	2.62	5.49	0.97	4.78	3.22	0.82	0.99	0.73
S12 4	4	2.84	6.98	0.94	6.14	3.46	0.98	0.96	0.88
S12 4	5	2.03	3.98	0.94	3.32	2.23	0.63	0.88	0.53
S12 4	6	2.24	3.33	0.94	2.83	2.44	0.56	0.87	0.48
S12 4	7	2.06	3.14	0.88	2.63	2.54	0.53	0.90	0.46

Sample & Plate Segment		Normal Force				Shear Force			
		β	η	R^2	Median	β	η	R^2	Median
S12 5	1	2.16	3.90	0.95	3.29	2.59	0.64	0.95	0.56
S12 5	2	1.91	4.01	0.92	3.31	2.49	0.65	0.98	0.56
S12 5	3	2.21	5.59	0.95	4.73	2.76	0.84	0.96	0.74
S12 5	4	2.21	6.93	0.92	5.87	3.00	0.98	0.95	0.87
S12 5	5	2.82	7.48	0.97	6.57	3.44	1.04	0.96	0.93
S12 5	6	2.23	4.37	0.92	3.71	2.84	0.68	0.95	0.60
S12 5	7	2.21	4.03	0.95	3.42	2.47	0.65	0.91	0.56
S12 6	1	2.22	4.29	0.92	3.64	2.59	0.69	0.89	0.60
S12 6	2	2.15	4.22	0.95	3.56	2.17	0.68	0.85	0.57
S12 6	3	2.38	6.18	0.88	5.30	3.42	0.90	0.98	0.81
S12 6	4	3.00	7.31	0.99	6.47	3.17	1.03	0.90	0.92
S12 6	5	2.87	8.62	0.87	7.58	4.15	1.16	0.98	1.06
S12 6	6	2.02	5.13	0.88	4.28	2.85	0.76	0.95	0.67
S12 6	7	2.38	4.59	0.94	3.93	3.06	0.72	0.98	0.64
S12 7	1	2.11	4.53	0.96	3.81	2.48	0.72	0.97	0.62
S12 7	2	2.11	6.35	0.97	5.34	2.54	0.92	0.93	0.80
S12 7	3	2.55	8.01	0.98	6.94	3.01	1.10	0.94	0.98
S12 7	4	2.97	8.61	0.98	7.61	3.69	1.14	0.99	1.04
S12 7	5	2.14	4.91	0.96	4.14	2.54	0.74	0.92	0.64
S12 7	6	2.23	4.65	0.95	3.94	2.71	0.70	0.93	0.62
S12 7	7	2.10	4.58	0.94	3.84	2.29	0.72	0.88	0.61
S12 8	1	2.28	3.64	0.95	3.10	2.62	0.60	0.95	0.52
S12 8	2	2.47	5.21	0.95	4.49	2.87	0.79	0.94	0.70
S12 8	3	2.55	6.40	0.95	5.54	3.01	0.92	0.94	0.82
S12 8	4	2.79	7.22	0.94	6.33	3.31	1.00	0.94	0.89
S12 8	5	2.20	4.27	0.94	3.61	2.58	0.66	0.92	0.58
S12 8	6	2.13	3.86	0.91	3.25	2.41	0.63	0.88	0.54
S12 8	7	2.14	3.73	0.92	3.14	2.51	0.62	0.92	0.53
S12 9	1	1.97	4.91	0.97	4.08	2.38	0.76	0.96	0.65
S12 9	2	2.35	6.73	0.97	5.76	2.98	0.97	0.99	0.85
S12 9	3	2.55	8.53	0.94	7.39	3.35	1.16	0.96	1.04
S12 9	4	2.63	9.19	0.97	7.99	3.11	1.22	0.93	1.08
S12 9	5	2.54	5.18	0.98	4.49	2.93	0.78	0.95	0.69
S12 9	6	2.21	4.96	0.94	4.21	2.83	0.75	0.96	0.66
S12 9	7	2.07	4.89	0.92	4.10	2.88	0.76	0.97	0.67

C.3. Bar Level

C.3.1. Bar #4

Table C-6, Normal and Shear Force Weibull Parameters (Bar #4)

	Normal Force				Shear Force			
Experiment	β	η	R^2	Median	β	η	R^2	Median
S9 1	2.72	4.50	0.98	3.94	3.29	0.64	0.98	0.57
S9 2	2.09	6.00	0.93	5.04	2.17	0.83	0.87	0.70
S9 3	3.19	5.08	0.97	4.53	3.54	0.73	0.97	0.65
S9 4	3.40	5.96	0.96	5.35	4.15	0.81	0.96	0.75
S9 5	3.02	4.04	0.96	3.58	3.42	0.60	0.97	0.54
S9 6	3.24	4.73	0.95	4.22	4.16	0.67	0.95	0.61
S9 7	3.02	5.27	0.99	4.67	3.78	0.72	0.98	0.66
S9 8	3.29	3.73	0.91	3.34	4.05	0.55	0.96	0.50
S9 9	2.62	5.29	0.98	4.60	3.46	0.78	0.98	0.70
S9B1 1	3.83	8.78	0.99	7.97	5.13	1.11	0.98	1.03
S9B1 2	4.54	9.30	0.97	8.58	5.73	1.16	0.98	1.09
S9B1 3	3.48	8.88	0.98	7.99	4.39	1.11	0.98	1.02
S9B1 4	5.42	9.40	0.94	8.79	6.89	1.21	0.96	1.15
S9B1 5	0.68	9.74	0.59	5.69	2.73	1.18	0.99	1.03
S9B1 6	3.72	8.71	0.99	7.89	4.35	1.09	0.99	1.01
S9B1 7	4.96	10.11	1.00	9.39	5.66	1.26	0.99	1.18
S9B1 8	5.50	10.04	0.95	9.39	6.10	1.25	0.96	1.18
S9B1 9	6.01	10.14	0.97	9.54	6.49	1.26	0.98	1.19
S9B2 1	3.90	5.96	0.97	5.43	4.68	0.78	0.97	0.73
S9B2 2	4.88	8.06	0.98	7.47	5.53	1.03	0.95	0.96
S9B2 3	1.76	3.26	0.80	2.65	2.30	0.53	0.82	0.45
S9B2 4	2.81	4.81	0.96	4.22	3.12	0.67	0.89	0.59
S9B2 5	4.10	5.77	0.99	5.27	4.67	0.76	0.98	0.71
S9B2 6	3.76	6.15	0.99	5.57	4.54	0.81	0.99	0.74
S9B2 7	3.01	7.20	0.99	6.38	3.22	0.93	0.95	0.83
S9B2 8	2.93	6.62	0.99	5.85	3.71	0.90	0.98	0.82
S9B2 9	3.30	6.91	0.97	6.18	4.15	0.92	0.96	0.84
S12 1	3.83	3.93	0.97	3.57	3.78	0.63	0.91	0.57
S12 2	5.26	7.29	0.98	6.80	6.21	1.09	0.99	1.02
S12 3	5.29	7.49	0.97	6.99	5.86	1.10	0.98	1.04
S12 4	3.32	6.70	0.99	6.00	3.47	1.02	0.93	0.92
S12 5	3.56	6.10	0.96	5.50	4.37	0.88	0.95	0.81
S12 6	4.83	7.17	0.98	6.65	5.91	1.00	0.98	0.94
S12 7	2.15	6.67	0.88	5.63	2.85	1.02	0.90	0.90
S12 8	3.90	6.64	0.98	6.04	4.58	1.00	0.97	0.93
S12 9	2.79	6.61	0.99	5.80	3.63	1.05	0.99	0.95

C.3.2. Bar #8

Table C-7, Normal and Shear Force Weibull Parameters (Bar #8)

	Normal Force				Shear Force			
Experiment	β	η	R^2	Median	β	η	R^2	Median
S9 1	2.54	5.54	0.87	4.79	3.40	0.75	0.89	0.67
S9 2	3.82	7.17	0.98	6.52	4.99	0.94	0.97	0.87
S9 3	4.05	6.41	0.97	5.86	4.55	0.86	0.98	0.79
S9 4	4.18	7.26	0.96	6.65	5.19	0.94	0.97	0.88
S9 5	3.58	5.97	0.94	5.39	4.05	0.80	0.91	0.73
S9 6	3.78	6.09	0.93	5.52	4.36	0.81	0.93	0.74
S9 7	3.95	6.78	0.99	6.18	4.98	0.89	0.99	0.82
S9 8	3.51	4.76	0.99	4.29	4.54	0.68	0.99	0.63
S9 9	3.34	7.20	0.97	6.45	3.89	0.98	0.97	0.89
S9B1 1	7.28	11.22	0.98	10.67	7.82	1.37	0.97	1.31
S9B1 2	4.60	11.11	0.96	10.26	5.55	1.34	0.97	1.26
S9B1 3	5.33	13.28	0.97	12.40	6.55	1.53	0.96	1.45
S9B1 4	3.43	10.84	0.81	9.74	3.99	1.34	0.77	1.22
S9B1 5	5.21	11.91	0.97	11.10	6.63	1.41	0.98	1.33
S9B1 6	5.09	12.69	0.99	11.81	6.01	1.49	0.98	1.40
S9B1 7	6.98	11.33	0.97	10.75	7.54	1.40	0.97	1.33
S9B1 8	7.78	10.87	0.98	10.37	8.78	1.32	0.97	1.26
S9B1 9	7.41	10.72	0.95	10.20	8.24	1.29	0.93	1.24
S9B2 1	3.77	7.73	0.94	7.01	4.91	1.01	0.97	0.93
S9B2 2	1.51	9.53	0.51	7.47	3.25	1.18	0.68	1.06
S9B2 3	2.56	5.08	0.94	4.40	3.29	0.68	0.94	0.61
S9B2 4	3.03	6.99	0.90	6.20	4.00	0.91	0.96	0.83
S9B2 5	5.39	6.66	0.95	6.23	6.04	0.87	0.96	0.82
S9B2 6	4.87	7.78	0.98	7.21	5.62	0.97	0.98	0.91
S9B2 7	2.18	9.40	0.65	7.95	3.27	1.17	0.75	1.04
S9B2 8	5.53	9.32	0.99	8.73	6.69	1.16	0.99	1.10
S9B2 9	4.97	10.08	0.98	9.36	6.11	1.22	0.98	1.15
S12 1	2.67	4.86	0.89	4.23	3.62	0.72	0.98	0.65
S12 2	4.66	9.59	0.86	8.86	5.37	1.33	0.91	1.24
S12 3	5.16	9.62	0.87	8.96	7.19	1.33	0.96	1.26
S12 4	2.63	8.65	0.84	7.53	3.13	1.24	0.86	1.10
S12 5	1.58	8.24	0.59	6.53	4.19	1.12	0.94	1.02
S12 6	4.18	8.39	0.94	7.68	5.19	1.18	0.97	1.10
S12 7	4.37	9.57	0.99	8.80	5.48	1.34	0.98	1.25
S12 8	3.24	9.11	0.76	8.14	4.21	1.27	0.87	1.17
S12 9	4.56	10.89	0.99	10.05	5.91	1.44	0.99	1.36

C.3.3. Bar #12

Table C-8, Normal and Shear Force Weibull Parameters (Bar #12)

	Normal Force				Shear Force			
Experiment	β	η	R^2	Median	β	η	R^2	Median
S9 1	4.35	6.35	0.99	5.84	4.81	0.90	0.99	0.83
S9 2	1.58	7.72	0.59	6.12	4.73	1.01	0.98	0.93
S9 3	4.43	7.00	0.99	6.44	4.75	0.94	0.98	0.87
S9 4	3.37	8.06	0.97	7.23	4.22	1.07	0.96	0.98
S9 5	3.98	7.11	0.99	6.48	4.92	0.94	0.98	0.88
S9 6	3.85	6.71	0.98	6.10	5.10	0.93	0.97	0.86
S9 7	1.94	8.08	0.77	6.70	2.70	1.05	0.83	0.92
S9 8	3.44	6.02	0.96	5.41	4.24	0.83	0.96	0.76
S9 9	5.23	9.21	0.96	8.59	6.30	1.19	0.96	1.12
S9B1 1	4.48	10.73	0.98	9.89	5.56	1.34	0.97	1.25
S9B1 2	3.65	11.34	0.98	10.26	4.49	1.39	0.96	1.29
S9B1 3	4.89	13.91	0.99	12.91	6.13	1.63	0.98	1.53
S9B1 4	3.69	11.23	0.88	10.17	4.66	1.36	0.88	1.26
S9B1 5	4.48	13.12	0.93	12.09	5.52	1.57	0.92	1.47
S9B1 6	4.21	13.50	0.99	12.38	5.43	1.57	0.99	1.47
S9B1 7	5.17	11.75	0.98	10.95	6.27	1.40	0.98	1.32
S9B1 8	6.24	12.08	0.96	11.39	7.70	1.42	0.93	1.35
S9B1 9	5.62	12.44	0.97	11.65	6.93	1.41	0.99	1.34
S9B2 1	2.79	8.48	0.84	7.44	3.80	1.06	0.89	0.96
S9B2 2	5.10	10.27	0.98	9.56	5.98	1.25	0.97	1.17
S9B2 3	2.12	6.10	0.84	5.13	2.87	0.80	0.85	0.70
S9B2 4	2.72	6.68	0.92	5.84	3.22	0.87	0.90	0.77
S9B2 5	3.47	7.21	0.96	6.49	4.30	0.93	0.98	0.86
S9B2 6	4.00	7.37	0.98	6.73	5.05	0.96	0.99	0.89
S9B2 7	4.44	10.02	0.99	9.23	5.78	1.19	0.97	1.12
S9B2 8	4.73	10.41	0.99	9.64	5.80	1.25	0.98	1.18
S9B2 9	4.78	10.72	0.99	9.93	5.87	1.27	0.99	1.20
S12 1	2.76	4.00	0.90	3.50	2.62	0.65	0.85	0.56
S12 2	2.83	6.26	0.99	5.50	3.30	0.93	0.98	0.83
S12 3	2.68	7.45	0.93	6.50	2.13	1.06	0.73	0.89
S12 4	2.44	5.69	0.97	4.89	2.63	0.85	0.91	0.74
S12 5	4.28	7.77	0.97	7.13	4.56	1.05	0.98	0.97
S12 6	4.48	8.03	0.99	7.40	5.20	1.06	0.99	0.99
S12 7	3.58	8.23	0.99	7.43	4.52	1.10	0.97	1.01
S12 8	2.38	6.53	0.95	5.60	3.20	0.91	0.98	0.81
S12 9	2.07	9.02	0.85	7.56	3.43	1.15	0.97	1.03